



university of  
 groningen

faculty of science  
 and engineering

NATIONAL INSTITUTE FOR SUBATOMIC PHYSICS  
 DETECTOR R&D DEPARTMENT

*Fast Silicon Pixel Sensors Group*

MECHANICAL ENGINEERING: ADVANCED INSTRUMENTATION  
 MASTER RESEARCH PROJECT [WMME902-40]

---

# Time Resolution of an HV-CMOS Based Silicon Detector using Picosecond Pulsed Infrared Lasers

---

*Author:*

Thijs Niemeijer (s3188825)

*Supervisors:*

Dr. U. Kraemer

Dr. G. de Lange

Dr. Ir. P. Dieleman

Nikhef

April 26, 2024

## Abstract

This thesis delves into the advancements and performance evaluation of High-Voltage CMOS (HV-CMOS) based silicon tracking detectors (RD50-MPW3/RD50-MPW4), focusing on their application in high-energy physics environments characterized by high radiation and particle flux. Integrating monolithic active pixel sensor technology into particle detection systems offers a compact, cost-efficient alternative to traditional hybrid pixel detectors, reducing complexity and enhancing performance in harsh operational conditions.

In this Master's thesis, the emphasis is placed on the time resolution of silicon-based detectors. This superior time resolution is necessary for accurately tracking particle trajectories and improving event reconstruction accuracy utilizing the fourth dimension, Time. Through the use of picosecond pulsed infrared lasers, this study provides a characterization of the time response of these detectors, showcasing the direct impacts of advancements made in the RD50-MPW detectors.

Experimental results indicate that while sensor architecture and readout electronics enhancements have led to improved temporal and spatial resolution, challenges remain in mitigating noise and optimizing the interface between digital and analogue components. This research project identified enhancements in time resolution and signal integrity in the RD50-MPW4 compared to its predecessor. Where the measured time resolution went from  $\sigma_t = 2.01$  ns to  $\sigma_t = 347$  ps with clock enabled. For clock disabled, the measured time resolution went from  $\sigma_t = 293$  ps to  $\sigma_t = 66$  ps. This improvement is mainly attributable to improvements in pixel architecture and digital readout systems, which have contributed to better control over noise and external clock influences. Despite these advancements, challenges remain, particularly in achieving time resolution below the tens of picoseconds due to system and component limitations such as the Preamplifier bandwidth constraints.

Furthermore, the results have highlighted the importance of temperature control on detector performance. This sensitivity to minor temperature fluctuation illuminates the necessity for environmental control measures, especially in future high-luminosity environments, where the integration of time as the fourth parameter depends on the precision of the time resolution.

In conclusion, the insights gained from the RD50-MPW series provide valuable directions for future research and development. It points towards the need for integrated solutions that address the technological and environmental factors affecting detector performances. The research presented in this thesis contributes to this ongoing effort and sets the framework for the next generation of particle detection technology.

*Keywords: HV-CMOS, silicon-based tracking detectors, time resolution, high-energy physics, infrared lasers, particle tracking.*

***“Not all those who wander are lost.”***

— J.R.R. Tolkien, *The Lord of the Rings*

# Contents

<b>1</b>	<b>Introduction</b>	<b>1</b>
1.1	Overview of High Energy Physics Experiments and Detectors . . . . .	1
1.2	Progression and Challenges in High Energy Particle Physics . . . . .	2
1.3	Goal and Structure of this Thesis . . . . .	6
<b>2</b>	<b>Semiconductor Based Particle Detectors</b>	<b>7</b>
2.1	Semiconductors . . . . .	7
2.1.1	Historic Overview . . . . .	8
2.1.2	Semiconductor Basics . . . . .	9
2.1.3	Band Diagrams with Direct and Indirect Bandgap . . . . .	10
2.1.4	Intrinsic and Extrinsic Semiconductors . . . . .	12
2.1.5	PN-Junction . . . . .	14
2.1.6	Reverse Bias in PN-Junctions of Silicon Detectors . . . . .	14
2.2	Silicon as the Detector Material . . . . .	16
2.2.1	Particles Interacting with Matter . . . . .	17
2.2.2	Energy Loss Fluctuation . . . . .	20
2.2.3	Drift Velocity in Detectors . . . . .	21
2.3	Pixel Detectors . . . . .	22
2.3.1	Hybrid Pixel Detector . . . . .	23
2.3.2	CMOS Monolithic Pixel Detectors . . . . .	24
2.3.3	Depleted Monolithic Active Pixel Sensors (DMAPS) . . . . .	26
2.4	Timing in Silicon-Based Pixel Detectors . . . . .	30
2.4.1	Clocking Mechanisms and Time Resolution . . . . .	30
2.4.2	Influence of Binning Size on Time Resolution . . . . .	30
2.4.3	Timewalk in Front-End Electronics . . . . .	31
2.4.4	Jitter in Front-End Electronics . . . . .	33
<b>3</b>	<b>Readout Systems for Pixel Detectors</b>	<b>34</b>
3.1	Setup and Instrumentation . . . . .	34
3.1.1	Laser Characterization and Selection . . . . .	34
3.1.2	Pulse Generation and Modulation . . . . .	36
3.1.3	Signal Visualization and Data Acquisition via Oscilloscope . . . . .	36
3.1.4	Power Supply and Bias Voltage Application . . . . .	38
3.1.5	Characterization of the Diodes and Detector . . . . .	38
3.2	DAQ . . . . .	40
3.2.1	Caribou . . . . .	40
3.2.2	Graphical User Interface . . . . .	41
3.2.3	The Readout Electronics . . . . .	41
3.3	Evolution of the RD50-MPW Series . . . . .	43
3.3.1	Introduction of the RD50-MPW3 . . . . .	44
3.3.2	RD50-MPW3; Digital Infrastructure and In-pixel Signal Processing . . . . .	45
3.4	Description of the RD50-MPW4 . . . . .	47
3.4.1	Design Methodology and Innovations: . . . . .	47
3.4.2	Key Enhancements: . . . . .	48

<b>4</b>	<b>Results</b>	<b>50</b>
4.1	Laser and Diode . . . . .	50
4.1.1	683 nm, QFLD-670-2S . . . . .	50
4.1.2	976 nm, QFBGLD-980-5 . . . . .	50
4.1.3	933 nm, PIL1-094-40FC . . . . .	53
4.2	RD50-MPW3 . . . . .	54
4.2.1	Charge Injection and $ToT$ Calibration . . . . .	54
4.2.2	External Clock Effects . . . . .	55
4.2.3	Pixel Response Through S-Curve Characterization . . . . .	58
4.3	RD50-MPW4 . . . . .	60
4.3.1	IV Curve of the RD50-MPW4 Pixel Matrix . . . . .	60
4.3.2	Charge Injection and $ToT$ Calibration . . . . .	61
4.3.3	External Clock Effects . . . . .	62
4.3.4	Reverse Bias Voltage Effects on the RD50-MPW4 . . . . .	63
<b>5</b>	<b>Discussion</b>	<b>65</b>
5.1	Implications of External Clock Effects . . . . .	65
5.2	Implications of PreAmplifier . . . . .	65
5.3	Time Resolution Improvements and Anticipated <i>MIP</i> Performance . . . . .	65
5.4	Constraints on Time . . . . .	65
<b>6</b>	<b>Outlook</b>	<b>66</b>
<b>7</b>	<b>Conclusion</b>	<b>66</b>
	<b>Acknowledgements</b>	<b>66</b>
	<b>References</b>	<b>72</b>
	<b>Appendices</b>	<b>73</b>
<b>A</b>	<b>Supplementary Information</b>	<b>73</b>
A.1	Detailed Analysis of Particle Interaction and Energy Loss Mechanisms . . . . .	73
A.2	Energy Loss Fluctuation . . . . .	73
<b>B</b>	<b>Laser Specifics</b>	<b>77</b>
<b>C</b>	<b>Test and Calibration Report of the PILAS System</b>	<b>79</b>
<b>D</b>	<b>Measurement Graphs</b>	<b>83</b>
D.1	683 nm . . . . .	83
D.2	976 nm . . . . .	84
D.3	933 nm . . . . .	86
D.4	RD50-MPW3 . . . . .	87
D.5	RD50-MPW4 . . . . .	90

# 1 Introduction

This thesis seeks to outline the progression of the current detector physics done at Nikhef, specifically focusing on the evolving field of silicon-based tracking detectors. The following introduction is divided into three subsections:

First, an overview is given in [subsection 1.1](#), showing the general events that took place within the High Energy Physics research community, which demand a new approach towards future particle detectors. Subsequently, the relevant subtopic of Progression in the Field of Research is presented in [subsection 1.2](#). This subsection will give an overview of what prior work was conducted by the Nikhef Institute R&D Department and the CERN RD50 Collaboration and how the current objective fits in this overall research area. The CERN RD50 Collaboration aims to pioneer sensor technologies that remain operational within high-radiation fields. The focus is on innovative structures (HV-CMOS) which promise enhanced radiation tolerance and operational longevity in harsh environments. From this, the goal of this Master Research Project was concluded, and the further structure of the report is presented in [subsection 1.3](#).

## 1.1 Overview of High Energy Physics Experiments and Detectors

High-energy particle physics is on the frontier of unravelling the building blocks of the universe; this is done through experiments such as the operations at the Large Hadron Collider (LHC) [1]. A depiction of the LHC layout is depicted in [Figure 1.1](#). Key to these explorations are tracking detectors that reconstruct the trajectories of charged particles produced during collisions, enabling the determination of their momentum and point of origin (vertex). Modern-day operations depend on finely segmented silicon detectors in order to determine the position of charged particles down to a few micrometres. As progress advances, it unavoidably encounters increasingly complex challenges, as is the tradition in the iterative innovation process. With the upgrades scheduled in 2029 for the High-Luminosity LHC (HL-LHC) project, there is an expected surge in the average collision rate within a 25 ns time window, rising from around 20 events to nearly 200 [2]. This increase amplifies the computational complexity and presents challenges to the performance of current tracking detectors. In order to reduce this complexity and overcome these hurdles, different approaches, such as the introduction of time as a fourth tracking parameter, are being investigated.

Integrating time as the fourth tracking parameter offers a simplification in the interpretation of collision events. By temporally distinguishing them, an improvement in the physics performance becomes feasible [1], as can be seen in [Figures 1.2-1.3](#). Furthermore, an improved time resolution allows for the identification of the type of particle through ToF measurements [4]. To harness these advantages, it is essential for silicon detectors to achieve time resolutions in the order of tens of picoseconds [1, 2]. This is a challenging goal as, currently, the time resolutions are in the order of hundreds of picoseconds (around 300 ps for MPW2 and 500 ps for MPW3) [5, 6].

It demands an in-depth understanding of foundational processes like charge generation and its subsequent transport in silicon. One prominent way to delve into these processes is through charge injection utilising infrared lasers, which are capable of achieving the desired time resolution. These utilised infrared lasers are rapid (40 MHz) and concise pulses (jitter of 1.9 ps), as can be seen in [Appendix C](#). The Detector R&D department at Nikhef stands at the forefront of this endeavour. The group works on all aspects of silicon-based detectors, optimising reaching from sensor geometry and technology to application-specific integrated circuits (ASIC) for signal amplification and digitisation.

Transitioning from the Large Hadron Collider’s overview to detailed advancements in detector technologies, the next section, [subsection 1.2](#), focuses on the progression within silicon-based

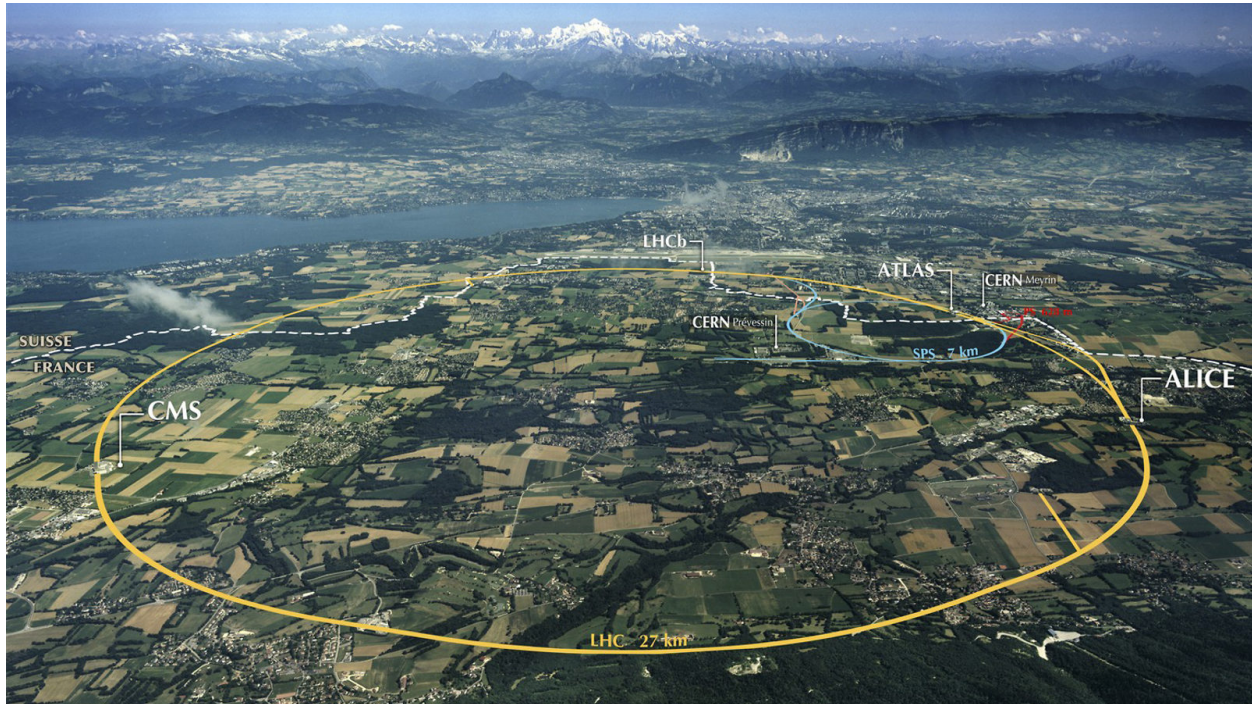


Figure 1.1: The aerial view captures CERN’s accelerator complex, showcasing the Large Hadron Collider (LHC) in yellow, the Super Proton Synchrotron (SPS) in blue, and the Proton Synchrotron (PS) in red, all located within underground tunnels. Positioned near the ATLAS detector, the main CERN site is set against the backdrop of Lake Geneva and Mont Blanc, showing the scientific infrastructure and the natural environment of the Geneva region. Image is taken from [3].

tracking detectors. It highlights past achievements, ongoing research, and future objectives crucial for tackling the challenges of high-luminosity colliders and the pursuit of new physics beyond the Standard Model.

## 1.2 Progression and Challenges in High Energy Particle Physics

The Standard Model (SM) of elementary particles stands as the central concept in the field of particle physics, offering insights into the fundamental structure and forces of the universe [7]. Despite its significant impact in explaining a wide array of experimental results, the SM is increasingly recognized by the scientific community as an incomplete framework, and many aspects of it are under investigation. Several phenomena and theoretical considerations highlight the limitations and point towards a complex underlying layer of physics yet to be uncovered [8, 7].

1. The SM lacks a natural mechanism for explaining the determined values of its numerous free parameters, such as particle masses. Particularly, the Higgs boson’s observed mass of  $125 \text{ GeV}/c^2$  presents a theoretical challenge, requiring an unusual fine-tuning of the “bare” Higgs mass and quantum corrections ( $10^{16} \text{ GeV}/c^2$  to  $10^{19} \text{ GeV}/c^2$ ) to avoid unnatural large values predicted by the SM [9, 10].
2. The SM does not provide an explanation for the observed matter-antimatter asymmetry in the universe [11].

3. The SM does not incorporate a mechanism for CP violation in strong interactions, an anomaly given its occurrence in weak interactions between quarks [12].
4. Furthermore, within the framework of the SM, only 15% of the universe’s matter is accounted for, leaving the composition of the remaining 85% as an unresolved topic attributed to dark matter [13]. This form of matter does not interact with electromagnetic radiation in a way that allows it to be directly observed with existing optical telescopes, and it cannot be described by any of the known particles within the SM’s particle collection.
5. Additionally, the concept of dark energy is presented as a theory to explain the universe’s accelerating expansion, a phenomenon supported by observational cosmology. The rate of this expansion implies the existence of an energy density vastly inferior to the predicted vacuum energy density within SM calculations, presenting a significant discrepancy known as the “cosmological constant problem” [14].

These concepts, critical to our understanding of the universe, are entirely absent from the SM’s particle collection and therefore require further investigations.

The phenomenon of neutrino oscillation further complicates the SM’s perspective by implying that neutrinos, long thought to be massless, possess a small mass [15]. This observation challenges the SM’s current structure, as does the inability to include gravity with quantum mechanics within the model’s framework [16]. Further, distancing the SM from upscaling to larger dimensions and extensive implementation.

The LHC, situated within the CERN accelerator complex, as depicted in [Figure 1.1](#), consists of a circular particle accelerator spanning a circumference of 27 kilometres. In the field of high-energy physics, the LHC plays a crucial role in challenging the established norms of the Standard Model. It propels packets of protons, and in certain instances ions, in opposing directions, inducing collisions at designated interaction points. These collision events are analysed using particle detectors, enabling the exploration of the resultant particle debris.

The use of collider-based physics stands as a promising method to uncover rare particles that remain undiscovered within the Standard Model’s framework. The intrinsic rarity of these particles’ production during collision events requires an increase in the total number of collisions to be conducted. This increase in collision frequency is necessary to increase the probability of detecting new particle candidates, thereby extending the boundaries of our current understanding of particle physics.

In the context of particle physics, luminosity is a fundamental parameter that quantifies the intensity of a particle collider. It is defined as the number of particles per unit area per unit of time that collide within a specific interaction region. The higher the luminosity, the greater the number of collisions per second, increasing the likelihood of observing rare processes [1]. In practical terms, luminosity is a measure of a collider’s performance, with high-luminosity environments enabling experiments to accumulate sufficient data for statistical analysis of particle interactions, thus facilitating discoveries at the frontier of fundamental physics.

The rapidly increasing amount of instantaneous collision events at high-luminosity colliders calls for improved tracking techniques capable of distinguishing primary vertices in densely packed interaction regions within the detectors. These improvements in the high-luminosity colliders might be able to shed light on some of the challenges named for the SM and, therefore, are highly anticipated.

At the first long shutdown (2013/2014), the LHC increased a collision energy design from 8 TeV to 14 TeV [17]. The integration of time measurements into trajectory reconstruction (4D tracking)



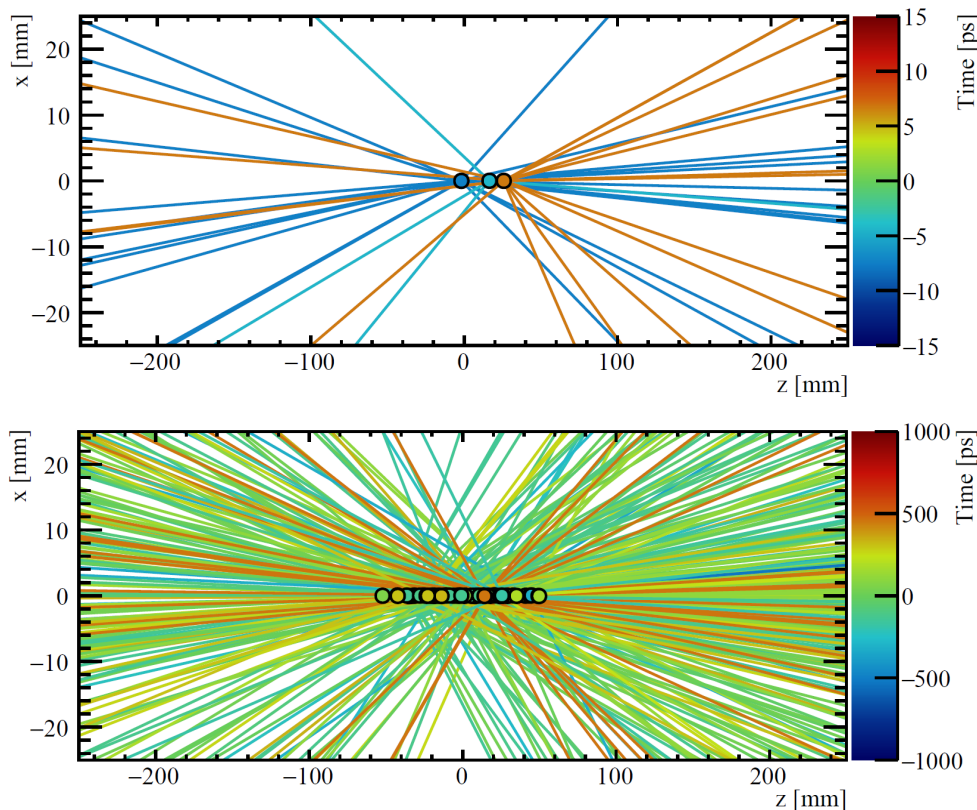


Figure 1.2: The figure illustrates the importance of temporal resolution in mitigating pile-up effects within the VELO. Depicted are primary vertices (dots) and their resulting particle trajectories (lines), colour-coded by their timestamps. A representative proton-proton collision scenario with an average of 42 interactions demonstrates how temporal segregation, achieved by narrowing the observation window in time, diminishes observed pile-up. This effect is indicated by the decreased density of coloured vertices and tracks in the figure. The sequence shows a selection of a collision event (of roughly 2 ns) in the bottom image, while the top image focuses on a refined temporal window of 30 ps, highlighting the improved event resolution through temporal selection. Image is taken from [20].

enhances the characterisation of matching collision events, highlighting the importance of improved time resolution in next-generation silicon pixel detectors [18, 19].

The "A Toroidal LHC ApparatuS" (ATLAS) and "Compact Muon Solenoid" (CMS) experiments are on track to deploy timing layers for Run 4, marking a significant advancement towards combining excellent timing with precise determination of trajectories [2, 18]. The upgrade planned for the LHCb and ALICE detectors, which are due in 2035, still have the experiments' strategy under consideration. However, here is a tracking system that combines excellent timing with precise determination of trajectories most appropriate for maintaining vertex locator performance [18, 21, 22]. In Figure 1.2, the addition of excellent timing with precise determination of trajectories is further emphasised for its significance in tracking. Future colliders like the FCC-hh, with its goal of reaching 100 TeV collision energy [23], will face major challenges in measured event pile-up (up to values of the order  $10^3$ ) [24]. The further pile-up of events will make the separation of trajectories and collisions even more difficult if only using 3D tracking.

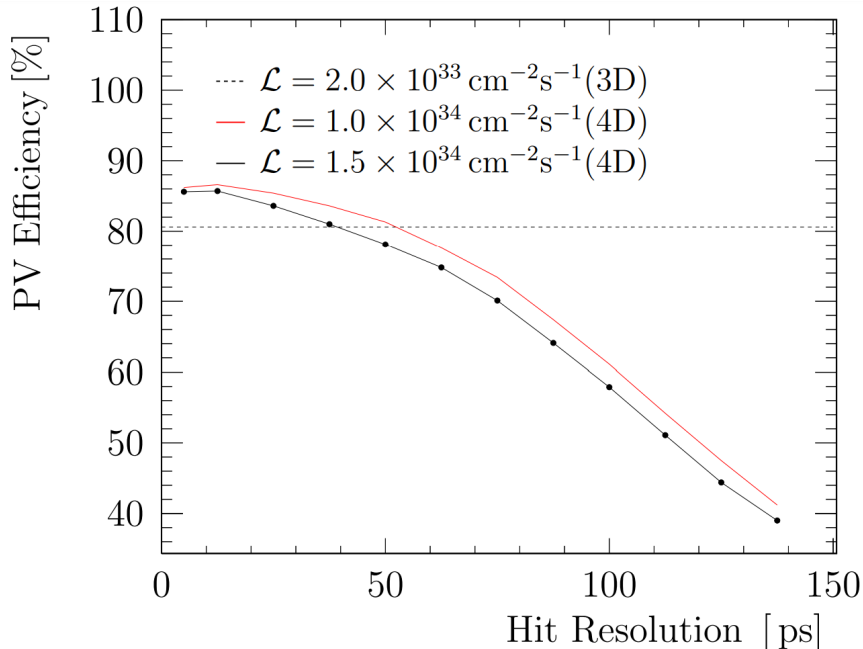


Figure 1.3: This plot illustrates the primary vertex (PV) reconstruction efficiency as a function of single hit resolution. The dotted line depicts the performance during Upgrade I, which does not utilize timing measurements for reconstruction. This shows that in order to achieve a similar efficiency in reconstructing the PV, a time resolution on the order of  $\sim 40$  ps is required. Image is taken from [1].

Furthermore, [Figure 1.3](#) provides a comparison of primary vertex (PV) reconstruction efficiency between two operational scenarios of the Vertex Locator (VELO) detector within the LHCb experiment. It contrasts the efficiency of the VELO following its initial upgrade (referred to as VELO Upgrade I) when subjected to the conditions anticipated for a further upgrade (Upgrade II) against its operational efficiency under the initial upgrade conditions (Upgrade I).

The impact of incorporating timing information on PV reconstruction efficiency can be observed from this analysis. This comparison shows a decline in PV reconstruction efficiency at higher occupancies when timing information is not incorporated despite the detector’s unchanged impact parameter resolution. The use of timing data, however, enhances the VELO Upgrade I’s efficiency under Upgrade II conditions. Additionally, the figure emphasises the role of timing resolution in the context of 4D-tracking, revealing that detector performance improves with better timing accuracy.

As was mentioned at the beginning of [subsection 1.1](#), to amplify the LHC’s luminosity, the High Luminosity LHC (HL-LHC) is planned for 2029. The HL-LHC is expected to produce luminosity improvements in 2029, going from  $2 \times 10^{33} \text{cm}^{-2} \text{s}^{-1}$  to  $1.5 \times 10^{34} \text{cm}^{-2} \text{s}^{-1}$  [1, 25]. Moreover, both ATLAS and LHCb will also be upgraded on their detectors by 2029 and 2035, respectively. The heightened luminosity represents a challenge in tracking complexity, as the detectors need to sustain the radioactive doses without significant loss in performance. For example, for the CMS, the radioactive doses increase from 0.84 MGy (84 mGrad) in the first 10 years of running to 12 MGy (1.2 Grad) around the accelerator in the new HL-LHC iteration [2, 25]. To address this, the RD50 Collaboration at CERN set out in 2002 to innovate the resilience of semiconductor detectors in order to handle the doses expected at the HL-LHC [26].

The research subject of the RD50 collaboration is the development of semiconductor sensors,

recognised for their particle trajectory tracking capabilities and their position of the active layer and electronics within the inner layer of particle detectors. Among these, the silicon pixel sensor stands out the most for quite some advantages. These sensors range from a few pixels to millions of pixels within the sensor, each designed for their specific needs. A promising advancement in this domain is the Monolithic Active Pixel Sensor (MAPS), characterised by integrated electronics within the silicon bulk, resulting in a singular, refined silicon wafer [5]. MAPS are more cost-effective than their competitors, primarily due to their reduced material demand and prevalent industrial usage [27].

This Master Research Project is structured around two MAPS iterations that sustained software and hardware improvements on the detector chips and surrounding electronics: the RD50-(Multi Project Wafers)3 and RD50-MPW4. While RD50's primary goal is to revolve problems around radiation resilience, this work narrows its focus on the time resolution of these sensors, another critical criterion for high luminosity settings. Employing test pulses and an infrared laser, the time resolutions of RD50-MPW2 and RD50-MPW3 in previous research yielded values of approximately 220 ps and 522 ps, respectively, for a minimal ionising particle-like laser injection [5, 6].

In summary, as particle physics continues to look beyond the Standard Model in search of new physics, the technological advancements in detector design, particularly in the realm of 4D tracking, are critical. This master thesis focuses on these technologies' current state and future prospects, aiming to contribute to the evolving landscape of high-energy particle physics.

### 1.3 Goal and Structure of this Thesis

Central to this thesis is the dual-fold problem approach: first, to precisely characterise three laser apparatuses, which have been procured to outline the characteristics of silicon detectors within the Nikhef facilities for these high-energy physics experiments. Second, the project aims to employ this setup to probe the achievable time resolution of the High-Voltage CMOS (HV-CMOS) silicon-based monolithic tracking detectors. A comparison will be made on the findings of the empirical data of the RD50-MPW3 and the RD50-MPW4, mainly focusing on their time resolution.

The following [section 2](#) delves into the technical aspects; this section describes the operational principles of semiconductor detectors, emphasising the role of HV-CMOS technology. It reviews the fundamental physics of semiconductors tailored to detecting high-energy physics applications. In [section 3](#), details of the experimental setup and instrumentation used for the tests conducted during this research. It covers the configurations of the readout systems and their optimisation for achieving enhanced time resolution. In [section 4](#), the core findings from the experimental investigations are presented. This chapter discusses the time resolution measurements of RD50-MPW3 and RD50-MPW4 detectors, analysing the effects of various operational parameters. In [section 5](#), it interprets the results and discusses the implications of the findings in the broader context. [Section 6](#) looks forward; this section outlines the next steps in research and development for HV-CMOS detectors based on the conclusions of this thesis. It suggests areas for further investigation and improvement. [Section 7](#) Summarises the thesis; this section reiterates the conclusions and the scientific contributions of the research. It also reflects on the broader impact of the work within the field of high-energy physics.

## 2 Semiconductor Based Particle Detectors

This section describes the theoretical principles related to silicon-based tracking detectors within the broader field of high-energy physics. Silicon-based tracking detectors have emerged as one of the key elements in the latest high-energy physics research. This newly acquired interest is due to their advantages over former tracking technologies such as photosensitive plates, cloud and bubble chambers, and multi-wire proportional chambers (MWPC). These early detector concepts are more limited in spatial resolution, reconstruction time, and time resolution [20].

Silicon-based tracking detectors have advanced the capabilities of high-energy physics experiments. Nevertheless, there are still opportunities for further enhancing these detectors, particularly when discussing aspects like position precision, readout speed, and time resolution. Such improvements are essential for all tracking detectors to meet the higher performance requirements set by future particle colliders such as the HL-LHC and beyond.

The high-energy physics research community has increased their efforts towards developing fast silicon tracking detectors. Detectors such as Micro-Channel Plates (MCPs) already achieve remarkable time resolutions in the few double-digit picosecond ranges, depending upon operational parameters [28]. However, these detectors are characterised by their single-channel functionality, substantial size, and relatively short operational lifespan. Due to these constraints, realising a full tracking detector with MCPs is not feasible. Nonetheless, efforts are ongoing to combine the existing advantages of silicon tracking detectors with excellent timing. This research is done both into electronics, such as front-end electronics, and fundamental principles of charge collection and sensor geometry, partially driven by future collider environments.

This section explores the basic principles of silicon-based tracking detectors. It examines the role of semiconductors and pn-junctions in detecting high-energy particles and photons. Critical subjects such as charge collection mechanisms and time resolution are discussed. This short theoretical review provides an in-depth look at the operational principles, challenges, and advancements in silicon-based tracking detectors.

### 2.1 Semiconductors

Semiconductors describe materials with electrical conductivity intermediate between conductors and insulators, which are crucial in modern technology. Their applications in everyday life span a broad spectrum, including (but not limited to) light-emitting diodes (LEDs), mobile phones, laptops, microwave ovens, and televisions. These devices utilise semiconductor properties in various configurations and designs, such as diodes, transistors, and integrated circuits. Particularly noteworthy applications are solar cells, devices that convert light into electricity, offering a sustainable and emission-free energy source and detectors utilising similar processes to make particle or photon detection possible.

This section seeks to outline the subject of semiconductor physics, specifically focusing on the evolving field of silicon semiconductor physics. The following semiconductors section is organised into six parts:

Starting with [subsection 2.1.1](#), a historical overview sets the stage, tracing the advancements and breakthroughs that have shaped semiconductor research. [Subsection 2.1.2](#) then lays the foundational principles of semiconductors, clarifying the core concepts that govern their behaviour and applications. Continuing in [subsection 2.1.3](#), focusing on the semiconductor band structures, including E vs. k diagrams and band gaps, contrasting direct and indirect gap semiconductors. Moving to [subsection 2.1.4](#), the discussion turns to intrinsic and extrinsic semiconductors, highlighting the impact of doping on carrier concentrations and semiconductor properties. The role of pn-junctions

is discussed in [subsection 2.1.5](#), explaining their creation, functionality, and the effects of external voltage on current flow at these interfaces. Concluding with [subsection 2.1.6](#), the significance of reverse bias in pn-junctions is examined, underlining its influence on the depletion region and electric field distribution, critical for optimising detector efficiency.

### 2.1.1 Historic Overview

The term 'semiconducting' originated from Alessandro Volta's phrase 'semicoibente', meaning semi-insulating, in 1782 [29]. However, it was not until the latter half of the 19th century that semiconductor physics and technology began to evolve [30]. The photovoltaic (PV) effect, a phenomenon where light is converted directly into electrical energy at the atomic level, was first documented by French physicist Edmund Becquerel in 1839 [31, 32]. This discovery laid the foundation for solar cell and detector technology. Another significant development by Albert Einstein, in his quantum theory of light, postulated the underlying mechanism of the photoelectric effect in his landmark paper. This insight earned him the Nobel Prize in Physics in 1921.

The first demonstration of ionisation signal production in a crystal of AgCl by P.J. Van Heerden in 1943 [33] marked the first step towards the use of semiconductors for detecting elementary particles. This was followed by the development of germanium detectors in 1950 [34], which introduced the concept of using reverse bias to deplete free charge, which improved electron and hole collection. The evolution of silicon technology witnessed a milestone in 1954 with the development of the first (inorganic) crystalline silicon *PV* by Chapin, Fuller, and Pearson at Bell Laboratories. This invention kickstarted the development of the conversion of photons into current through more efficient and practical means. The 1960s and 1970s witnessed rapid advancements, with the first application of silicon p-n junction detectors to high-energy particles and the fabrication of silicon strip-like sensors [35], which improved track reconstruction precision. The first practical LED was made from Gallium Arsenide Phosphide (GaAsP) by Nick Holonyak in 1962 while he was working at General Electric. The invention of charge-coupled devices in 1969 [36, 37] merged imaging and memory capabilities, further expanding the possibility of semiconductor applications in particle detection. In 1977, a remarkable discovery by Shirakawa *et al.* revolutionised the field: they observed a dramatic increase in the conductivity of doped polyacetylene upon the usage of halide vapour [38]. This groundbreaking research illustrated the potential of plastics in semiconductor applications and led to Shirakawa *et al.*, receiving the Nobel Prize in Chemistry in 2000.

This invention opened up the domain of organic semiconductors (OSC) detector physics and its inception in 1986 with the work of Tang *et al.* [39]. By the 1980s, the development of strip detectors [40] and the introduction of silicon microstrip detectors in experiments [41, 42] allowed for particle tracking and vertex reconstruction. The development of the pixel concept in 1984 [43] and its application in CERN experiments [44, 45] underscored the importance of pixel segmentation in these environments with many tracks.

The transition into the 21st century saw silicon detectors becoming integral to the infrastructure of collider experiments, with the LHC experiments demonstrating the progress [46, 47, 48, 49]. This progression from basic semiconductor materials to complex detector systems illustrates the impact of semiconductor technology on the field of particle physics, setting the stage for this thesis's exploration of detector physics advancements.

### 2.1.2 Semiconductor Basics

The classification of solid-state materials into conductors, insulators, and semiconductors is primarily based on their electrical resistivity. Semiconductors are characterised by their electrical resistivity, which lies between that of insulators (ranging from  $10^6$  to  $10^{16}$   $\Omega\text{m}$ ) and conductors ( $10^{-8}$  to  $10^{-6}$   $\Omega\text{m}$ ) [50].

Their distinct electrical properties are derived from their band structure, which allows for the thermal generation of electron-hole pairs but at a much lower rate than in conductors and prevents the thermal generation of charge carriers in insulators. This precise balance makes semiconductors particularly well suited for applications such as charged particle detection, where the ability to modulate conductivity through doping and control over the electronic environment enables the detection of minute electrical signals against low background noise.

The band diagrams map the allowed energy levels (or bands) electrons may occupy. Materials exhibit two bands: the valence band, which includes electrons in the outermost shell of the atomic structure bound to atoms, and the conduction band, consisting of free electrons that facilitate electrical conduction. These bands describe energy and momentum levels for electrons within a crystal lattice, often depicted as a function of their wavevector  $k$  in the energy versus wavevector ( $E$  versus  $k$ ) diagram, as can be seen in [Figure 2.1](#). In a semiconductor's crystalline structure, the numerous atomic energy levels due to the closely packed atoms overlap, merging into continuous energy bands. These bands represent a spectrum of energy/momentum levels where electrons and holes can exist, effectively transitioning from discrete atomic levels to a more generalised band description. These energy bands allow for an analysis of electron and hole dynamics, as further described by the literature [51].

In insulators, there exists a large bandgap, as can be seen in [Figure 2.1c](#). A bandgap is a range of prohibited energy levels between the conduction and valence bands (typically more than a few electron volts in the case of insulators) that separates these bands. This large gap prevents electrons in the valence band from acquiring sufficient energy to transition to the conduction band under normal conditions. This means that in a normal state, the number of charge carriers in the conduction band is minimal, leading to strong bonds and immobilised electrons in the valence band, hence hampering electrical conduction.

In contrast, in conductors, electrons are bound through metallic bonds [50, 51]. The conduction band overlaps with other bands, allowing the Fermi level to reside above the lowest energy state of the conduction band. This ensures charge carriers are available, even at 0 Kelvin, to facilitate conductivity. Semiconductors at 0 Kelvin have an unpopulated conduction band, similar to insulators. However, their small band gap allows the thermal excitation of electrons from the valence to the conduction band at higher temperatures, granting conductivity. Insulators also have an unpopulated conduction band at 0 Kelvin; furthermore, their large band gap prevents thermal excitation of charge carriers at room temperature, blocking conductivity. From this perspective, semiconductors bear a closer resemblance to insulators than conductors.

Semiconductors, like insulators, have a completely filled valence band but possess a much smaller bandgap (typically in the order of 1 eV). This relatively narrow bandgap facilitates the thermal excitation of some valence electrons to the conduction band at ambient temperatures, enabling conductivity. When electrons are excited to the conduction band, they leave behind vacancies (unoccupied states) in the valence band, known as "holes". These holes behave as positive charge carriers, moving through the lattice as neighbouring electrons fill the vacancy they leave behind, effectively allowing electrical conduction. Both electrons in the conduction band and holes in the valence band serve as charge carriers that enable electrical conduction through the crystal lattice [51]. Charge carrier movement is a thermal process in semiconductors that is categorised into drift,

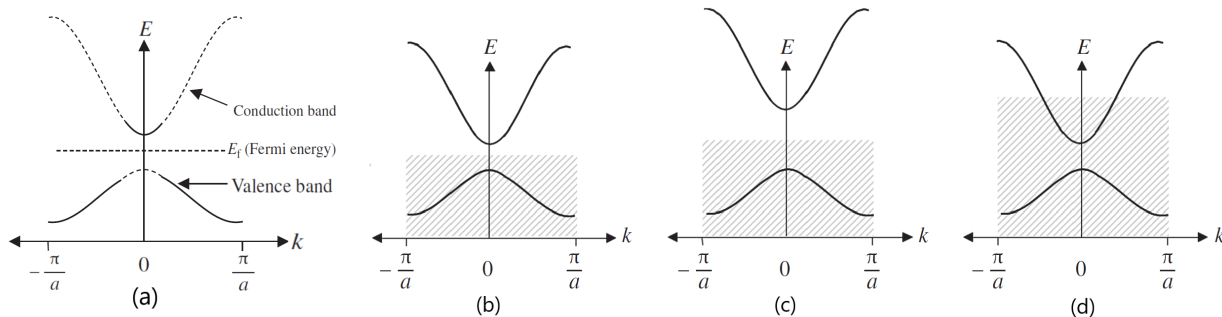


Figure 2.1: This illustrates the simplified band diagram of a semiconductor at ambient in (a). It illustrates the occupation of energy bands in (b) semiconductors, (c) insulators, and (d) metals near 0 K. Hatched areas represent filled electron states within the energy bands, while higher energy states remain vacant. Band gaps, absent of energy states, are indicated by the absence of hatching, highlighting the lack of electron presence in these regions. Image is taken from [51].

caused by an electric field, and diffusion, resulting from a movement along a density gradient.

Silicon, with its four valence electrons and a bandgap energy of 1.12 eV, is one of the most commonly used (cubic diamond structured) semiconductors in particle detectors due to its abundance on the earth and the feasibility of producing it in high purity [52].

### 2.1.3 Band Diagrams with Direct and Indirect Bandgap

Figure 2.1a depicts the semiconductor at room (ambient) temperature and in thermal equilibrium. Unlike a hard boundary on the energy axis to define occupied and unoccupied electron states, these diagrams often exhibit a more gradual transition between these states. Here, the Fermi energy,  $E_f$ , becomes a crucial concept. Represented by an imaginary horizontal line on the diagram, the Fermi energy acts as a threshold: above it, the likelihood of electron states being occupied falls below 50%, while below it, this likelihood exceeds 50%. This concept is helpful in understanding the distribution of electrons at various energy levels within the semiconductor.

While these band diagrams offer valuable insights, it's important to note that this graphical depiction of the band diagram is often a simplification and only partially captures the intricate nature of semiconductor band structures. A closer examination reveals complexities such as the presence of multiple valence bands and the nuanced determination of energy gaps in materials like Silicon and GaAs (Figure 2.2). Notably, an aspect of these band structures is the presence of multiple valence bands, which may overlap or nearly overlap, rather than a singular band. This complexity originates from spin-orbit interactions that affect the energy states of electrons in the valence band, resulting in sub-bands. Details further describing these properties can be found in the literature [51].

Conduction bands in semiconductors often have two energy minima, each defined by a parabola, to determine electron effective mass. GaAs, GaN, and CdTe are direct gap semiconductors, while silicon is an indirect gap semiconductor, leading to differences in energy gap determination. In a direct gap, only energy is needed to have interaction to create an Electron-Hole Pair (EHP) and in an indirect gap, the creation of an EHP due to photon absorption, with a shift in momentum ( $\Delta p \simeq \hbar k$ ) in the case of an indirect gap semiconductor like silicon, where  $p$  is the momentum and  $\hbar$  is the reduced Planck constant. During the creation of an EHP, both energy and momentum

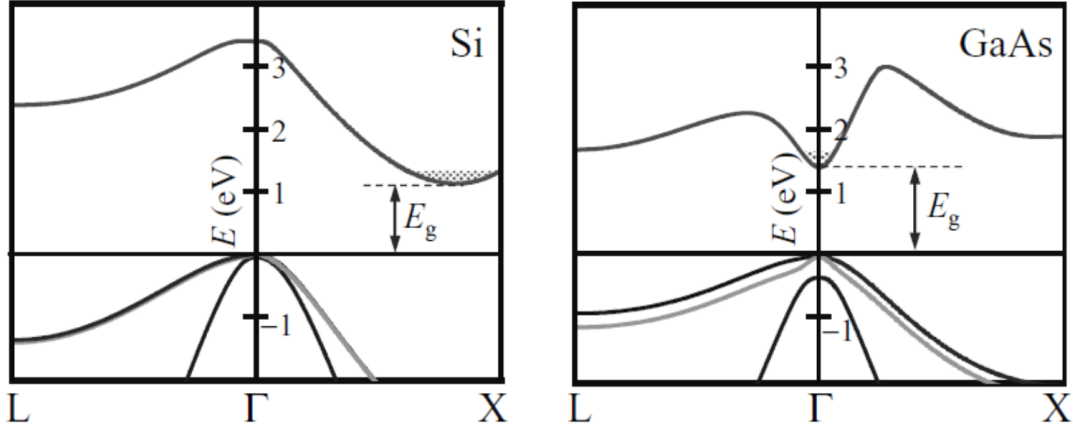


Figure 2.2: This illustrates the band diagrams of Silicon and GaAs with various band features and values. It is a simplification to only the two bands closest to the Fermi level. This way highlights the impact of the wave vector on needed excitation energy and momentum to maintain the conservation laws. Image is taken from [51].

must be conserved. The conservation of energy is satisfied since the photon energy  $\hbar\omega$  meets the condition  $\hbar\omega = E_g$ , where  $E_g$  is the bandgap energy. However, the photon momentum  $p = \frac{h}{\lambda}$  is very small and insufficient for momentum conservation. This discrepancy necessitates the involvement of lattice vibration, or phonon, in the *EHP* generation process to ensure both energy and momentum conservation.

Moreover, the necessity for phonons to have momentum conservation makes the creation of *EHP* less likely than when in a direct bandgap. The absorption of the photon and the presence of a phonon need to overlap in time and space to generate an *EHP*. Making the indirect bandgap more inefficient in the perspective of a total of incoming photons to an amount of *EHP* created. This additional step for indirect band gaps gives the indirect band gap semiconductors the property that the *EHP* generation process is more restrained than the one of a direct band gap.

For example, when focusing on the difference between Gallium Arsenide (GaAs) and silicon, we see two different types of semiconductors. The direct bandgap property is one of the reasons why GaAs as a material is often desired to be used when manufacturing high-end *PV* cells. It gives a higher efficiency, which is also the case for gallium nitride (GaN) and cadmium telluride (CdTe), all of which are direct gap semiconductors. Resulting in the fact that GaAsP was used for the first practical LED devices due to its direct gap.

So, not just the bandgap energy but the effective energy required to create an *EHP*. While the bandgap energy of silicon is lower at 1.1 eV, making it seem more accessible for *EHP* creation compared to the 1.43 eV bandgap of GaAs, silicon's indirect gap necessitates additional momentum for *EHP* creation or the absorption requiring more energy can lift it straight in the bandgap. This momentum, typically provided by phonons, means that despite its lower bandgap energy, silicon might not directly convert photons into *EHPs* as efficiently as direct gap semiconductors like GaAs. Silicon, due to its extensive research and development history, emerges as the predominant choice for high-purity and high quality in high-energy physics applications. This prominence of silicon is attributed to the perfected techniques in producing high-purity wafers over decades. However, alternative materials like gallium-arsenide [53], cadmium-telluride [54], and emerging candidates



such as diamond and silicon-carbide are being explored, with the latter two particularly garnering research interest as potential replacements for silicon (as they have larger bandgaps hence giving them higher radiation tolerance). Nonetheless, the focus of this thesis lies on silicon-based detectors, which will henceforth be the primary material discussed in the following sections.

In this subsection, we have only looked at “pure” considerations of the material. In the next subsection, [subsection 2.1.4](#), a short examination is done into the “doping” of the material and what it means for a semiconductor to be intrinsic and extrinsic.

### 2.1.4 Intrinsic and Extrinsic Semiconductors

Intrinsic semiconductors are pure semiconductor materials that naturally possess a bandgap that lends itself to semiconducting behaviour. Extrinsic semiconductors are produced by introducing specific impurities into the semiconductor; this so-called Doping modifies the charge carrier density across several orders of magnitude, enhancing the material’s electrical conductivity. This technique does not convert an insulator into a semiconductor; instead, it tailors the electrical properties of an existing semiconductor by altering the balance of electrons and holes.

When a Group V element of the periodic table, like phosphorus, is added to a silicon crystal, the phosphorus atom is substituted for a silicon atom. This introduces a spatially localised energy level, known as the donor level ( $E_d$ ) as displayed in [Figure 2.3](#). Since phosphorus has an extra electron compared to silicon, this electron does not participate in the silicon lattice’s valence bonding. It remains loosely bound to the phosphorus atom, making it easy to excite into the conduction band. Due to the donation of this additional electron, the number of electrons in the material is now larger than the number of holes, making the electrons the majority charge carriers and the holes the minority charge carriers. The energy required for this excitation, termed the donor binding energy, is given by  $E_c - E_d$ . When this donor electron enters the conduction band, it leaves a positively charged ion behind. Semiconductors doped in this specific way are referred to as n-type semiconductors.

The calculation of donor binding energy involves modifications to account for the semiconductor

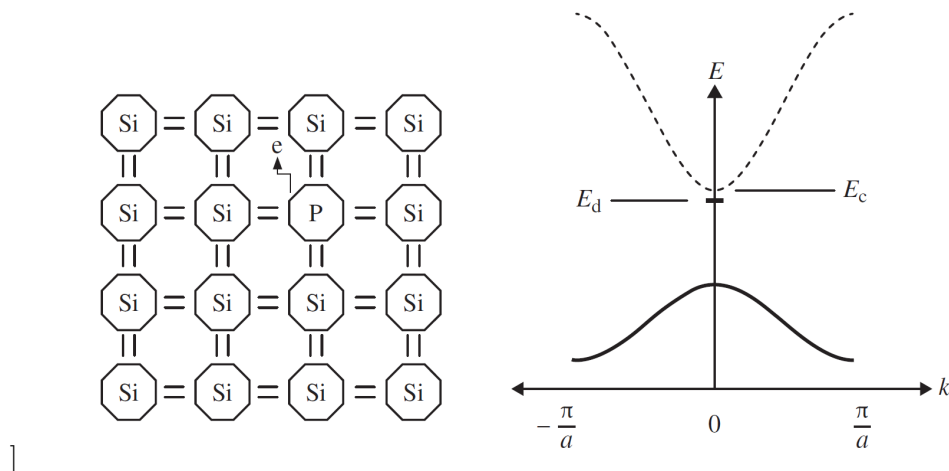


Figure 2.3: This illustrates the doping of silicon with a phosphorus atom (donor) in an n-type semiconductor. The phosphorus introduces an extra, weakly bound electron at a new energy level  $E_d$ , not needed for the crystal’s covalent bonds. A small energy gap ( $E_c - E_d$ ) allows this electron to be excited into the conduction band, creating a positively charged donor ion and adding an electron to the conduction band. Image is taken from [51].

environment, differing from a vacuum. The dielectric constant is adjusted from the free space value ( $\epsilon_0$ ) to that suitable for silicon ( $\epsilon_r$ ), and the free electron mass ( $m_e$ ) is replaced by the effective mass ( $m_e^*$ ). These adjustments result in a smaller binding energy and a larger atomic radius for the donor in silicon compared to hydrogen atoms, justifying the use of bulk silicon constants over vacuum constants.

When a Group III element of the periodic table, like Aluminium, is added to a silicon crystal, Aluminium functions as an acceptor. This introduces a new spatially localised energy level, the acceptor level ( $E_a$ ), as displayed in Figure 2.4. Aluminium's deficit of one electron compared to silicon enables it to accept an electron from another valence bond in the silicon lattice, creating a hole in the valence band. The introduction of an additional hole has increased the number of holes in the material and exceeded the number of electrons. Therefore, the holes are now considered the majority charge carriers, while the electrons are referred to as the minority charge carriers. The energy required for this process, known as the acceptor binding energy, is  $E_a - E_v$ . An accepted electron forms a hole, and the acceptor atom becomes a negatively charged ion. Semiconductors that are doped in this specific way are referred to as p-type semiconductors. Boron atoms are commonly used to dope silicon to get p-type doped silicon. The concentration of these doping atoms is typically fairly low, ranging from one dopant for every hundred million silicon atoms to one dopant for every thousand silicon atoms.

The introduction of donors or acceptors alters the concentration of charge carriers in the semiconductor. This change affects the position of the Fermi level, which is no longer at equilibrium where  $n_0 = p_0$ . However, the Fermi-Dirac distribution function remains applicable. A crucial relationship in extrinsic semiconductors is the product of the electron and hole concentrations. This distinction in carrier concentrations plays a crucial role, especially in the introduction of the pn-junction, as will be seen in the next subsection.

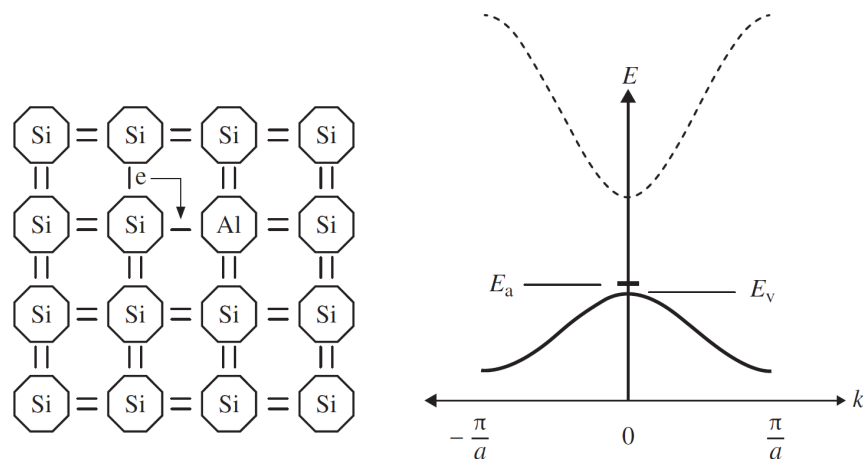


Figure 2.4: This illustrates the doping mechanism in a p-type semiconductor, where an aluminium atom substitutes in a silicon lattice. This substitution creates an incomplete valence bond at the aluminium site, requiring an electron from a nearby bond to fill it. The involved energy level, slightly above the valence band and denoted as  $E_a$ , necessitates a minimal energy transfer ( $E_a - E_v$ ). This process results in a negatively charged aluminium ion (acceptor) and an additional hole in the valence band, fundamental to the conductivity of p-type semiconductors. Image is taken from [51].

### 2.1.5 PN-Junction

A pn-junction is formed by combining p-type and n-type silicon. At this interface, due to differences in electron and hole concentrations resulting from their distinct doping types, electrons from the n-type region diffuse to the p-type region and vice versa for holes. In semiconductor- and detector physics, the pn-junction drives the operation of semiconductor devices.

This diffusion of minority carriers (electrons in p-type and holes in n-type silicon) and their recombination with majority carriers generates a current across the junction. Initially, both types of silicon are neutrally charged. This migration of majority carriers leads to the formation of negative (positive) space charges on the p-type (n-type) sides. Consequently, an electric field is established across the junction, creating a drift current. At thermal equilibrium, the drift and diffusion currents counterbalance each other. The constant Fermi level across the junction indicates equilibrium, with the Fermi level being closer to the conduction band in n-type silicon and to the valence band in p-type silicon. This results in a potential difference across the junction, known as the built-in voltage ( $V_{bi}$ ). The built-in voltage can be calculated as follows:

$$V_{bi} = \frac{k_b T}{q} \ln \left( \frac{N_a N_d}{n_i^2} \right), \quad (2.1)$$

where  $k_b$  is the Boltzmann constant,  $T$  the temperature,  $q$  the elementary charge,  $N_d$  and  $N_a$  are the donor and acceptor doping concentrations, and  $n_i$  is the intrinsic carrier concentration.

The depletion zone in a pn-junction is defined as the region absent of free charge carriers. The width of this depletion zone is determined by the built-in voltage and can be expressed as:

$$w = \sqrt{\frac{2\varepsilon_0\varepsilon_{Si}V_{bi}}{q} \left( \frac{1}{N_a} + \frac{1}{N_d} \right)}, \quad (2.2)$$

where  $\varepsilon_{Si}$  is the permittivity of silicon and  $\varepsilon_0$  is the permittivity of a vacuum.

Applying an external voltage to the pn-junction alters its behaviour. A positive potential difference greater than  $V_{bi}$  on the p-type side, known as forward bias, allows a current to flow through the junction, reducing the depletion zone width. In contrast, a negative potential, or reverse bias, inhibits current flow except for a minimal leakage current (dark current) and enlarges the depletion zone. The depletion zone width under external voltage is similar to that under built-in voltage, with the primary difference being the inclusion of the external voltage ( $V_{bi} \rightarrow V_{bi} + V_{ext}$ ) in the calculation. In practice, external voltages applied are usually much larger than the built-in voltage, leading to the latter often being neglected in the depletion zone width estimation. Hence, the function for the depletion zone is as follows:

$$w = \sqrt{\frac{2\varepsilon_0\varepsilon_{Si}(V_{bi} + V_{ext})}{q} \left( \frac{1}{N_a} + \frac{1}{N_d} \right)} \approx \sqrt{\frac{2\varepsilon_0\varepsilon_{Si}V_{ext}}{q} \left( \frac{1}{N_a} + \frac{1}{N_d} \right)}. \quad (2.3)$$

### 2.1.6 Reverse Bias in PN-Junctions of Silicon Detectors

Planar silicon sensors employ pn-junctions, where a significant discrepancy exists between the doping concentrations of the two regions. In such junctions, the depletion region predominantly extends into the more lightly doped area, which constitutes the bulk silicon from which the sensor is fabricated. Conversely, the more heavily doped region, referred to as the implant, is situated at the surface and characteristically exhibits a shallow depth.

**Depletion Region Dynamics** The influence of reverse bias voltage on the depletion region's thickness is critical for sensor operation. Basically, in non-depleted regions, there is no electric field, so it cannot collect the charge before it typically recombines. As illustrated in Figure 2.5, the depletion region thickness varies as a function of a reverse bias voltage across a spectrum of bulk doping concentrations. For this analysis, an implant doping concentration of  $10^{19} \text{ cm}^{-3}$  is posited for the implant. It is worth noting that as long as the implant doping concentration substantially exceeds that of the bulk, the precise rough order of magnitude of the implant doping does not significantly alter the depletion region's behaviour.

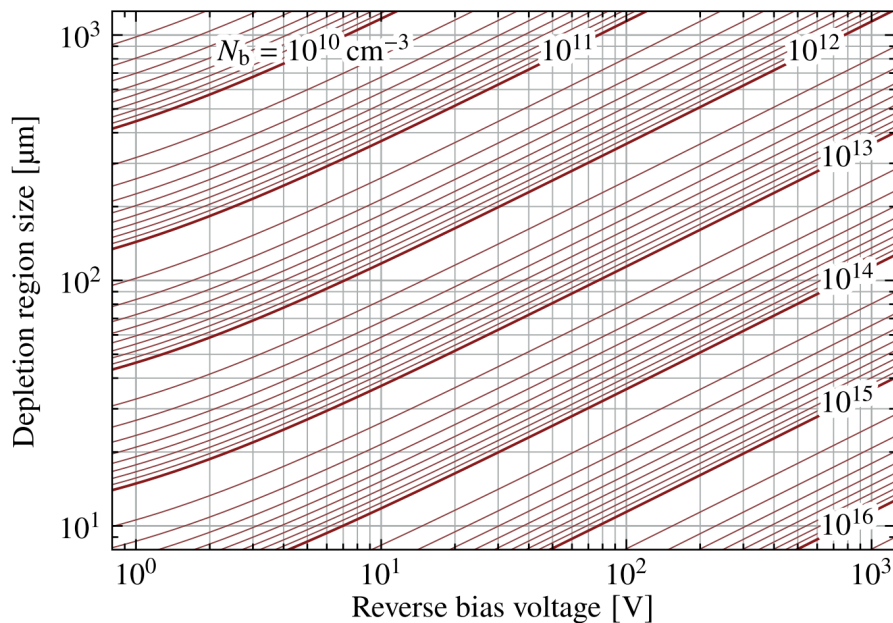


Figure 2.5: Variation of depletion region thickness with reverse bias voltage across different bulk doping concentrations, assuming an implant doping concentration of  $10^{19} \text{ cm}^{-3}$ . Image is taken from [19].

**Electric Field Distribution** Furthermore, the distribution of electric field strength within the pn-junction under varying reverse bias voltages is depicted in Figure 2.6, considering a bulk doping concentration of  $10^{12} \text{ cm}^{-3}$ . The electric field strength within the junction is a key factor, as it influences the efficiency of charge carrier separation and collection within the silicon-based sensor and if there is no electric field, the charge cannot be collected before it typically recombines.

In the following section 2.2, we delve into the specifics of how silicon, exploiting the dynamics of the depletion zone, functions as an effective material for detecting and analysing charge carriers generated by particle interactions. Thereby explain the detection mechanism employed in silicon-based tracking detectors.

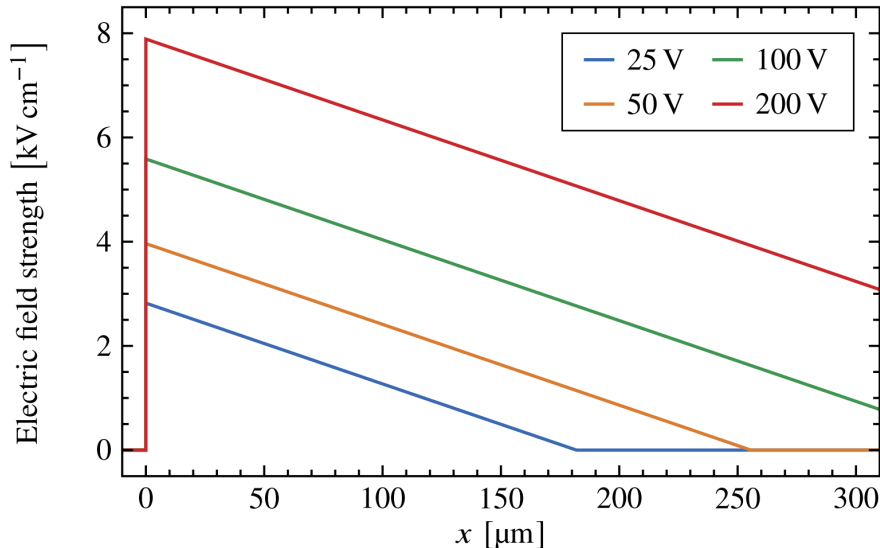


Figure 2.6: In this figure, the variation of electric field strength across a pn-junction, the influence of reverse bias voltages at a bulk doping concentration of  $10^{12} \text{ cm}^{-3}$  and an implant doping concentration of  $10^{19} \text{ cm}^{-3}$  are displayed. Image is taken from [19].

## 2.2 Silicon as the Detector Material

This section clarifies how particles interact with silicon to produce these charge carriers. As was mentioned in [section 2.1](#), in silicon, electrons within the valence band can be excited to higher energy states in the conduction band through various electromagnetic interactions. The interaction of charged particles or photons with valence electrons can excite them to the conduction band, resulting in the formation of *EHPs*. Due to the application of an external bias voltage, a depletion of free charge carriers in the silicon detection volume is provided. This depletion region is empty of free charge carriers and, therefore, establishes an electric field across. This electric field will swiftly separate and drive any newly produced *EHPs* resulting from the traversal of particles towards the electrodes. This movement of charge carriers towards the electrodes is the detection mechanism, converting the interaction into an electrical signal detectable by the detector's readout electronics.

Pixelated and strip-based silicon detectors typically consist of a silicon bulk of either p- or n-type, complemented by an implant of the opposite type (n- or p-type), although configurations like n-type bulk with n-type implant also exist. Detector designs vary based on the bulk material used. If the bulk is p-type (n-type), the design is termed p-on-n (n-on-p). The primary distinction lies in the type of charge carrier drifting towards the implant: electrons in n-on-p and holes in p-on-n. This difference significantly influences the speed and functionality of the detector, particularly in advanced sensor designs like 3D sensors and Low Gain Avalanche Diodes (LGADs) [55, 56].

Silicon-based tracking detectors can detect photons and charged particles. The interactions of these particles with silicon, though similar, have subtle differences. Silicon, being an indirect semiconductor, presents a momentum mismatch between the states at the top of the valence band and the bottom of the conduction band, as depicted in [Figure 2.2](#). Excitation of an electron across the bandgap requires a change in momentum, often provided by phonons as the lattice vibrations. This process is temperature-dependent due to the increased presence of phonons at higher temperatures [57, 58]. Conversely, for excitations by charged particles, the mean energy transfer per electron-hole pair creation is approximately 3.6 eV, known as the mean pair-creation energy in silicon. This higher energy transfer does not necessitate already existing phonons from

the lattice. Despite the differing excitation processes for photons and charged particles, both result in the creation of detectable electron-hole pairs.

The section is organized into three parts:

First, [Subsection 2.2.1](#) examines the interaction between charged particles, photons, and detector materials, employing the Bethe-Bloch equation to explain energy loss and discussing photon interaction mechanisms. This foundation is critical for designing effective high-energy physics detectors. Proceeding to [subsection 2.2.2](#) addresses the statistical nature of energy loss in materials, focusing on Landau's distribution and the impact of stochastic processes like delta ray production. Advanced models that improve energy loss predictions are vital for optimizing silicon-based tracking detectors. Lastly, [subsection 2.2.3](#) explores the influence of drift velocity on semiconductor detector performance. It highlights the effects of electric fields, doping on mobility, and the challenges of high electric fields and saturation velocity, essential for detector design and functionality.

The next [Subsection 2.2.1](#) will delve deeper into the mechanisms of a particle travelling through and interacting with matter, utilizing the Bethe-Bloch equation for a more comprehensive understanding.

### 2.2.1 Particles Interacting with Matter

Charged particles are detected primarily through their interactions with matter. The interactions can manifest in various forms, and the choice of the detection mechanism often depends on factors such as the energy range, the incident particle's mass, and the specific requirements of the measurement (calorimetry, tracking, or particle identification). This subsection defines the principles that control the interactions of charged particles with matter, focusing on excitation and ionisation processes, as these are closely related to the measurements involving Minimum Ionizing Particles (MIPs) discussed in subsequent sections. For a broader scope of interaction mechanisms, readers are directed to reviews available in the literature [63, 64].

The Bethe-Bloch equation offers a description of the mean energy loss of charged particles due to electronic interactions traversing through material. To better understand the *Bethe-Bloch* equation's application, a further examination of [Figure 2.7](#) is required. It shows that the mass stopping power quantifies the energy loss per unit mass of the absorber material. Expressed typically in  $\text{MeV cm}^2 \text{g}^{-1}$ . [Figure 2.7](#) shows the mass-stopping power for various charged particles in silicon.

Notably, the mass-stopping power remains relatively constant across different materials, slightly decreasing with an increase in the material's atomic number [64]. This figure also breaks down the energy loss into contributions from excitation, nuclear recoil, radiative losses, and ionisation, including photonuclear interactions, bremsstrahlung, and direct pair production.

This Bethe-Bloch equation is valid in the range of  $0 \leq \beta\gamma \leq 1000$ , where  $\beta$  is the velocity of the particle relative to the speed of light ( $\frac{v}{c}$ ), and  $\gamma$  is the Lorentz factor. The energy loss is approximated by the *Bethe-Bloch* equation [65]:

$$\left\langle -\frac{dE}{dx} \right\rangle = Kz^2 \frac{Z}{A} \frac{1}{\beta^2} \left[ \frac{1}{2} \ln \left( \frac{2m_e c^2 \beta^2 \gamma^2 T_{max}}{I^2} \right) - \beta^2 - \frac{\delta(\beta\gamma)}{2} \right], \quad (2.4)$$

where the equation incorporates various parameters including the bremsstrahlung photon energy ( $K$ ) as can be seen in [Equation 2.5](#), the maximum energy transferable in a single collision ( $T_{max}$ ) as can be seen in [Equation 2.6](#):

$$\begin{aligned} K &= 4\pi N_A r_e^2 m_e c^2 \\ &= 0.307075 \text{ MeV cm}^2 \text{ mol}^{-1}, \end{aligned} \quad (2.5)$$

$$T_{max} = \frac{2m_e c^2 \beta^2 \gamma^2}{1 + 2\gamma m_e/m + m_e^2/m^2}, \quad (2.6)$$

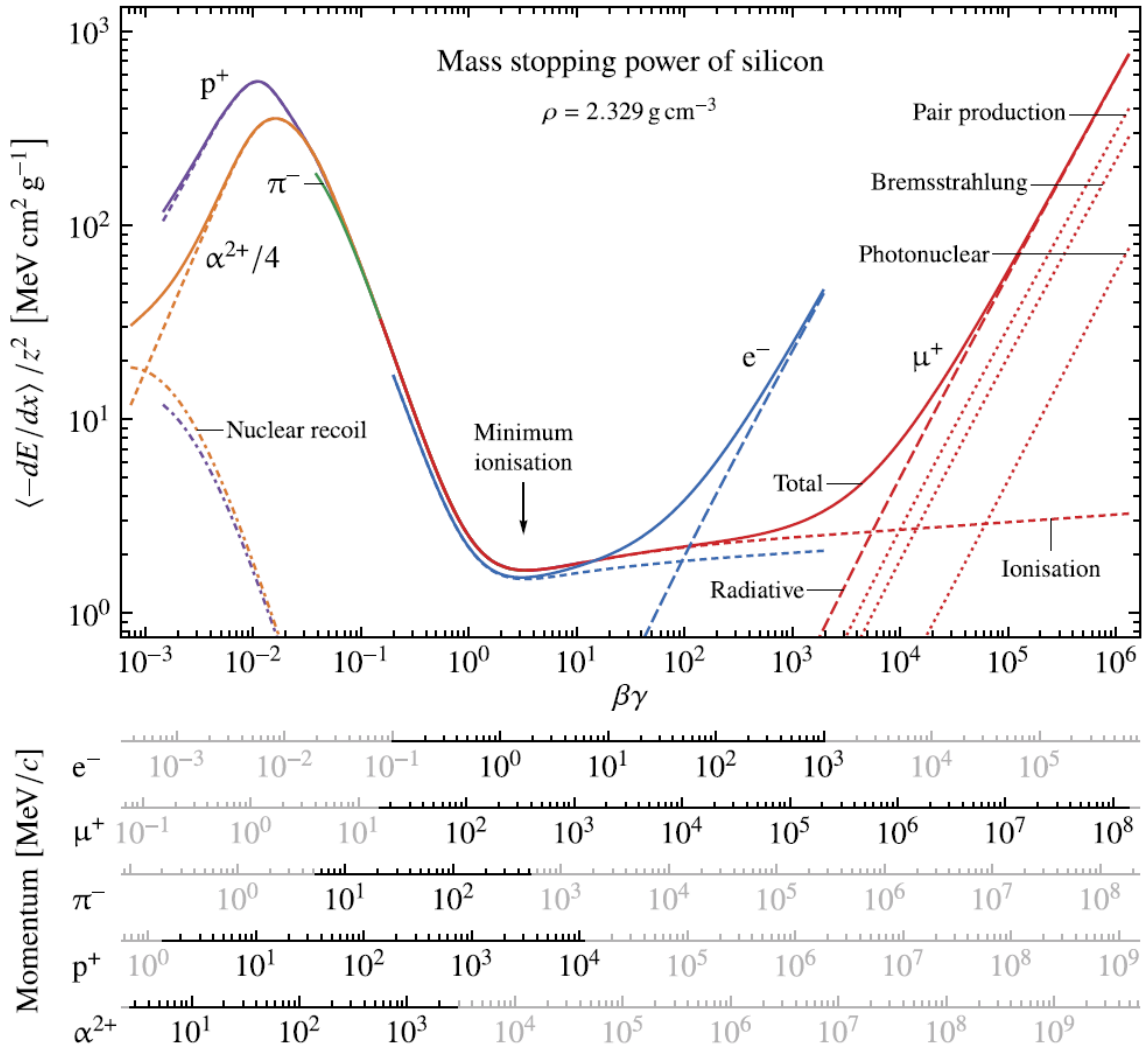


Figure 2.7: Depiction of the mass stopping power of silicon, expressed as a function of particle velocity for particle types including protons [59], electrons [60], alpha particles normalised respective to the square of their charge number [61], and muons [62]. The figure illustrates the interaction mechanisms within various sectors of the momentum spectrum. Notably, the mass stopping power reaches its maximum at the low or high levels of the momentum range, which suggests an increase in interaction rates for particles possessing either minimal or maximal momentum. The vicinity of a  $\beta\gamma$  value approximating 3 is designated as the 'minimum ionising' zone. Image is taken from [19].

the atomic number ( $Z$ ), the charge number of the incident particle ( $z$ ), the mass ( $A$ ) of the absorber, the mean excitation energy ( $I$ ) which is approximately proportional to its atomic number ( $I \sim Z^{0.9} \cdot 16 \text{ eV}$  [63]), experiments have found a value of 173(3) eV for silicon [66], the speed of light ( $c$ ), the electron mass ( $m_e$ ), and the density effect correction to ionisation energy loss  $\delta(\beta\gamma)$ . The latter accounts for the reduced energy loss at high relativistic velocities, becoming increasingly significant in denser materials. Thus, the energy transfer process is bounded by two limits.

The minimum energy transfer threshold is determined by the energy required to excite or ionise an electron from its atomic state. The upper limit of energy transfer, on the other hand, is constrained by momentum conservation laws in the interaction. This upper limit depends on the

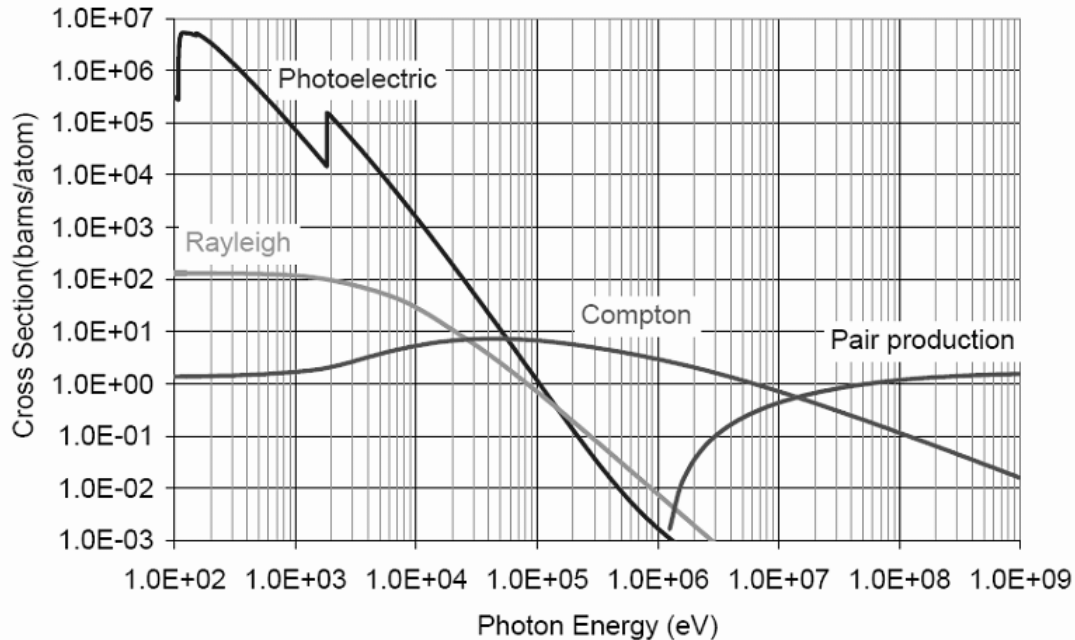


Figure 2.9: Partial Cross-Sections of Photon-Material Interaction Mechanisms in Silicon. This figure delineates the varying cross-sections for photon-material interaction processes in silicon across a range of photon energies. It illustrates how different mechanisms, such as the photoelectric effect, Compton scattering, electron-positron pair production, and Rayleigh scattering, exhibit various cross-sectional distributions depending on the energy of the incident photons. Image is taken from [67].

mass and velocity of the incoming particle and the mass of the electron. These energy transfer limits predict the behaviour of particles as they pass through materials.

The 'minimum ionising' zone (as seen in Figure 2.7) will produce the most often measured particle in LHC, particles called Minimum Ionizing Particles (MIP)'s. The *MIP* energy deposition is the most influential considered particle energy in detector design in this field of research. It will accommodate the 'worst' possible case scenario in terms of deposited energy for the relevant experiments. Therefore, detectors are measured for their performance in this worst possible case, such that the measurable range never falls below the *MIP* energy deposition range.

For a detailed exploration of particle interactions with matter, energy loss mechanisms, and the specifics of the Bethe-Bloch equation, see Appendix A.1.

Photons are chargeless particles that mediate the electromagnetic force. Their ability to interact with charged particles is fundamental in particle detection. Several processes govern these interactions, most notably Compton scattering, the photoelectric effect, electron-positron pair production, and Rayleigh scattering [64, 63]. Each of these mechanisms has distinct characteristics and regions depending on the photon energy and the material with which they interact.

Figure 2.9 presents the interaction cross-sections for these different photon interaction mechanisms as a function of photon energy.

Within the used energy range, the photoelectric effect emerges as the predominant mechanism for photon interaction. This effect involves the absorption of a photon by an atom in the detector material, leading to the excitation of an electron. This excitation can either propel the electron to a higher energy state or liberate it entirely from the atom, resulting in ionisation. The ionisation



process occurs when the photon energy is sufficient to overcome the binding energy of the electron to the atom. Photons with energies typically below 100 keV are most effective in inducing the photoelectric effect.

While the photoelectric effect is predominant at lower energies, other mechanisms, such as Compton scattering and electron-positron pair production, become significant at higher photon energies. Compton scattering involves the inelastic scattering of a photon by a loosely bound outer electron, resulting in a change in the photon's direction and a decrease in its energy. Electron-positron pair production, on the other hand, occurs when a high-energy photon interacts with the electric field of a nucleus or an electron, leading to the creation of an electron-positron pair. A detailed examination of these processes is available in [64].

While the Bethe-Bloch equation provides an average energy loss, it does not accurately describe the energy loss for individual particles due to the skewed distribution resulting from rare hard collisions. These collisions can transfer significant energy to a single electron, producing a delta ray. Delta rays are electrons that acquire sufficient kinetic energy to ionise absorber atoms at a distance from the primary particle's track. Their behaviour and the resultant fluctuations in energy loss significantly impact the time resolution of silicon-based tracking detectors and are further mentioned in [Appendix A.2](#) and shortly discussed in [subsection 2.2.2](#).

### 2.2.2 Energy Loss Fluctuation

The concept of mass stopping power, as defined by Bethe Bloch ([Equation 2.4](#)), relates to the mean energy loss of a charged particle traversing a specific absorber material. Particularly for *MIPs*, this mean energy loss does not reliably represent the energy loss of individual particles due to the skewed nature of the energy loss distribution. This skewness arises from relatively rare but quite hard collisions, where energy is transferred to a single electron, resulting in the generation of a delta ray. Upon losing their energy, such electrons may exit the sensor material, thereby not contributing to the signal formation in the detector. The variability in energy loss is a factor influencing the time resolution of silicon-based tracking detectors.

[Figure 2.10](#) illustrates the Landau energy loss distribution for 180 GeV/*c* protons traversing silicon sensors of varying thicknesses. Notably, the stopping power derived from Bethe's equation mainly resides in the distribution's tail, highlighting the distinction between average and most probable energy losses in high-energy interactions.

To quantify the energy deposition in silicon, the secondary horizontal axis of [Figure 2.10](#) represents the number of *EHPs* generated per unit path length within the detector. This estimation is predicated on the assumption that the entire energy of the incident particle is absorbed by the material. Given that the average energy required to create a single *EHP* in silicon is approximately 3.62 eV, this axis allows for a direct correlation between energy loss and charge carrier generation [63].

The peak of the Landau energy loss distribution ([Equation A.6](#)) is the most probable energy loss, defined as:

$$E_{\text{mp}} = \xi \left( \log \frac{2m_e c^2 \beta^2 \gamma^2 \xi}{I^2} + 0.2000 - \beta^2 - \delta \right), \quad (2.7)$$

which was postulated in [68].

For a more detailed look at fluctuations in energy loss that impact the time resolution, look in [Appendix A.2](#).

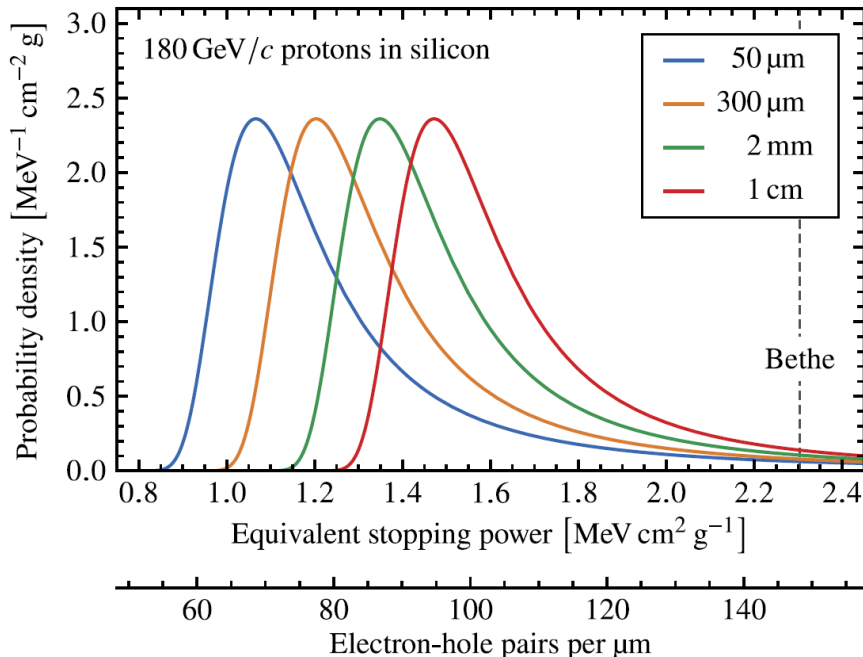


Figure 2.10: This figure illustrates the Landau energy loss distributions as a function of sensor thickness for protons with a momentum of 180 GeV/c traversing silicon. The distributions showcase the variability in energy loss dependent on the thickness of the silicon sensor. Additionally, the mean stopping power calculated by Bethe’s formula is shown for comparison, further illustrating its position relative to the Landau distribution tails. Image is taken from [19].

### 2.2.3 Drift Velocity in Detectors

The drift of charge carriers, a fundamental aspect of charge transport in semiconductor detectors, is governed by the application of an electric field across the junction. According to the Drude model [69, 70], the equation of motion for a charge carrier under an electric field  $E$  is given by:

$$m_{\text{eff}} \left( v_D + \frac{v_D}{\tau} \right) = qE, \quad (2.8)$$

where  $q = \pm e$  represents the charge of the carrier, taking a negative value for electrons and a positive value for holes, and  $m_{\text{eff}}$  denotes the effective mass of the charge carriers. The parameter  $\tau$ , known as the relaxation time, encompasses factors such as scattering within the lattice and can be interpreted as the average time between successive collisions of the charge carriers.

In a steady-state scenario, the drift velocity  $v_D$  is considered to be constant, essentially approximating to zero. This assumption simplifies the analysis of drift motion, leading to the following expression for the drift current:

$$j_{\text{drift}} = \sigma E, \quad (2.9)$$

where  $\sigma = nq\mu$  is the electrical conductivity,  $\mu = \frac{q\tau}{m_{\text{eff}}}$  is the mobility factor, representing the ease with which the carriers can move through the semiconductor material, and  $n$  denotes the charge carrier density. The mobility factor is pivotal in determining the efficiency and speed of charge transport in the detector material.

The charge transport by drift governs the dynamics of charge carrier movement in response to applied electric fields in silicon sensors. It underlines the principles governing the detectors’

temporal and spatial resolution, as well as their overall sensitivity and performance under varying experimental conditions.

Manipulating the electric field within the sensor can enhance the temporal resolution of semiconductor detectors. Practically, the application of high-bias voltages can induce electric discharges, potentially causing irreversible damage to the detector. Moreover, a breakdown can occur at approximately  $3 \times 10^5 \text{ V cm}^{-1}$  [71]. Beyond this threshold, electron multiplication might ensue, leading to a rapid increase in leakage current and consequent sensor damage; however, in iterations of the LGAD, the multiplication did not cause sensor damage. It should be separately looked at on a case-on-case basis.

A critical theoretical limitation arises from the concept of saturation velocity. As the electric field strength increases, so does the energy of electrons and holes. This heightened energy begins to interact more forcefully with the lattice, transferring energy in the form of optical phonons, which are out-of-phase movements of atoms within the lattice structure [72]. Such energy transfers can diminish the velocity of charge carriers, culminating in an upper limit to the drift velocity.

Another factor influencing drift velocity is the mobility of electrons and holes in doped silicon, particularly at high doping concentrations ( $N > 10^{16} \text{ cm}^{-3}$ ). Experimental observations indicate that electron mobility varies with donor concentration [73, 74], while hole mobility is affected by acceptor concentration. Both mobilities diminish as doping concentration increases. However, due to the relatively thin, highly doped regions around the implants, this decrease in mobility does not significantly impact the resolution of current silicon sensors.

## 2.3 Pixel Detectors

Pixel detectors have become a cornerstone in the field of high-energy physics and detector technology. The basic structure of a pixel detector typically involves a p-doped silicon substrate with n-doped regions. However, for today's applications in high-energy physics, most detectors use n-doped silicon substrates with p-doped regions (this way, it suffers less from type inversion) configured in a grid, forming an array of diodes. The spatial separation between the centres of these diodes, known as the pixel pitch, is a parameter in detector design.

The CERN RD50 collaboration is dedicated to the development of semiconductor devices engineered to withstand the extreme radiation environments anticipated at very high luminosity collider experiments. With the coming of the *HL-LHC* and the prospective *FCC-hh*, detectors are required to endure neutron equivalent fluences exceeding  $\Phi_{\text{eq}} > 10^{16} \text{ cm}^{-2}$  and reaching up to  $\Phi_{\text{eq}} = 6 \times 10^{17} \text{ cm}^{-2}$ , respectively [5].

### Types of Pixel Detectors

Pixel detectors are categorised into two types, mainly differing in the integration of the analogue front end and digital readout. These two iterations will be discussed down below in [subsection 2.3.1](#) and [subsection 2.3.2](#). In a hybrid pixel detector ([subsection 2.3.1](#)), the sensor and the readout electronics are separate entities connected via bump-bonding. In a monolithic pixel detector ([subsection 2.3.2](#)), the readout electronics and the sensor part are integrated into the same substrate. Monolithic sensors refer both to the CMOS (Complementary Metal Oxide Semiconductor) pixel sensors ([subsection 2.3.2](#)) and the Depleted Monolithic Active Pixel Sensors (DMAPS) ([subsection 2.3.3](#)).

### 2.3.1 Hybrid Pixel Detector

Hybrid pixel detectors are depicted in Figure 2.11 and represent the most commonly used pixel detectors used in many large-scale experiments, such as the *ATLAS* Tracking Detector and the *CMS* Tracking Detector and their respective upgrades for the *HL-LHC* due to their Modularity, Flexibility, and Customization [2, 75].

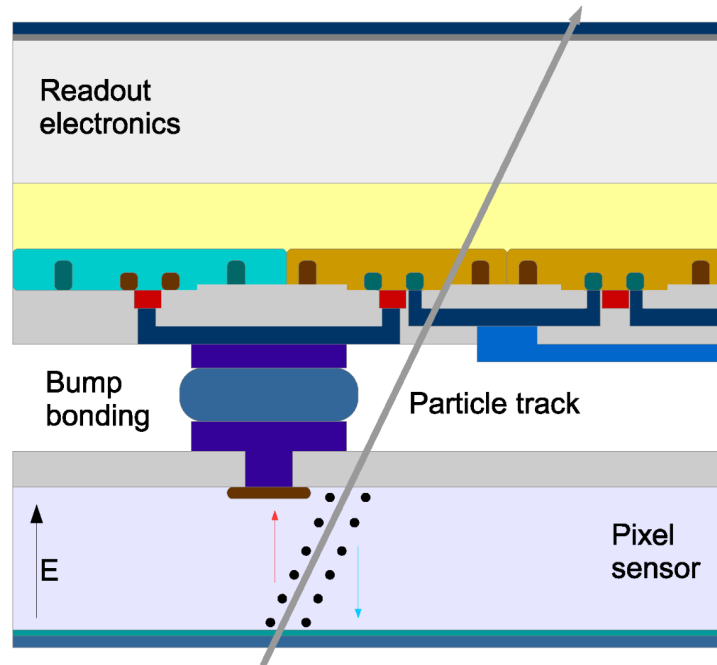


Figure 2.11: A schematic representation of a Hybrid Pixel Detector. This diagram illustrates the operational principle of a hybrid pixel detector in response to an ionising particle. As the particle traverses the sensor, it generates *EHPs*. These charge carriers then drift towards the depletion region under the influence of an applied electric field. The accumulated charge in this region is subsequently converted into electrical signals by the underlying readout electronics. Image is taken from [27].

Hybrid pixel detectors represent a technology where the readout electronics and the sensor are distinct entities connected via bump-bonding. This modular design, as showcased in Figure 2.11, offers several advantages and challenges:

#### Advantages

- **Modularity:** The separate components in hybrid detectors allow for individual upgrading or replacement. This modularity is particularly beneficial when adapting the detector for different experimental setups or when upgrading to newer readout technologies without needing to replace the entire detector.
- **Flexibility and Customizability in Design:** Hybrid detectors enable the use of different materials for the sensor and the electronics, allowing each to be customized electronically for specific purposes to get the best performance, such as the LHCb's VELO or to engineer versatile solutions suitable for a broad spectrum of scientific inquiries, as demonstrated by

the Timepix detector arrays. Each component can be individually tailored to maximize performance in its specific role, enhancing overall detector efficiency and adaptability.

### Challenges

- **Complex Assembly:** The bump-bonding process used to connect the sensor and electronics is technically challenging, expensive, and not done on a large scale in the industry. This complexity limits the production rate and increases the overall cost of the detectors.
- **Material Budget:** The layered structure of hybrid pixel sensors contributes to a larger material budget. This increased material can cause increased multiple Coulomb scattering, potentially degrading the spatial resolution and tracking performance of the detector.

**Applications:** Due to their high-resolution capabilities and robustness, hybrid pixel detectors have been successfully implemented in various high-energy physics experiments, such as in the current *ATLAS* and *CMS* hybrid detectors, highlighting the potential for hybrids when using their modularity. Their modular design, which allows for the independent optimization of sensors and Application-Specific Integrated Circuits (ASICs), affords these detectors a unique adaptability. Hybrid pixel sensors are ideal for experiments demanding excellent spatial resolution and rapid data acquisition. Nonetheless, their applicability might be constrained in scenarios where material budget and sensor thickness are important considerations and where a large area needs to be instrumented due to their higher cost per square meter. It is worth noting that the spatial resolution performance at the current state of development is similar between hybrid and monolithic structures.

#### 2.3.2 CMOS Monolithic Pixel Detectors

A contrasting approach to the hybrids is seen in monolithic pixel detectors, also known as CMOS (Complementary Metal Oxide Semiconductor)-monolithic pixel detectors [27]. *CMOS* monolithic pixel detectors describe and represent the less commonly used pixel detectors in large-scale experiments. The development is still in an early stage of integration compared to the hybrids. However, the ALPIDE (ALice PIxel DETector) is a *CMOS* monolithic pixel detector and demonstrates superior spatial resolution compared to current *ATLAS* and *CMS* hybrid detectors. In *CMOS*, the readout electronics and sensing diodes are integrated into the same substrate, as can be seen in Figure 2.12 and in Figure 2.13.

The electronics within the CMOS structure are layered on top of a high-resistivity base. This layering includes the integration of NMOS (n-type Metal-Oxide-Semiconductor) and PMOS (p-type Metal-Oxide-Semiconductor) transistors within distinctly doped wells. With its resistivity, the epitaxial layer serves as the sensing volume, ensuring charge collection efficiency and minimizing electronic noise [76]. Monolithic Active Pixel Sensors (MAPS) represent an integration of *CMOS* technology with a sensitive p-n diode element, resulting in a monolithic sensor architecture that includes integrated readout electronics. This integration eliminates the necessity for complex and expensive interconnection methods like bump bonding. The charge collection in these sensors occurs within a high-resistive p-type epitaxial layer that also accommodates the embedded readout electronics. Charge carriers are primarily collected through an n-type implant; additional deep p-well implants are utilized to encapsulate PMOS transistor-housing n-wells, mitigating parasitic charge collection. Since these detectors operate without biasing beyond their intrinsic electric fields, diffusion is dominant as the charge collection mechanism. Consequently, such *MAPS* are

not well suited for environments with high particle rates and substantial radiation levels, like those encountered in *ATLAS*, which necessitate drift-dominated charge collection mechanisms.

The construction of a *CMOS* wafer incorporates diverse manufacturing techniques and materials to optimize its functionality. Contrary to standard processes in CPU and GPU manufacturing, which often employ low-resistivity silicon substrates produced via the Czochralski method, advanced particle detection applications necessitate silicon wafers with higher resistivity. This enhances charge collection efficiency and reduces leakage currents in detector environments.

Typical resistivity of p-substrate for CPUs/GPUs  $\approx$  few tens of  $\text{m}\Omega \cdot \text{cm}$  (Czochralski method)

Resistivity for particle detection applications  $\approx$   $\text{k}\Omega \cdot \text{cm}$  (Float-zone or Epitaxial growth)

There are also *MAPS* that use adapted designs with high resistivity materials to reach larger depletion regions for improved radiation hardness and efficiency. These are referred to as Depleted Monolithic Active Pixel Sensors (DMAPS), most commonly used in high-energy physics. For instance, RD50-MPW3 utilizes a substrate with a resistivity of  $1.7 \text{ k}\Omega \text{ cm}$ , while the current iteration, RD50-MPW4, features an even higher resistivity of  $3.0 \text{ k}\Omega \text{ cm}$ . The float-zone-based substrate can be depleted by applying high voltage. In scenarios where the electronics are not protected from such a high voltage, such as the *ALICE MAPS*, an epitaxial growth with even higher resistivity is used to ensure depletion even at low voltages.

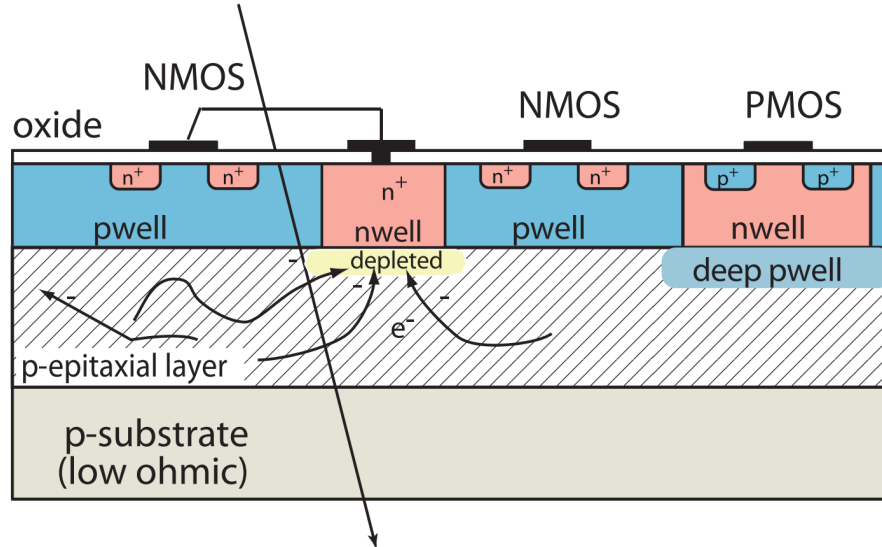


Figure 2.12: A simplified representation of a *MAPS* cross-section closely affiliated to the *CMOS*, integrating photodiodes and readout electronics on a single silicon substrate. The sensor's active region, formed by a p-n junction between the photodiode and the substrate, facilitates charge generation and separation upon photon or particle interaction. *MAPS* primarily rely on diffusion for charge collection within an epitaxial layer. Image is taken from [77].

### 2.3.3 Depleted Monolithic Active Pixel Sensors (DMAPS)

*DMAPS* represent an advance in pixel detector technology. Unlike traditional CMOS sensors, *DMAPS* incorporate high-voltage or high-resistivity processes to extend the depletion region within the silicon substrate, it also does not require any interconnection such as bump bonding. This design enables efficient charge collection. Introduced in the early 1990s as an alternative to Charge-Coupled Devices (CCDs) in visible imaging, *DMAPS* have since been recognized for their potential in high-energy physics due to their fabrication compatibility with standard commercial technology processes [78].

The maximum depletion thickness in *DMAPS* is dependent on the *CMOS* process that is used, the inherent p-substrate resistivity, and the maximum allowable bias voltage. The ideal operational scenario is total depletion of the sensor, which is influenced by the overall thickness of the *DMAPS*, typically ranging between 30  $\mu\text{m}$  and 300  $\mu\text{m}$ .

In *DMAPS*, pixel electronics are situated within an isolated n-well. The choice between a charge-sensitive amplifier and a voltage amplifier for signal conversion depends on the sensor's capacitance. A voltage amplifier is implemented for very low input capacitances ( $\sim 100$  fF). The noise level in the detector is directly proportional to the total capacitance at the input of the amplifier, making the detector capacitance a critical factor in maintaining low noise levels. This sensor technology presents a notable advancement in terms of noise minimization and enhanced signal sensitivity when contrasted with traditional hybrid pixel detectors. The integrated design and fabrication processes employed in this technology contribute to a reduction in electronic noise.

Figure 2.13 provides simplified illustrations of the *DMAPS* cross-section structures, highlighting the design considerations that enable deep depletion and efficient charge collection. The extent of sensor depletion is influenced by the material's resistivity and the applied bias voltage, suggesting that extensive depletion can be achieved through either the use of materials with high resistivity, the application of high bias voltages, or a combination of both. Based on these criteria, detectors are often classified into two categories: HR-CMOS (High-Resistivity *CMOS*) and HV-CMOS (High-Voltage *CMOS*), though the distinction between them can be somewhat indistinct. Both types aim to achieve deep depletion and efficient charge collection but utilize different approaches to realize these objectives. Typical *DMAPS* designs target depletion depths within the range of 50 to 100 micrometres. However, depletion depths as shallow as 20 micrometres are also achievable in configurations optimised for low noise.

**HR-CMOS (ALICE):** *HR-CMOS* technology is used in instruments such as the ALICE (A Large Ion Collider Experiment) Inner Tracking System (ITS) at CERN. This technology harnesses the advantages of commercial CMOS processes while incorporating a high-resistivity epitaxial layer, enabling enhanced charge collection efficiency and radiation hardness essential for particle detection in collider experiments. In traditional CMOS sensors, the signal charge is primarily collected by diffusion, which can be adversely affected by radiation-induced traps, leading to lowered tolerance. However, *HR-CMOS* sensors, like the *ALPIDE* used in the *ALICE ITS* upgrade, integrate a high-resistivity epitaxial layer exceeding 1 k $\Omega$  cm. This layer improves charge collection by facilitating a larger depletion volume when a moderate reverse bias voltage (typically on the order of a few volts) is applied to the substrate. The depleted region ensures a more efficient charge collection through drift, reducing the reliance on diffusion and thus mitigating the impact of radiation-induced defects [79].

**HV-CMOS (RD50-MPW and Mupix/Atlaspix):** *HV-CMOS* technology, including the RD50-MPW series and Mupix/Atlaspix, incorporate high-voltage processes to extend the depletion zone across the bulk silicon. This technology uses reverse biasing at high voltages, ensuring efficient charge collection across a more extensive volume. The innovation in *HV-CMOS* lies in its ability to collect electrons predominantly in an isolated n-well, which, in addition, houses all electronics, leveraging quick charge collection mechanisms due to the uniformity of the collection electrode as well as shielding the sensitive electronics from the high voltage applied to the substrate. This allows for bias voltages on the order of hundreds of volts. Further improving collection speed, depletion depth and radiation hardness. This strategic approach not only facilitates rapid charge collection but also minimizes the sensor’s susceptibility to noise, thereby enhancing its time resolution capabilities.

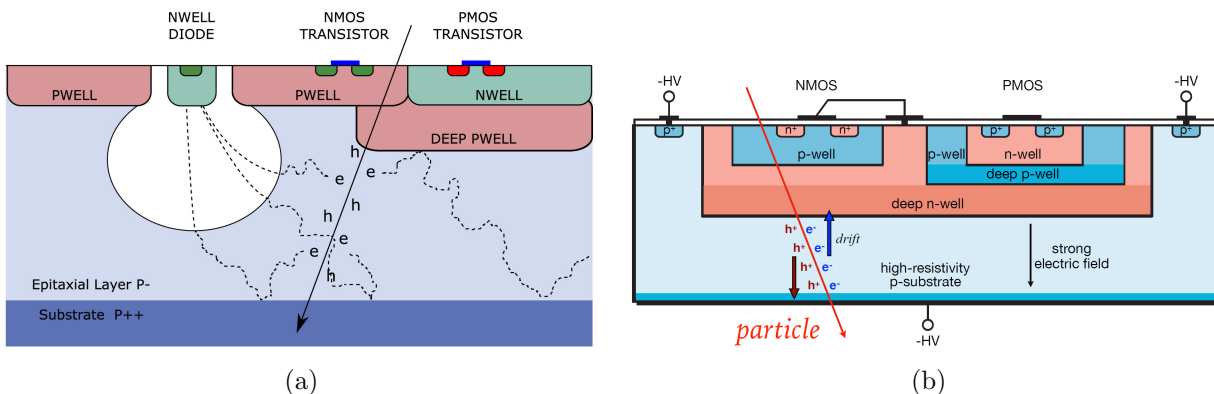


Figure 2.13: Simplified representations are shown of a *HR-CMOS* (a) and a *HV-CMOS* (b) cross-section closely affiliated to the *DMAPS*, integrating photodiodes and readout electronics on a single silicon substrate. The sensor’s active region, formed by a p-n junction between the photodiode and the substrate, facilitates charge generation and separation upon photon or particle interaction. Embedded *HV-CMOS/HV-CMOS* circuitry adjacent to each photodiode enables immediate signal amplification and processing, this shows the compact and efficient design characteristic of *DMAPS* pixel detectors. Images are taken from [79, 80].

***DMAPS* vs. Hybrid:** Again, a contrasting approach from the hybrid is seen in *DMAPS*, where the readout electronics and sensing diodes are integrated into the same substrate (Figure 2.13). This integration offers several advantages over hybrid sensors:

- **Complexity:** Better availability, reduced costs, no interconnection, and faster fabrication due to the use of commercial standard CMOS processes. Also, this results in low input capacitance due to the removal of interconnection, allowing for low-noise front-end designs.
- **Lower Material Budget:** As a result of the lower material budget, reduced multiple Coulomb scattering due to the absence of a two-layer setup with bump bonds.



### Challenges of *DMAPS* Technology

*HV-CMOS/HR-CMOS* technology offers several advantages over traditional sensor designs; however, they face the same challenges and issues that were long overcome in hybrids. This lack stems from the technology's relatively young age in its application within high-energy physics. However, while the *HV-CMOS/HR-CMOS* technology is relatively young, it still profits from the previous understanding and studies made with the hybrids. In essence, many subjects need to be redone; however, the basic understanding of the issues is now more advanced (e.g. at the beginning of the hybrids, it was not known why there was radiation damage, to begin with). The following subjects need to be investigated once more, but this time for the *HV-CMOS/HR-CMOS* technology, specifically:

- **Radiation Hardness:** Increasing radiation hardness is important as *HV-CMOS/HR-CMOS* sensors are expected to withstand high radiation environments typical of modern collider experiments. Strategies include optimizing substrate resistivity and thickness to enhance the depletion region and employing manufacturing processes to mitigate radiation effects. The exact problems for radiation hardness are:
  - **Lattice Damage:** Exposure to high-energy particles can damage the crystal lattice of the silicon sensor. This damage creates defects that act as traps for charge carriers, degrading the detector's performance over time.
  - **Leakage Current:** Radiation-induced damage can increase the leakage current within the sensor, leading to higher noise levels and potentially affecting the detector's signal clarity.
  - **Bias Voltage and Depletion Depth:** To mitigate radiation damage, higher bias voltages are often applied to increase the depletion depth, enhancing the detector's radiation tolerance. However, this approach can lead to other challenges, such as increased power consumption and the risk of breakdown at high voltages.
- **Detector Design:** Balancing out all the parameters within the design is essential to optimize the *DMAPS* while minimizing adverse effects in:
  - **Timing Resolution:** There is a continuous need to improve the timing resolution to track fast-moving particles accurately. This involves enhancing the sensor architecture to speed up charge collection and minimize delays in the readout electronics.
  - **Signal Integrity and Crosstalk:** Integrating readout electronics and sensor elements on the same substrate can introduce crosstalk and signal integrity issues, especially as device complexity and pixel density increase. Isolation techniques (e.g. guard rings) and improved circuit design must be employed to manage these effects.
  - **Scalability and Yield:** As the demand for larger area detectors grows, scaling up *DMAPS* production while maintaining high yields and performance consistency across larger wafers is a challenge. This requires innovations in *CMOS* fabrication processes and quality control measures.
  - **Cost and Complexity of Production:** While *DMAPS* offer a reduction in the material and production costs compared to hybrid designs, the initial setup and tuning of production lines for high-performance *DMAPS* can be complex and costly. Scale and process optimization are crucial to make these technologies economically viable for large-scale employment.

These subjects and processes are far better understood in hybrid designs and need to be investigated again from the ground up. In addressing these challenges, *DMAPS* technology continues to evolve, with ongoing research focused on enhancing radiation hardness and spatial resolution.

**Objectives and Focus of RD50** The CERN RD50 collaboration's primary objective is to pioneer sensor technologies that remain operational within these high-radiation fields. The focus is on innovative structures, notably *HV-CMOS* technologies, which promise enhanced radiation tolerance and operational longevity in harsh environments. The CERN RD50 HV-CMOS group is at the forefront of this endeavour, concentrating efforts on several key areas:

- **ASIC Design:** *ASICs* that leverage HV CMOS technology for optimized performance in high-radiation fields.
- **TCAD Simulations:** Utilizing Technology Computer-Aided Design (TCAD) tools to simulate the physical and electrical behaviours of sensors under various conditions, guiding the development of more resilient devices.
- **DAQ Development:** Engineering Data Acquisition (DAQ) systems that can efficiently process and manage the vast data volumes generated by next-generation detectors.
- **Performance Evaluation:** Conducting comprehensive evaluations of chip performance to validate their efficacy and resilience in radiation-rich environments.

**Impact and Implications** Through its focused research and development activities, the RD50 collaboration aims to enhance semiconductor detectors' capability to operate under extreme conditions with excellent temporal resolution and contribute to the success of future collider experiments. By pushing the boundaries of *HV-CMOS* technology and related semiconductor innovations, RD50 is laying the groundwork for the next generation of radiation-hard detectors.

## 2.4 Timing in Silicon-Based Pixel Detectors

In [section 1.2](#), the utilization of improving the time resolution to allow the temporal tracking of particles was first highlighted. However, in order to correctly measure such parameters, some contributions to the measured time resolution need to be discussed. The time resolution of silicon-based pixel detectors is influenced by factors from both the sensor and the front-end electronics. In pixel *ASICs*, systematic errors in time measurements across the pixel matrix impact performance.

### 2.4.1 Clocking Mechanisms and Time Resolution

Using a global clock involves synchronizing the entire pixel detector array with a single clock source. This approach ensures uniform timing across all pixels, enabling coherent time measurements. However, phase noise and jitter inherent in the global clock signal can propagate throughout the system, affecting the time resolution. The challenge lies in minimizing these effects to preserve temporal accuracy.

An alternative to the global clock is the implementation of on-chip clocks, where individual clocks are embedded within each pixel or pixel group. This decentralization can reduce the impact of phase noise and front-end noise, as each pixel operates independently. Yet, variations in clock rates across the chip due to manufacturing differences or environmental factors introduce complexity in maintaining uniform time measurements across the detector.

For example, in the *Timepix4* architecture, superpixels—a group of  $2 \times 4$  pixels—each has a Voltage-Controlled Oscillator (VCO) connected via a Phase Locked Loop (PLL). This local clock runs at 640 MHz for enhanced timing precision, whereas the general clock operates at only 40 MHz. The decision to use higher frequency clocks locally is also influenced by power consumption considerations. The power consumed by digital electronics is proportional to the clock frequency, and by embedding these clocks within a subset of pixels that activate only upon signal detection, the overall power consumption is significantly reduced compared to continuously operating the entire array at a high frequency.

This approach addresses the inherent trade-off between higher clock speeds for improved timing resolution and increased power consumption. It is worth noting that the power consumption increases with the clock speed, similar to the operating principle in CPUs. Therefore, while technically feasible, increasing the clock frequency to extremely high values like 1 THz would lead to impractical power consumption levels, among other technical challenges.

Another important factor that further influences this parameter is the binning size used in digital signal processing. Binning size, or the granularity with which the time measurements are digitized, directly impacts the achievable time resolution of a detector system. The following subsection explores how binning size affects time resolution.

### 2.4.2 Influence of Binning Size on Time Resolution

The digitization process in pixel *ASICs* involves converting the analogue signal from the front-end electronics into a digital format for subsequent processing and analysis. The binning size determines the smallest time interval that can be resolved by this digitization process, as can be seen in [Figure 2.14](#). A smaller binning size allows for finer time resolution, as it enables the system to distinguish between signal arrivals with minor differences in their time of arrival. However, reducing the binning size increases the demand for data processing and storage systems, as more data points are generated for each event.

The influence of binning size on time resolution can be systematically evaluated by considering the digital sampling theorem and its application to timing measurements in pixel detectors:

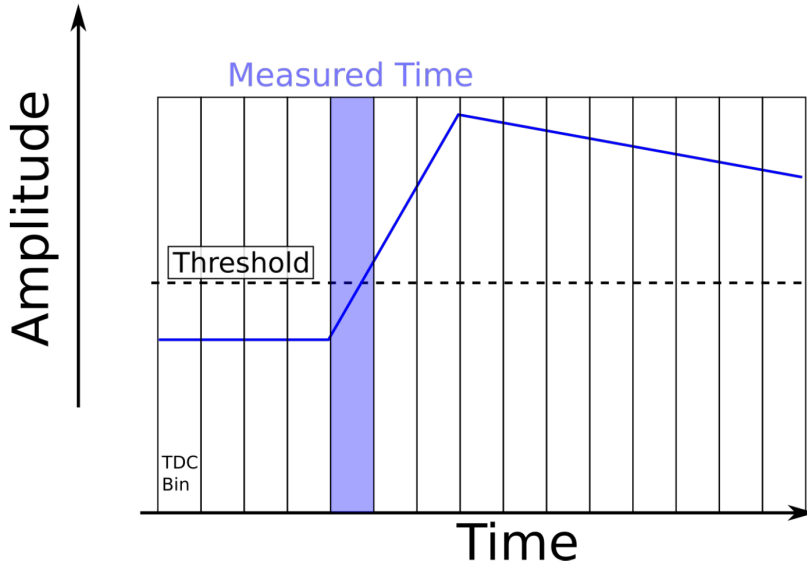


Figure 2.14: Simplified illustration of the influence of binning size on the measured time the amplitude surpasses the threshold and with it the influence on the time resolution (adapted from material provided by Dr. U. Kraemer, personal communication).

$$\sigma_{\text{TDC}} = \frac{\Delta T}{\sqrt{12}} \quad (2.10)$$

where  $\sigma_{\text{TDC}}$  represents the minimum resolvable time difference (i.e., the time resolution), and  $\Delta T$  is defined as the binning size. As the binning size decreases,  $\sigma_{\text{TDC}}$  diminishes, indicating an improvement in time resolution.

The relationship between the clock frequency ( $f$ ) and the binning size is described by the equation  $\Delta T = \frac{1}{f}$ . This direct relation shows that the time-based granularity is linked to the frequency of the clock controlling the sampling process. Hence, higher clock frequencies can facilitate smaller binning sizes, enhancing the time resolution.

However, optimizing the binning size for a pixel detector involves balancing the enhanced time resolution against power consumption and the increased computational and storage requirements. Furthermore, practical limitations such as the speed of the readout electronics, the clock synchronization accuracy across the pixel matrix, and the system's noise characteristics also constrain the lowest attainable binning size.

### 2.4.3 Timewalk in Front-End Electronics

Time walk is an inherent characteristic of analogue front-end electronics used in timing measurements, particularly in systems utilizing leading-edge discrimination. As depicted in Figure 2.15a, preamplifier responses vary with charge levels, influencing the threshold crossing time due to voltage noise at the preamplifier output. Notably, for smaller signals, the preamplifier's response to the current pulse (initially occurring at  $t_0 = 1$  ns) crosses the threshold later than anticipated. This delay, referred to as timewalk, is attributed not only to the delayed response of the preamplifier but also to variations in the discriminator's response time, which depends on the signal's amplitude relative to the threshold.

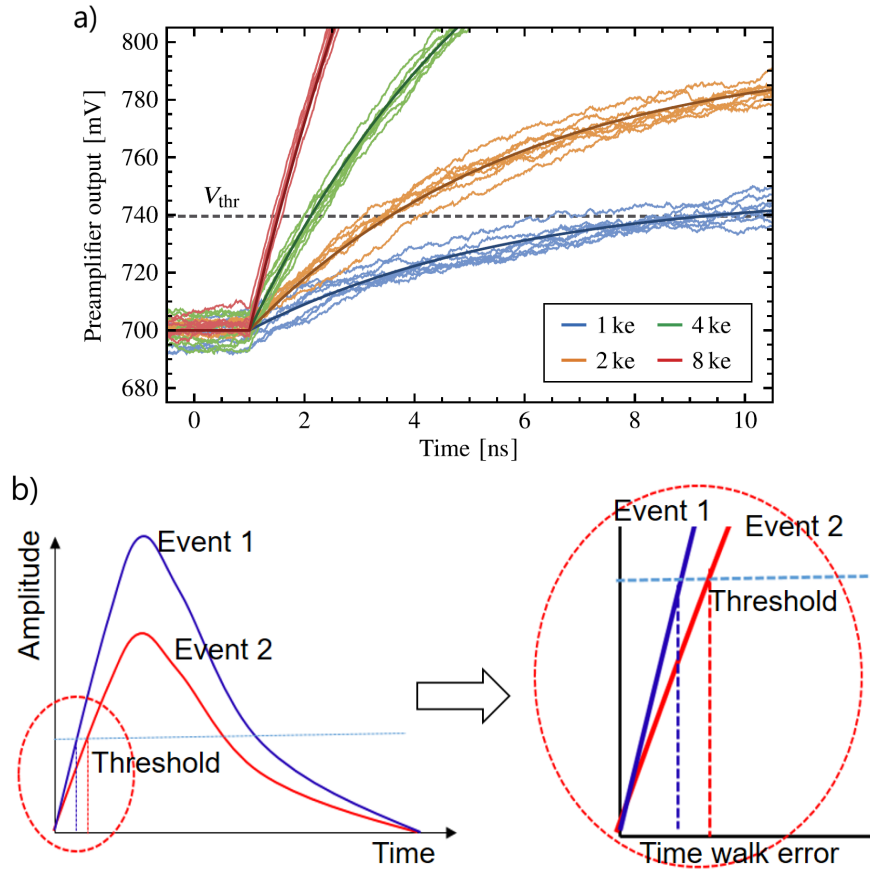


Figure 2.15: **(a)** This figure demonstrates preamplifier response leading edges for varying charge quantities. Each charge level is represented by multiple responses to illustrate the effect of voltage noise. The threshold level is denoted by a dashed line. **(b)** This figure demonstrates the relationship between the faster rise time of the signal and the measured signal surpassing the threshold, giving the *Timewalk* error between two events. Images are taken from [19, 81].

The effect of timewalk can impact the accuracy of time measurements, such as the threshold crossing time in precise timing applications. Systems designed to compensate for timewalk typically utilize calibration techniques to correlate direct measurements of the signal shape to the expected timing errors. These corrections assume that the signal shape remains consistent across different charge values, allowing for effective adjustment of the time measurement discrepancies.

In general, time measurement systems should be designed to consider timewalk effects to ensure that variations in signal amplitude do not adversely affect the timing accuracy. This involves careful design of the front-end electronics and potentially the use of integrated circuits that standardize response times across a range of input conditions.

One approach to mitigate timewalk is Constant Fraction Discrimination (CFD), where the threshold is set as a percentage of the signal height. This allows for more consistent timing, irrespective of signal amplitude. However, *CFD* implementation in pixel detectors is challenging due to the complexity and constraints of pixel electronics.

As an alternative, many pixel detectors employ a static threshold and correct for timewalk in post-analysis by using the measured signal height to adjust the timing data. This correction method compensates for the timewalk by aligning the measured times based on the known relationship

between signal height and timing error; this standardizes the time measurements across varying signal amplitudes.

#### 2.4.4 Jitter in Front-End Electronics

$\sigma_{\text{Jitter}}$  denotes the time uncertainty associated with the comparator's activation timing, influenced by noise within the signal or the detector's electronics. This uncertainty arises from the comparator triggering prematurely or with a delay due to the fluctuating noise levels superimposed on the signal. Mathematically,  $\sigma_{\text{Jitter}}$  is directly proportional to the amplitude of the signal noise ( $\sigma_{\text{Noise}}$ ) and inversely proportional to the rate of change (slope) of the signal at the threshold voltage ( $V_{\text{th}}$ ), expressed as:

$$\sigma_{\text{Jitter}} = \frac{\sigma_{\text{Noise}}}{\left| \frac{dV}{dt} \right|_{V=V_{\text{th}}}} \quad (2.11)$$

where  $\frac{dV}{dt}$  represents the slope of the signal at the threshold crossing point [19]. The  $\sigma_{\text{Jitter}}$  is a combination and convolution of the Front-end noise and the Landau Fluctuations, as discussed in subsection 2.2.2. The implication of jitter on the timing resolution is depicted in Figure 2.16, illustrating how noise can cause the signal to cross the threshold earlier or later than anticipated. This effect directly impacts the precision of time measurements in silicon-based pixel detectors, emphasizing the need to optimize the signal-to-noise ratio and ensure a steep slope at the comparator's threshold level to minimize timing errors.

Figure 2.15 and Figure 2.16 show the need for the rapid, powerful, and concise lasers needed to optimally measure the *Time resolution*. The measured signal must not be dependent on the slow rise time of the signal from the laser or the low input of the laser, as then the chip is not measured for its *Time resolution*, but the laser's *Time resolution* is characterised.

Considering the focus on a single pixel, all the named contributions to the time resolution will culminate into the following relation for the overall time resolution denoted by  $\sigma_t$ :

$$\sigma_t^2 = \sigma_{\text{clock-global}}^2 + \sigma_{\text{clock-on-chip}}^2 + \sigma_{\text{TDC}}^2 + \sigma_{\text{Timewalk}}^2 + \sigma_{\text{Jitter}}^2. \quad (2.12)$$

This equation represents the various contributions for a single pixel readout, focusing on the interplay and relative importance of each component in the overall time resolution calculation.

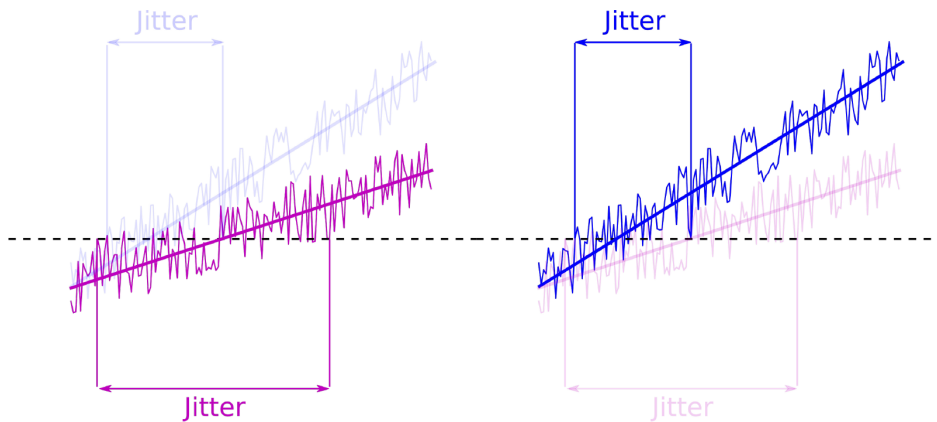


Figure 2.16: Simplified illustration of the influence of the same amount of noise has on two different rising signals, a fast-rising signal is impacted less for its time resolution (adapted from material provided by Dr. U. Kraemer, personal communication).

### 3 Readout Systems for Pixel Detectors

In this thesis, Single Photon Absorption (SPA) laser setups are utilized to investigate the performance of the RD50 Multi-Project Wafer (MPW) silicon detectors. A special focus is spent on the temporal performance of the RD50-MPW, with a direct comparison between two iterations of the detector series in order to evaluate shortcomings and successes of the newest iterations changes.

This chapter consists of four parts: a short discussion of the instrumentation setup in [subsection 3.1](#), a description of the readout electronics of the different boards in [subsection 3.2.3](#), a detailed analysis of the evolution for the used RD50-MPW series chips in [subsection 3.3](#), and finally an analysis of the implication for the used RD50-MPW4 chips in [subsection 3.4](#).

#### 3.1 Setup and Instrumentation

##### 3.1.1 Laser Characterization and Selection

At the Nikhef facility, a comprehensive study of *SPA* lasers is employed for the purpose of conducting time-performance-based measurements. This study comprises:

- A continuous wave (CW) or pulsed operation diode laser operating at a wavelength of 683 nm.
- A continuous wave (CW) or pulsed operation diode laser operating at a wavelength of 976 nm [82, 83].
- A Gain Switching pulsed diode laser operating at a wavelength of 933 nm [84].

The choice of laser wavelength depends upon the sensor’s depth under examination. Sensors with a thickness in the order of 300  $\mu\text{m}$  necessitate a signal capable of deeper penetration into the detector. Conversely, sensors with reduced thickness in the order of 50  $\mu\text{m}$ , a shorter wavelength that ensures rapid absorption upon interaction with the material, are preferable because they carry higher photon energy. Notably, the absorption depth in silicon is defined as the distance a photon can travel before interaction with the material, rising with an increase in wavelength. Lasers with shorter wavelengths are favoured for sensors with a reduced thickness, provided the absorption depth extends into the sensitive sensor region. This is because they carry a higher energy per photon, as described by the equation:

$$E_f = \frac{hc}{\lambda}, \quad (3.1)$$

where the equation depends on Planck’s constant ( $h$ ), the speed of light ( $c$ ), and the wavelength ( $\lambda$ ).

**683 nm** The QFLD-670-2S produced by QPhotonics is a compact system that can generate optical *CW* and pulsed waves operation using diode lasers, also referred to as one of the slow *SPAs*. This device was bought in 2005, and the model was discontinued many years ago. Due to its age, support for the model was discontinued, and additional data provided by the manufacturer is no longer available. This device is designed as a wavelength-stabilized single-mode fibre-coupled laser diode at a central wavelength of 670 nm, and the actual central wavelength was measured at 683 nm ([Appendix B](#)). A wavelength of 683 nm falls within the red portion of the visible light spectrum. The red laser is capable of delivering a maximum laser output of 1 mW at a voltage of 2.47 V directly from the pigtail, achieving a spectral width of 0.95 nm.

**976 nm** The QFBGLD-980-5 produced by QPhotonics is a compact system that can generate optical *CW* and pulsed waves operation using diode lasers, also referred to as one of the slow *SPAs*. This device, designed as a wavelength-stabilized single-mode fibre-coupled laser diode, operates at a wavelength of 976 nm (so near-infrared), delivering an output power ranging from 0 to 5 mW. It employs Fibre-Bragg-Grating (FBG) technology to ensure precise wavelength stabilization, crucial for applications requiring high spectral purity, with a narrow spectral width (FWHM) of 0.02 nm. Operational parameters include an operating voltage of 2.08 V and a current range of 80 mA, with a reverse voltage tolerance between 5 to 20 V. The threshold current is set at 52 mA, which is a low threshold current with high slope efficiency in the generated laser output. It also features a monitoring current of 1.79 mA for feedback control. The QFBGLD-980-5 operates within a temperature range of 25 °C to 70 °C, ensuring reliability under varying environmental conditions. Its temperature drift is modestly rated at 0.01 nm °C<sup>-1</sup>, further attesting to its stable performance over temperature fluctuations. This laser diode is designed to ease integration into existing systems and is provided in a 14-Pin DIL/DIP/Through-Hole format and equipped with an FC connector. Its class 3B laser product classification underlines the careful handling and safety precautions necessary for its operation.

**PIL1-094-40FC** The PIL1-094-40FC (FC for fibre coupled version) produced by NKT Photonics is a compact system generating ultra-short Gain Switching optical pulses using diode lasers, also referred to as the fast *SPA*. This fast *SPA* laser has an emitted wavelength ( $\lambda$ ) of 933 nm (so near-infrared) and a Max. pulse repetition rate (f) of 40 MHz; the very low jitter and different triggering possibilities make the PILAS a flexible and reliable system suitable for a wide range of applications. The Average radiant power at max. rep. rate ( $P_0$ ) is 5000  $\mu$ W, the Peak radiant power ( $P_P$ ) is 3000 mW, and the Pulse duration (t) is 100 ps. This PILAS laser system is classified as a class 3B laser (5 mW, infrared) product. Furthermore, a scan of the official supplied Test and calibration report is displayed in [Appendix C](#). The PILAS system, integral to our experimental setup, comprises a control unit and an optical head that contains the electrical driver and laser diode, as can be seen in [Figure 3.1](#). It operates on gain-switching (see [subsection 3.1.2](#)), a technique that modulates the diode via an electronic circuit to produce electrical pulses of high amplitude. These pulses are characterized by variable widths and minimal jitter, 1.9 ps, allowing for precise temporal resolution.

Tuning within the PILAS system is achieved by modulating the laser diode current, which directly influences pulse amplitude and width. Through the “TUNE” function accessible via the controller’s menu, users can inversely modify the laser diode current, where lower “TUNE” values represent increased diode current, thereby enhancing pulse amplitude. Optimal pulse shapes are attainable by sticking to the system’s test report’s recommended “TUNE” values.



Figure 3.1: The PIL1-094-40FC produced by NKT Photonics. Image is taken from [84]



The PILAS system accommodates both internal and external trigger modes. The system accepts Transistor-Transistor Logic (TTL) signals for external triggering, requiring a minimum voltage of 1.5 V and adjustable amplitude inputs up to  $\pm 10$  V. This external trigger functionality permits the synchronization of laser pulse emissions with an external clock facilitated through the TTL or adjustable input connections. Users can select the preferred triggering edge, rising or falling, and adjust the trigger level for variable inputs. This enhances the system’s utility in precision applications requiring exact timing alignment between laser pulses and external events or signals.

### 3.1.2 Pulse Generation and Modulation

The integration of the slow *SPA* lasers necessitates the interface with a pulse generator. This device is capable of emitting an electrical signal, thereby dictating the intensity of light the laser should emit, the frequency of pulse emission, and the sustained duration of the signal. The fundamental attributes of this input signal are amplitude, frequency, and pulse width. At the same time, it is essential to ensure the laser operates within a specified safe input signal range. Exposing the laser to an abnormally high amplitude and prolonged pulse width can result in its damage, thereby compromising its ability to operate. To determine the appropriate input parameters, datasheets that describe the relationship between laser output power and input amplitude are consulted, as can be seen in [Appendix B](#). Some lasers experienced internal damage by previous users, as will be shown in [subsection 4.1](#). An Agilent 81110A pulse-/pattern generator (165/300 MHz) was employed for this research.

On the other hand, the fast *SPA* laser produced by NKT Photonics utilizes the method of gain switching. In this operation, the integration of the fast *SPA* laser did not necessitate interfacing with a pulse generator, as a trigger signal corresponding to the lasing operation is provided by the system without requiring an external driver. Gain switching generates pulses by rapidly applying high pump power to a laser, initiating emission with a delay as amplified spontaneous emission accumulates energy, resulting in a short pulse. This pulse can be shorter than the pump pulse and the gain medium’s upper-state lifetime, closely resembling the spiking phenomenon where only a single spike is produced with short pump durations. The term ”gain medium’s upper-state lifetime” refers to the period excited electrons in the gain medium stay in a higher energy state before returning to a lower level. This lifetime influences the pulse characteristics in gain-switched lasers, where rapid pump power excitation creates short laser pulses. If the pump duration is shorter than the upper-state lifetime, it leads to population inversion and the subsequent release of energy as a coherent pulse once the pump is ceased. Thus, the upper-state lifetime is used to determine the pulse repetition rate and energy, directly impacting the laser’s efficiency and the quality of pulses for applications like timing measurements.

Pulse build-up time decreases with increased pump energy and can be extended by lengthening the laser resonator, which also lengthens the pulse duration. The pump power may be fully turned off or maintained below the lasing threshold. Gain switching differs from free-running operation, where pulsed outputs without a Q-switch result from gain modulation, but should not be confused with quasi-continuous-wave operation modes.

### 3.1.3 Signal Visualization and Data Acquisition via Oscilloscope

To directly check the pulse generator interface with the laser apparatus, it is a standard protocol to include an oscilloscope in the connection (maybe figure if time PLACEHOLDER). Measurements were used to assess only the analogue performance via direct interfacing with the comparator utilising the oscilloscopes. This approach facilitates the acquisition of pulse amplitude and time stamp

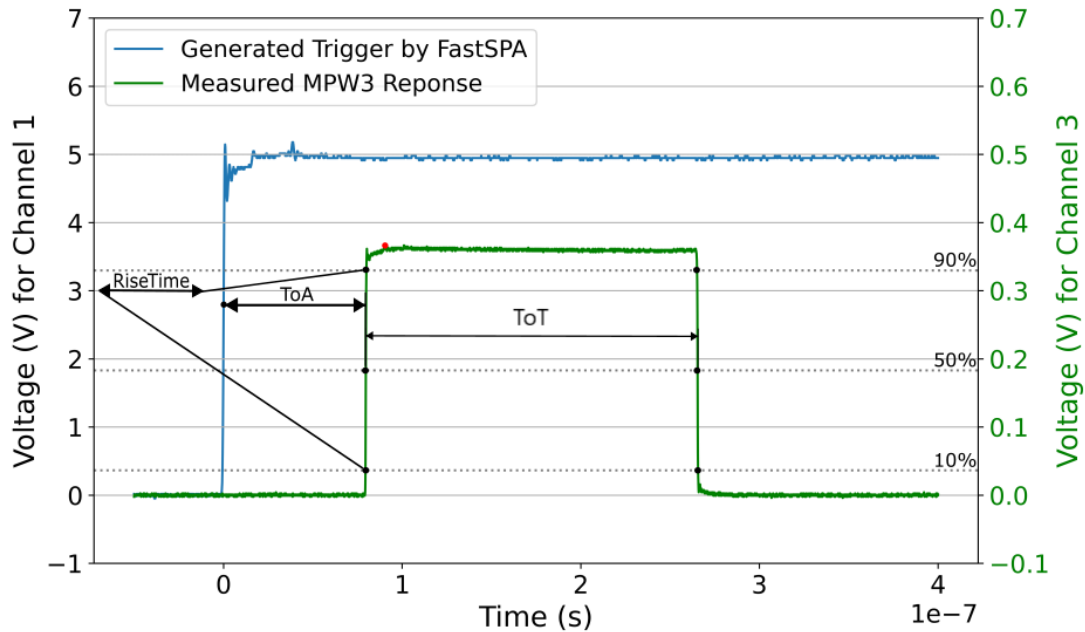


Figure 3.2: Visualization of Time over Threshold (ToT), rise time, and Time of Arrival (ToA) measurements displayed on an oscilloscope. This figure showcases the representation of trigger signals and measured responses, enabling the comparison of incoming and outgoing signals for temporal analysis. Data extracted from channels 3 and 1 are used to calculate key temporal parameters, including pulse amplitude, Time over Threshold, rise time, time of arrival, and time resolution.

data, essential for analysing the signal’s amplitude and temporal characteristics. Additionally, the oscilloscope serves as the point for data extraction, enabling the transfer of data onto external storage such as a computer’s hard drive. The oscilloscope was used to display the generated trigger signal and the measured response in the same frame. Facilitating temporal comparison of the ingoing and outgoing signal.

Figure 3.2 depicts one waveform as received via the oscilloscope. The two graphs are the reference pulse generated by the fastSPA in blue (channel 1) and the response received from the output of the chip in green (channel 3). The pulse amplitude is determined by processing data from channel 3, commencing from the peak amplitude (marked by the red dot) to the falling/trailing edge, and computing the average of this data segment. For channel 1, the procedure is similar, but the average spans from the peak amplitude to the end of the data segment. This computed mean amplitude allows for the determination of the 90%, 50%, and 10% amplitude levels on both the rising/leading and falling/trailing pulse edges. Employing linear interpolation, we pinpoint the precise temporal and voltage positions of these levels, considering they likely fall between two measured points. Important for the evaluation of the system performance are:

- **Time over Threshold (ToT):** Derived by subtracting the interpolated time values at 50% amplitude on the falling/trailing edge from the corresponding time on the rising/leading edge, yielding values typically in the order of several hundred nanoseconds.
- **Rise Time:** Determined by the time difference between the 90% and 10% amplitude points on the rising/leading edge.

- **Time of Arrival (ToA):** Calculated as the time discrepancy between the 50% amplitude points on the rising/leading edges of the reference trigger signal provided by the laser and the signal output from the chip.
- **Time Resolution ( $\sigma_t$ ):** Established from the standard deviation of the  $ToA$  across subsets of 100 measurements, thereby offering a gauge of the detection system's temporal accuracy. For 1000 measurements, this provides 10 distinct Time Resolution data points.

The specific oscilloscope models utilized in this research were the TEKTRONIX 6 Series B (MSO) Mixed Signal Oscilloscope up to 10 GHz 50 GSa/s 12 bits [85], the Agilent Technologies InfiniiVision CSO-X 3054A 500 MHz 4 GSa/s [86], and the Keysight Infiniium MXR604A MSO 6 GHz 16 GSa/s 10 bit [87].

### 3.1.4 Power Supply and Bias Voltage Application

**R&S HMP2020 Two-Channel Power Supply** The Rohde & Schwarz Power Supply is used to power the caribou Board and to supply power to the laser attenuator. Supplying 12.9 V to the caribou board and (typically) 3.4 V to the attenuator (when the laser is at 86% tune and 1 kHz repetition frequency).

**Keithley 2470 High Voltage SourceMeter Source Measure Unit** The Keithley device is used to apply a reverse bias voltage to the pixel sensor. This bias voltage depletes the sensor and subsequently leads to an increased electric field, facilitating the drift of charge carriers. The Source Voltage Range can be changed from 200 mV to 1 kV (at 10 nA to 1000 nA to 1 A). The HV-CMOS was only operated at a maximum of 500 V due to SMA connector only being rated up to 500 V.

**Keysight 33600A Series Trueform Waveform Generators** The 33600A Series waveform generators by Keysight Technologies represent an advancement over traditional Direct Digital Synthesis (DDS) technology. It uses an exclusive digital sampling technique to generate waveforms, providing superior signal generation capabilities [88]. Trueform technology ensures better signal integrity, reduced jitter, lower harmonic distortion, and greater resolution compared to DDS. Featuring a 1 GSa/s sampling rate, up to 120 MHz bandwidth. These devices offer signal integrity with 1 ps jitter and 0.03% total harmonic distortion. The 33600A is used to give injection voltage to the RD50-MPW. These injection voltages can be used to calibrate the response signals.

### 3.1.5 Characterization of the Diodes and Detector

Photodiodes produced by CERN and Thorlabs are used to evaluate the performance of the different laser setups by converting the laser pulse into an electrical pulse. This diode's operational mechanism mirrors that of the pixel sensors. The underlying semiconducting substrate is responsible for the generation of electron-hole pairs in the diode/detector. One of the CERN-produced diodes and the Thorlabs-produced DET08CFC/M Detector is made of Indium Gallium Arsenide (InGaAs), a material renowned for its exceptional photoelectric properties. The other CERN-produced diode has an optical head made of a Silicon PIN.

**Specifications of the CERN-produced Diodes** The CERN-produced Si diode and InGaAs diode have the following specifications due to their material properties and intended applications:

- **Silicon Diode**
  - **Material:** Silicon
  - **Responsivity:** 41.2  $\mu\text{W}/\text{mV}$  at 680 nm
  - **Bandwidth:** 1.5 GHz
  - **Serial Number:** OH-113
- **InGaAs Diode**
  - **Material:** Indium Gallium Arsenide (InGaAs)
  - **Responsivity:** 0.43 A/W at 1060 nm and 0.87 A/W at 1310 nm
  - **Bandwidth:** 1.5 GHz
  - **Serial Number:** 328G219

**Specifications of the DET08CFC/M Detector** The DET08CFC/M detector, designed for high-speed, fibre-coupled applications, is notable for its wide spectral sensitivity range and high bandwidth [89, 90]. Here are the detailed specifications:

- **Wavelength Range:** 800 nm to 1700 nm, catering to a broad spectrum from the near to the far infrared, with a peak wavelength of 1550 nm.
- **Detector Material:** InGaAs.
- **Bandwidth (-3 dB):** 5 GHz, enabling the capture of high-speed signals with minimal delay.
- **Fibre Input:** FC/PC, providing a standardized connection compatible with a wide array of fibre optics.
- **Maximum Peak Power:** 100 mW, indicating the highest power level the detector can handle without saturation.
- **Rise Time:** 70 ps (Typical) at 952 nm, showcasing the detector’s ability to respond quickly to input signal changes.
- **Fall Time:** 110 ps (Typical) at 952 nm, complementing the rapid rise time with a swift return to baseline.
- **Dark Current:** 1.5 nA (Typical), representing the signal noise level in the absence of light input.
- **Noise Equivalent Power (NEP):**  $2 \times 10^{-15} \text{ W}/\sqrt{\text{Hz}}$  at 1550 nm, quantifying the minimum detectable power by the detector.
- **Junction Capacitance:** 0.3 pF, affecting the overall speed and responsiveness of the detector.

These specifications underline the DET08CFC/M detector’s capability to perform in high-speed optical applications.

## 3.2 DAQ

Laboratory experiments are used to assess the performance of the RD50-MPW3 and RD50-MPW4. This necessitated integrating the detector into various data acquisition (DAQ) systems to facilitate comprehensive measurements.

### 3.2.1 Caribou

To facilitate integration with Caribou, a device designated as *RD50-MPW3* was developed for this purpose. This device is programmed to parse a configuration file designed for the MPW3, managing hardware components and configurations established for the *RD50-MPW3*. This setup includes:

- A Field Programmable Gate Array (FPGA) board (Xilinx Zynq ZC706) fully running Yocto-based Linux system (Poky) and the data acquisition software Peary facilitates communication between the control and readout (CaR) board and the RD50-MPW3 chip, as can be seen in [Figure 3.3](#). This board handles the sensor’s dynamic control and data handling.
- The CaR board generates the necessary clock signals and voltage levels for the RD50-MPW3 operation. It’s also designed to support charge injection for calibration and testing purposes.
- A carrier board tailored to the RD50-MPW3, allowing connections to its Hitbus output and setting precise voltages. This board integrates filtering and other essential features for interfacing the chip within the broader DAQ system.

The *RD50-MPW3* device, developed to interact with this hardware assembly, parses a specific RD50-MPW3 configuration file, handling tasks like bias and reference voltage adjustments on the CaR board and configuring the RD50-MPW3 pixel matrix through an  $I^2C$  interface.

In terms of operational capabilities, the system allows for the adjustment of key measurement and control parameters rather than distinct measurement modes. Key functions include:

- **Open-shutter Mode:** A continuous data acquisition mode for recording detector activity over a designated period, useful for experiments with radioactive sources or initial detector evaluations.
- Adjustment functionalities for laboratory measurements and storing the results locally on the *FPGA* board’s SD card:
  - **S-Curve Measurements:** Applies an injection voltage to a pixel for a certain period, logging the hit count. The voltage is incrementally increased from a minimum to a maximum value, generating an ‘S-like’ curve when plotting hit counts against injection voltage.
  - **Enable double column:** Specify which column is specifically enabled for readout.
  - **Set Threshold:** Set the threshold voltage  $V_{th}$  supplied to the chip via external DACs.
  - **Disable External Clock:** It disables the jitter attenuator on the CaR-Board (corrected code was added to PEARY device).

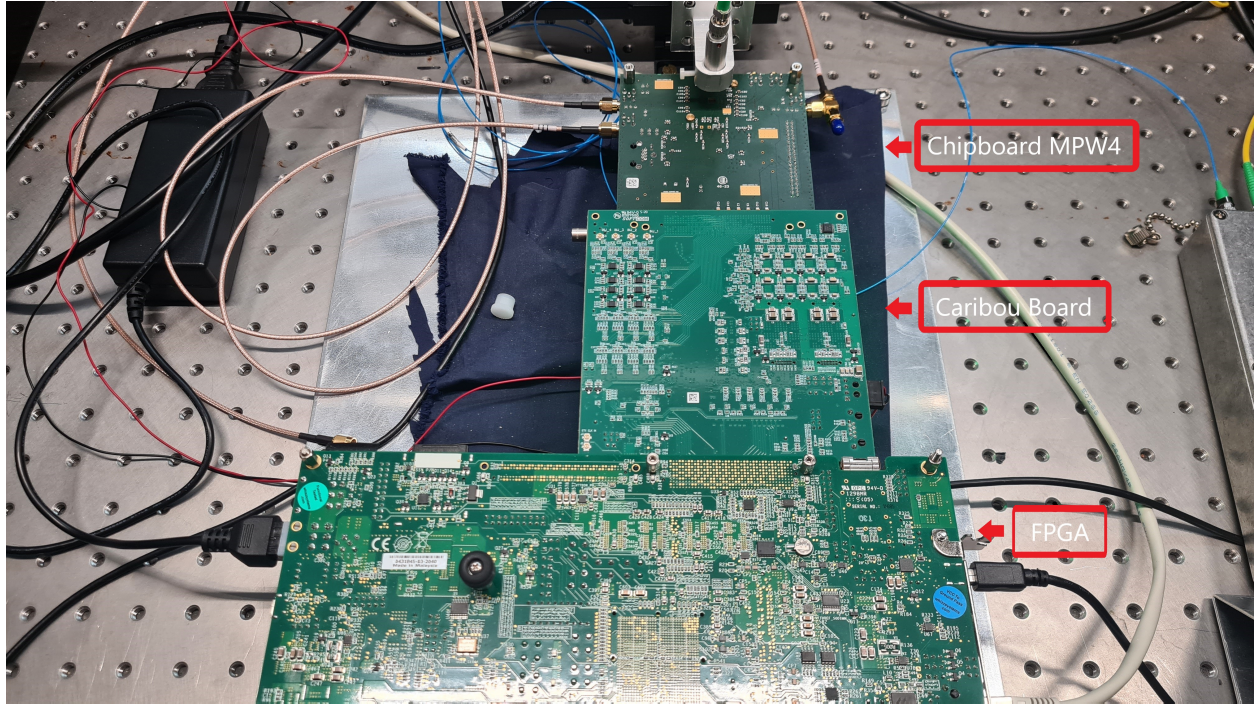


Figure 3.3: Overview of the DAQ Components situated in the setup at the Nikhef facility. The FPGA board, Caribou Board, and the MPW Chipboard.

### 3.2.2 Graphical User Interface

Communication with the RD50-MPW3 and the readout computer was enabled using PEARY software, accessible via the command line interface, a dedicated Graphical User Interface (GUI) for chip control, or automated data acquisition and control through the EUDAQ finite state machine. This GUI supported tasks such as:

- Creating a configuration file for PEARY, specifying bias voltages, pixel configurations, and additional parameters like the detector's  $I^2C$  address and clock settings.
- Directly executing available functions in the PEARY device, circumventing the need for command-line usage.
- Monitoring EUDAQ events in real-time with an embedded monitor feature, facilitating the oversight of data acquisition sessions through EUDAQ.

### 3.2.3 The Readout Electronics

Based on the in-pixel electronics diagram shown in [Figure 3.4](#), a pixel registers a hit if the AC coupled voltage following the preamplifier output,  $V_{\text{preamp}}$ , fulfils the condition:

$$V_{\text{preamp}} + V_{\text{bl}} \geq V_{\text{th}} + V_{\text{tdac}} \quad (3.2)$$

Here, the baseline voltage  $V_{\text{bl}}$  and the threshold voltage  $V_{\text{th}}$  are supplied to the chip via external digital-to-analogue converters (DACs), functioning as global parameters for the entire pixel matrix. Conversely, the Trim-DAC voltage  $V_{\text{tdac}}$  is produced internally and can be individually adjusted

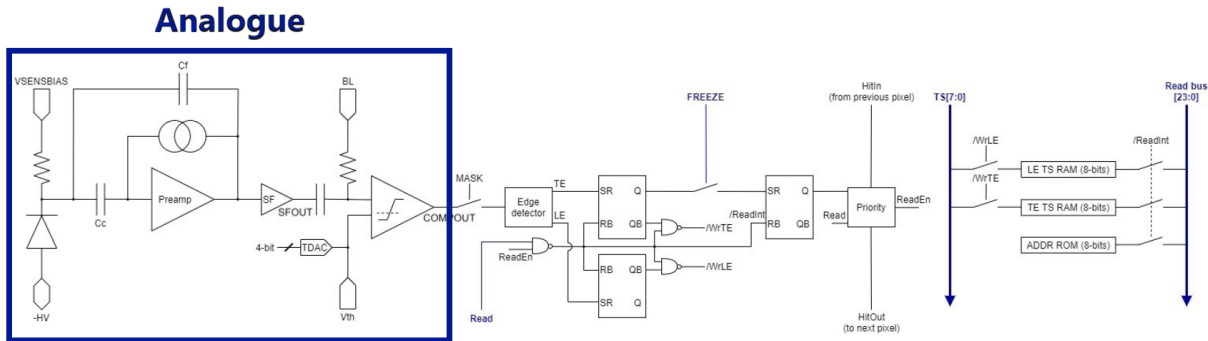


Figure 3.4: Simplified Schematic of the RD50-MPW3 Pixel with Analogue and Digital Readout Electronics. The analogue front-end, inherited from RD50-MPW3 pixels, features a continuous-reset Charge Sensitive Amplifier (CSA). The analogue signal is digitised through an integrated comparator within each pixel. Additionally, a 4-bit trim-DAC allows for fine-tuning the comparator’s threshold, enabling control over the signal processing. An injection circuit is also incorporated into each pixel’s design to facilitate performance characterisation. Moreover, the digital circuits are included, Which are not measured or characterised in the thesis. However, for completeness’ sake, it includes readout control logic, an eight-bit address Read-Only Memory (ROM), and dual eight-bit timestamp Random Access Memories (RAMs). Image is adapted from [91].

for each pixel with a 4-bit value, enabling threshold tuning for every pixel. Additionally, the digital signal output from each pixel can be selectively disabled through masking. This pixel-level configuration enables the deactivation of specific pixels within the matrix; the different settings are displayed in Table 1.

Table 1: Summary of configuration options for individual pixels within the sensor matrix. The boolean registers, when set to “true,” activate their respective functions, encompassing charge injection (EnInj), source-follower output (EnSFout), data output disabling (Mask), and hit-bus output activation (EnHB). The TrimDAC register allows for threshold voltage adjustments through a 4-bit configuration.

Register	Type	Function
EnInj	Boolean	Enable injection
EnSFout	Boolean	Enable source-follower output
TrimDAC	4 bit	Fine adjust $V_{th}$
Mask	Boolean	Disable data output
EnHB	Boolean	Enable hit-bus output

### 3.3 Evolution of the RD50-MPW Series

The RD50-MPW1 chip, submitted in November 2017 and received in April 2018, features dimensions of 5 mm by 5 mm and a thickness of 280  $\mu\text{m}$ . Manufactured on substrates with resistivities of 500  $\Omega\text{cm}$  and 1.9  $\text{k}\Omega\text{cm}$ . As depicted in Figure 3.5, the RD50-MPW1 showcases a pixel cross-section with a large fill-factor. It includes test structures for I-V and Edge-Transient Current Technique (E-TCT) alongside two discrete CMOS pixel arrays. The first array, dedicated to photon counting, comprises 28 by 52 pixels integrating readout electronics, a charge amplifier, a 16-bit counter, and a discriminator. The second array, consisting of 40 by 78 pixels, each measuring 50  $\mu\text{m}$  by 50  $\mu\text{m}$ , incorporates both analogue and digital readout electronics that have a column drain architecture analogous to that of the FEI3 readout chip. The analogue electronics included a Charge Sensitive Amplifier (CSA), low-pass and high-pass filters, and a CMOS comparator. At the same time, the digital readout was based on a column drain architecture, facilitating two 8-bit time stamps and an 8-bit address for event registration [91, 92]. The characterization of RD50-MPW1 involved evaluating leakage current and breakdown voltage within the test structure pixels. A specialized Data Acquisition System (DAQ) was developed for the characterization of the active CMOS pixel matrices. While the sensors were operational, the observed leakage current exceeded initial expectations, and instances of crosstalk were detected among some digital readout lines in the matrix employing the column drain readout scheme.

The development of the RD50-MPW2 sought to minimise leakage current and explore various analogue structures by reducing to a simpler design. This strategy was adopted to facilitate a clearer analysis of how different components impact the overall performance of the chip. Consequently, the MPW2 was equipped with numerous test structures and a variety of pixel designs to enable a comprehensive study of these effects.

The RD50-MPW2 was submitted for fabrication in January 2019, and this device was subsequently received in February 2020. Initially, the prototype dimensions were reduced in RD50-MPW2 to facilitate an evaluation of individual components and firmware/software integration. This downsizing allowed for analysing and optimising the system's architecture and operational efficien-

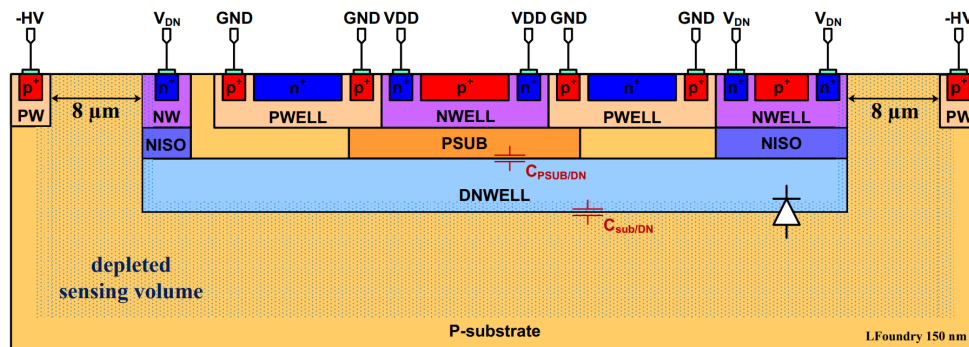


Figure 3.5: Simplified illustration of the *HV-CMOS* cross-section structure of the RD50-MPW series. *HV-CMOS* is designed for high-voltage operation, enabling deep depletion across the sensor substrate. By applying a reverse bias at higher voltages, an extensive electric field extends the depletion zone throughout the bulk silicon, ensuring efficient charge collection over a larger volume. The sensor integrates high-voltage tolerant readout electronics within the substrate, facilitating rapid signal processing and enhanced detection capabilities for high-energy particles. Image is taken from [93].



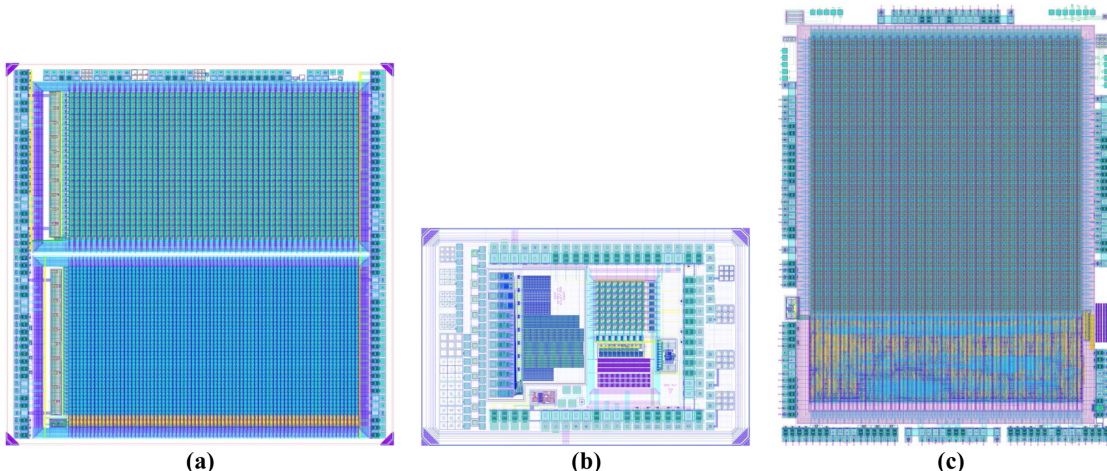


Figure 3.6: The layout views of the RD50-MPW series, RD50-MPW1 (a), RD50-MPW2 (b), and RD50-MPW3 (c), the dimensions of these sensor chips are  $5\text{ mm} \times 5\text{ mm}$ ,  $3.2\text{ mm} \times 2.1\text{ mm}$ , and  $5.1\text{ mm} \times 6.6\text{ mm}$ , respectively. Image is taken from [91].

cies. The design was subsequently expanded after successfully validating these elemental aspects, leading to the comprehensive and advanced RD50-MPW3 model. This is shown in Figure 3.6, showcasing the evolution in design and functionality aspect of the RD50-MPW series development trajectory. Minimising leakage current was achieved by removing specific filling layers added during the foundry process and including a series of guard rings [94]. The RD50-MPW2 demonstrated a reduction in leakage current to approximately  $100\text{ pA}$  per pixel, a substantial decrease from the  $1\text{ }\mu\text{A}$  per pixel observed in RD50-MPW1. It also featured a breakdown voltage of  $120\text{ V}$  and an Equivalent Noise Charge (ENC) below  $2\text{ mV}$  [5, 95].

The device's layout, as illustrated in Figure 3.6, includes I-V and  $E\text{-}TCT$  test structures alongside an 8 by 8 pixel matrix of  $60\text{ }\mu\text{m}$  by  $60\text{ }\mu\text{m}$  pixels equipped with analogue embedded readout electronics. It also features a bandgap voltage reference and an array resilient to Single-Event Upsets (SEU). Assessments indicated a reduction in pixel leakage current by approximately six orders of magnitude to the order of  $100\text{ pA}$ , a contrast to the RD50-MPW1's  $100\text{ }\mu\text{A}$  leakage current. This sensor's enhanced performance and sensitivity could potentially be used for precise particle tracking in future iterations. Additionally, in the pixel readout electronics, an improved speed of data acquisition was achieved [96, 97]. The RD50-MPW2, characterised by its compact size of approximately  $3\text{ mm} \times 2\text{ mm}$  and a uniform thickness of  $280\text{ }\mu\text{m}$ , was fabricated with an array of substrate resistivities, including  $10\text{ }\Omega\text{ cm}$ ,  $0.5\text{ k}\Omega\text{ cm}$  to  $1.1\text{ k}\Omega\text{ cm}$ ,  $1.9\text{ k}\Omega\text{ cm}$ , and ranges between  $2\text{ k}\Omega\text{ cm}$  and  $3\text{ k}\Omega\text{ cm}$ .

Despite the advances made with RD50-MPW2, certain limitations emerged, particularly regarding the pixel matrix's scalability and the simplicity of its peripheral readout circuitry. These constraints highlighted the need for a subsequent iteration to overcome these challenges and introduce advancements in pixel matrix design and readout electronics. Thus, the development of RD50-MPW3 was initiated.

### 3.3.1 Introduction of the RD50-MPW3

The RD50-MPW3, developed under the responsibility of the CERN-RD50 collaboration, focuses on exploring and enhancing aspects of monolithic High-Voltage CMOS (HV-CMOS) sensor technology for high-energy physics applications. This initiative is particularly aimed at meeting the future de-

mands of hadron colliders in terms of radiation tolerance, time resolution, and granularity [5]. By assessing and seeking to refine these key parameters, the RD50-MPW3 contributes to the ongoing evolution and diversification of HV-CMOS sensor technologies in the field, aligning with the broader objective of advancing detector capabilities for next-generation particle physics experiments. Building on the foundational work of its predecessors, RD50-MPW1 (2018) and RD50-MPW2 (2020), the RD50-MPW3 (2022) chip incorporates both analogue and digital readout electronics within a  $64 \times 64$  pixel matrix, aiming for enhanced performance metrics such as high breakdown voltage, low leakage current, and rapid analogue front-end processing as will be discussed in subsection 3.3.2. The RD50-MPW3 is fabricated by LFoundry S.r.l., utilizing a 150 nm *HV-CMOS* process, aiming to achieve elevated spatial resolution alongside robust radiation tolerance [91].

The RD50-MPW3 has adopted a double-column architecture paired with FE-I3 style in-pixel digital readout circuits. This configuration not only enables efficient chip configuration and swift data transmission but also allows for the handling of a larger pixel matrix. The inclusion of an advanced digital periphery complements these improvements, facilitating effective chip management and data handling, as will be discussed in the next subsection.

### 3.3.2 RD50-MPW3; Digital Infrastructure and In-pixel Signal Processing

As was mentioned in the previous subsection, the MPW3 chip tried to address and surpass the constraints identified in its predecessor, RD50-MPW2. It does so by expanding the pixel matrix to include 64 rows and 64 columns and integrating digital readout electronics based on the column drain architecture directly within the pixel area [27]. The pixel pitch of the RD50-MPW3 is specified at  $62 \mu\text{m}$ , from which the spatial resolution is derived to be approximately  $17.9 \mu\text{m}$  [98]. This iteration of the RD50 series also introduces dedicated test structures, primarily for assessing diode I-V features, parasitic capacitance, and depletion depth. Manufactured in three distinct substrate resistivities, MPW3 is produced in the standard resistivity of  $10 \Omega\text{cm}$  and two higher resistivities of  $3 \text{ k}\Omega\text{cm}$  and  $1.9 \text{ k}\Omega\text{cm}$ .

One of the improvements in MPW3 is the in-pixel digital readout electronics, which enhance the device's functionality over when it was designed for RD50-MPW1. This system includes logic to mask noisy pixels, replaces the prior priority circuit for a more space-efficient alternative based on an OR chain, and permits the temporary pausing of new hit digitisation until the column readout concludes. Analogue and digital components within each pixel are segregated into separate deep p-wells, reducing crosstalk noise and optimizing the sensor's operational efficiency. The analogue front-end, a continuation of the RD50-MPW2 design, includes a continuous-reset charge-sensitive amplifier (CSA) proven to offer high processing speed. Complementing this, the in-pixel digital readout employs an 8-bit time-stamp mechanism for recording the  $ToA$  and  $ToT$ , which is important for accurate particle detection and temporal analysis. The pixels are equipped each with an 8-bit SRAM shift register for serial configuration. The register stores critical data, including threshold voltage compensation, noisy pixel masking, and controls for the calibration circuit, amplifier output monitor, and comparator output monitor.

Additionally, MPW3 incorporates a digital periphery running at 40 MHz driven by a single 640 MHz clock and, with that, a digital high-speed readout at up to 640 MHz [98]. Experimental evaluations revealed that an insufficiently rapid discharge of the timestamp signal line (TS-signal-line) within the chip led to abnormal behaviour of the timestamp-leading edge (TS-LE) and timestamp-trailing edge (TS-TE) values. This anomaly was corrected by reducing the operational frequency to 320 MHz, which afforded the TS-signal-line adequate time for discharging, thereby restoring expected dynamics to the TS-LE and TS-TE values in the data readout [71]. Concurrently, this frequency reduction resulted in the adjustment of the digital periphery's clock, set

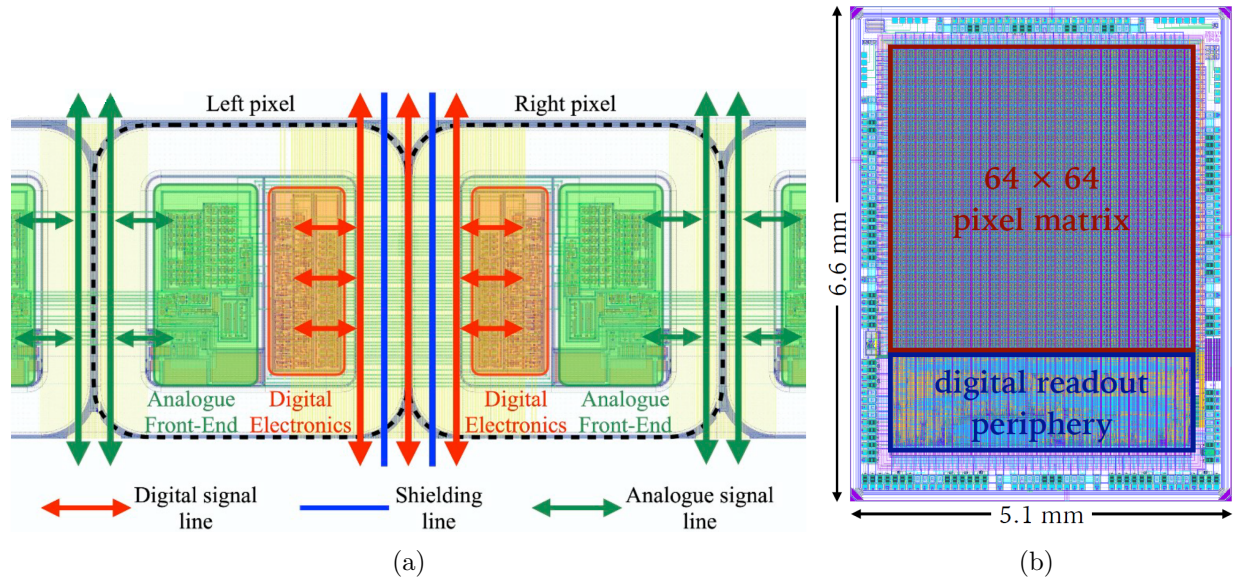


Figure 3.7: It shows how the 64 columns are organised into 32 double columns on the pixel matrix. (a) Illustrates how both the analogue and digital electronics are included inside each pixel. Their orientation is mirrored to each other to prevent signal induction from the analogue and digital lines. To save area and avoid crosstalk between digital and analogue signals, Digital signal lines are placed in the middle of each double column; analogue lines are placed between double columns; Shielding lines (grounded) are inserted between digital signal lines to minimise coupling. Image is taken from [5]. (b) Illustrates the location and proximity of the digital readout periphery to the pixel matrix. Image is taken from [71].

initially at 40 MHz, down to 20 MHz.

MPW3 introduces a double-column architecture in the pixel matrix to circumvent routing congestion. This scheme and the 8-bit SRAM shift register effectively reduce routing congestion and minimise cross-talk noise. By sharing metal routing lines within double columns, the need for numerous lines is halved, with a mirrored layout in each double column to accommodate this design. The ground-connected metal lines are placed to avoid cross-talk noise. Moreover, the analogue and digital grounds are separated by a trench made of shallow n-well and deep n-isolation to prevent noise interference.

The pixel matrix features four independent power domains and two ground domains to ensure noise-free operation and maintain the integrity of signal processing across various sub-circuits. Additionally, the peripheral electronics of MPW3 are redesigned, featuring Enhanced Output Circuits (EOCs), a Control Unit (CU), and a slow control system employing the  $I^2C$  protocol for external communication through an internal Wishbone bus. This system optimises pixel configuration and control, improving the data readout process with triggerless operation and high-speed serial data transmission capabilities at a maximum rate of 640 Mb/s.

The introduction of the RD50-MPW3 marks a step forward in the evolution of monolithic *HV-CMOS* sensors for particle physics research. This monolithic approach offers advantages, including reduced material thickness, elimination of bump bonding (thus allowing for smaller pixel sizes and reduced production costs), and the application of high-bias voltages for swift charge collection and enhanced radiation tolerance. With its advanced features and design optimizations, the

RD50-MPW3 chip stands as a demonstration of the ongoing innovation within the CERN-RD50 collaboration, aimed at meeting the demands of future collider experiments. As the collaboration continues to evaluate the performance of the latest prototype, the RD50-MPW4, the RD50-MPW4 is expected to offer better performance in almost every aspect compared to the RD50-MPW3.

### 3.4 Description of the RD50-MPW4

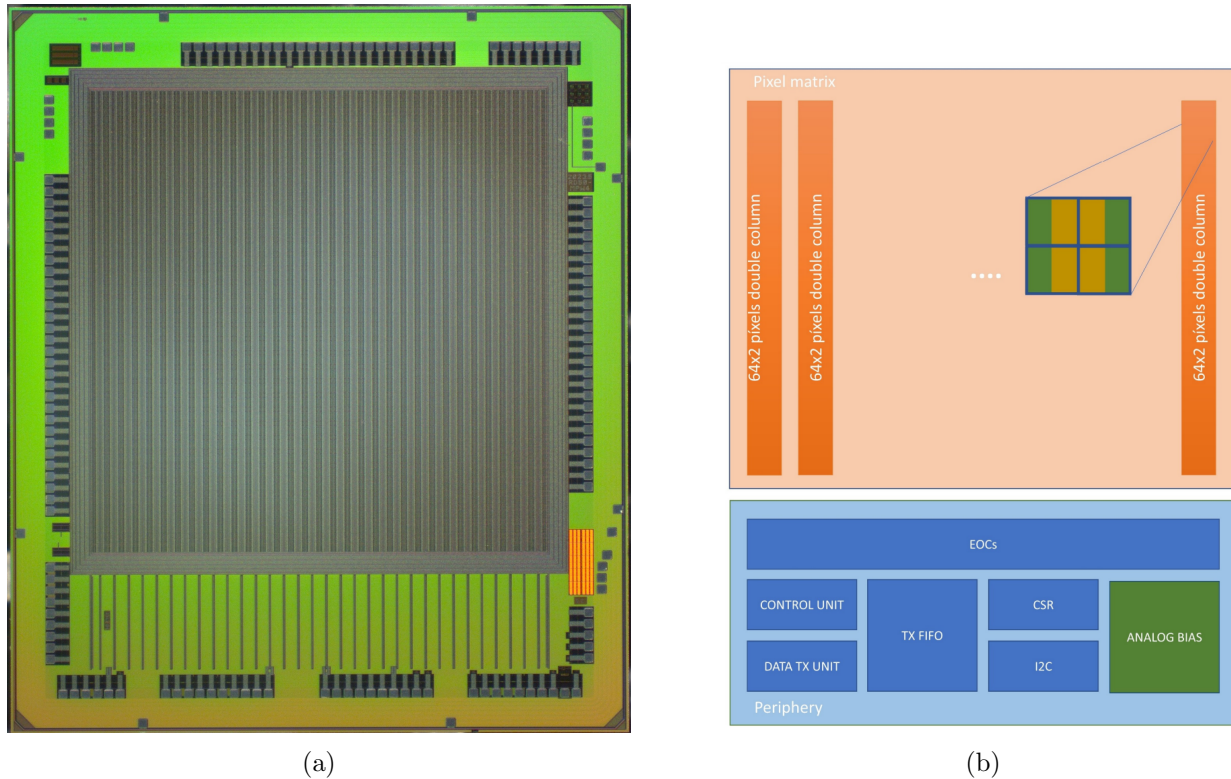


Figure 3.8: **(a)** Depicts the RD50-MPW4 showcased within the facilities at Nikhef. This image captures the chip shortly after its arrival. **(b)** Illustrates the block diagram of the RD50-MPW4 chip (identical to the RD50-MPW3). The orange area represents the  $64 \times 64$  pixel matrix and the blue area is the digital readout periphery. Image is taken from [99].

The RD50-MPW4 was developed by the CERN-RD50 collaboration as a continuation of the RD50-MPW3. The RD50-MPW4 is fabricated using the 150 nm High-Voltage CMOS (HV-CMOS) process from LFoundry and was submitted for fabrication in May 2023 and received in January 2024. The design incorporates different substrate resistivities: a standard  $10 \Omega \text{ cm}$  (1 wafer) and  $3 \text{ k}\Omega \text{ cm}$  (3 wafers). The chip dimensions are 5.36 mm by 6.30 mm. The RD50-MPW4 is shown when it just arrived at the Nikhef facilities as depicted in [Figure 3.8](#).

#### 3.4.1 Design Methodology and Innovations:

RD50-MPW4 inherits almost all core architecture of the RD50-MPW3, including the  $64 \times 64$  pixel matrix with identical layout and almost identical dimensions. The RD50-MPW4 is slightly smaller ( $5.36 \text{ mm} \times 6.30 \text{ mm}$ ) as the dimensions of the digital periphery have been reduced. However, it introduces a suite of refinements based on the insights gained from its predecessor. These

improvements are aimed at enhancing overall chip efficiency, radiation tolerance, and reducing power consumption, thereby optimizing the chip for future high-energy physics. Most details of the key enhancements are displayed in Table 2 and some will be further elaborated down below; for the full description, however, see the referred literature [99].

### 3.4.2 Key Enhancements:

- **Power Domain Separation:** An improvement in the RD50-MPW4 is the separation of power domains between the pixel matrix and the digital readout circuitry. This separation is achieved through the implementation of dedicated power lines and isolation techniques to minimize power coupling and substrate noise between the analogue and digital sections of the chip. By segregating the power supplies, the RD50-MPW4 reduces the noise injection from the digital circuits into the sensitive analogue front-end, leading to improved signal integrity and lower threshold voltages for particle detection.
- **Digital Periphery and FIFO Redesign:** The RD50-MPW4's digital periphery underwent a redesign, focusing on the reduction of the FIFO (First-In, First-Out) memory blocks used for data buffering and processing. This optimization not only leads to a decrease in the digital area footprint but also contributes to a reduction in power consumption. The streamlined digital periphery enhances the efficiency of data readout and processing, ensuring faster and more reliable data transmission even under the high data rate conditions expected in future experiments.
- **Guard Ring Optimization:** The RD50-MPW4 introduces a guard ring structure designed to enhance the chip's high voltage tolerance, and with that, the radiation tolerance can be better compensated. This introduction involves redesigning the peripheral guard rings to improve leakage current containment and reduce surface current paths that could potentially degrade the sensor's performance under high-radiation conditions. The new guard ring configuration is optimized based on simulations to ensure improved high-voltage stability and maximal effectiveness in shielding the active pixel area from edge-related leakage currents, thereby extending the operational lifetime of the sensor in high-radiation environments.
- **Backside Biasing:** Introducing backside biasing in the RD50-MPW4 offers a versatile approach to applying high voltage across the sensor. Backside biasing enhances the uniformity of the electric field distribution within the sensor. This uniformity is crucial for preventing localized regions where the electric field might intensify to levels that could initiate breakdown, characterized by an uncontrolled increase in carrier multiplication. The application of biasing from the chip's backside leverages a broad, consistent surface area to apply the potential, in contrast to localized biasing points within each pixel. This approach draws a parallel to the electrostatic principle where a larger surface area, such as a sphere, can sustain higher voltages without discharging, unlike a smaller, pointed surface like a needle, which could lead to electrical arcing under the same conditions. Hence, backside biasing not only contributes to a more stable operation at higher voltages by mitigating the risk of electric field-induced breakdown but also improves the sensor's resilience to radiation.
- **Clock Issue:** The clock issue in the MPW series stemmed from parasitic capacitances in the circuit layout, which slowed down signal transitions at high clock frequencies. This effect is governed by the RC time constant, where a high product of resistance and capacitance leads to longer charging and discharging times, delaying signal switching. The initial resolution in RD50-MPW3 involved reducing the clock frequency from 640 MHz to 320 MHz, effectively

doubling the clock period to 50 ns. This reduction was necessary to accommodate the time required for signals to transition states, given the parasitic capacitance effects. Consequently, the baseline clock frequency that governed the internal operations also shifted from 40 MHz to 20 MHz. In the RD50-MPW4, rather than simply reducing parasitic capacitances, the design introduced flexibility in readout timing. Rather than strictly requiring a line to be pulled to zero within a single cycle, the redesign permitted multiple cycles for a signal on the timestamp line to be read out. This adjustment not only directly addressed the issue of parasitic capacitance but also restored higher clock frequencies, thereby enhancing the efficiency of the readout process. Furthermore, the layout and SRAM driver strength were enhanced, this redesign allowed for faster signal transitions, enabling a return to higher clock frequencies. This adjustment improved the readout process's efficiency.

Table 2: Main design details and performance parameters of the RD50-MPW pixel chips (adapted from material provided by Dr. J. Sonneveld, personal communication).

Parameter	RD50-MPW1	RD50-MPW2	RD50-MPW3	RD50-MPW4
Device size [mm × mm]	5 × 5	3.2 × 2.1	5.1 × 6.6	5.4 × 6.3
Pixel matrix size	40 × 78	8 × 8	64 × 64	64 × 64
Pixel size [μm × μm]	50 × 50	60 × 60	62 × 62	62 × 62
P-n spacing [μm]	3	8	8	8
In-pixel electronics	Analogue Digital	Analogue	Analogue Digital	Analogue Digital
Output data	Pixel address Time-stamp	Binary	Pixel address Time-stamp	Pixel address Time-stamp
Digital periphery	78 EOCs 2 LVDs lines	8 EOCs	32 EOCs, with 32-events 24-bit FIFOs 128-events 32-bit TX FIFOs I2C Wishbone bus 1 LVDs line	32 EOCs, with 16-events 24-bit FIFOs 64-events 32-bit TX FIFOs I2C Wishbone bus 1 LVDs line
Chip guard ring frame	None	1 n-ring 6 p-rings	1n-ring 6p-rings	1 n-ring 5n-/p-rings
Substrate biasing	Through p-stop contacts	Through p-stop contacts	Through p-stop contacts	Through chip edge or backside
Substrate resistivity [kΩ · cm]	0.5 – 1.1 1.9	Standard: 0 0.2 – 0.5 1.9 3	Standard: 0 1.9 3	Standard: 0 3
Device thickness [μm]	280	280	280	280
V <sub>BD</sub> [V]	56	120	120	600
ILEAK [μA/ pixel]	1	10 <sup>-4</sup>	10 <sup>-6</sup>	10 <sup>-6</sup>
Depletion depth [μm]	118	190 [100]	190	Fully depleted
ENC [mV]	50	2	< 140, > 50	50
Efficiency [%]	Not tested	Not tested	60	> 99

## 4 Results

The experimental examination measured different types of lasers, diodes, and chipboards. In this section, the data will be presented and discussed. The goal was to observe and compare the unique properties of the different lasers and analyse the difference between the new and older iterations of the RD50-MPW chipboard.

### 4.1 Laser and Diode

In this subsection, an analysis is performed that considers the characterization of the lasers. This was essential before proceeding to the RD50-MPW-series measurements. The lasers needed to be tested for performance to determine whether they met the high standards for measuring the RD50-MPW series. If a laser's rise time is too slow, the rise time measurements of the RD50-MPW-series are essentially not a measure of the RD50-MPW-series' responsiveness but of the laser's rise time.

Note that terminology is different between the diode measurements and the MPW measurements. In the diode detector measurements, instead of referring to the width of the measured signal as Time over Threshold (ToT), it is named by convention as Pulse Width, as seen in [Figure 4.5a](#). Furthermore, all the plots with the error bars are derived from taking the standard deviation of the related measurement data.

#### 4.1.1 683 nm, QFLD-670-2S

Previous examinations at Nikhef frequently employed a specific red laser (683 nm) for their experiments. However, concerns were raised regarding its conformance to high standards. Subsequent measurements highlighted a deficiency in the laser's performance (using the Si Cern-produced Diode), specifically its rise time. Furthermore, the waveforms of the slow *SPA* sustained too much noise on top of the waveform to accurately extract the parameters from, resulting in the utilization of a moving average smoothing function being projected over the data as can be seen in [Figure 4.1a](#).

The observed rise time was considerably slower than optimal, reaching the maximum and desired value only when subjected to an input pulse width of approximately 5  $\mu\text{s}$  (at a Voltage high of 2.6 V, see [Figure 4.1b](#)), while the leading edge on the pulse generator was set to 2 ns. For precise measurements of time resolution in detectors, particularly in the context of the MPW series, the laser's rise time is especially important. Ideally, the rise time should be as low as possible to avoid contributing to the measured time resolution, as discussed in [section 2.4](#).

Given these considerations, it became clear that the use of this slow *SPA* laser would not meet the requirements necessary for accurately measuring the time resolution of the MPW series detectors. This necessitated the transition to a fast *SPA* laser, capable of delivering the required rise time performance for high-precision time resolution measurements. All affiliated measurements of this slow *SPA* can be found in [Appendix D.1](#) for further elaboration and investigation.

#### 4.1.2 976 nm, QFBGLD-980-5

In previous investigations at Nikhef, a particular near-infrared laser with a wavelength of 976 nm was frequently utilized. Although the InGaAs diode's responsivity at the specific operational wavelength remains undefined, it was recorded to be 0.43 A/W at 1060 nm. However, the value for this responsivity was found to be 3.73 A/W at 980 nm by the referred literature [101]. Concerns were raised regarding its conformance to high standards as it was suspected that the laser might have sustained damage from improper usage, particularly due to the application of a negative bias voltage. Measurements resulting from this investigation can be found in [Appendix D.2](#).

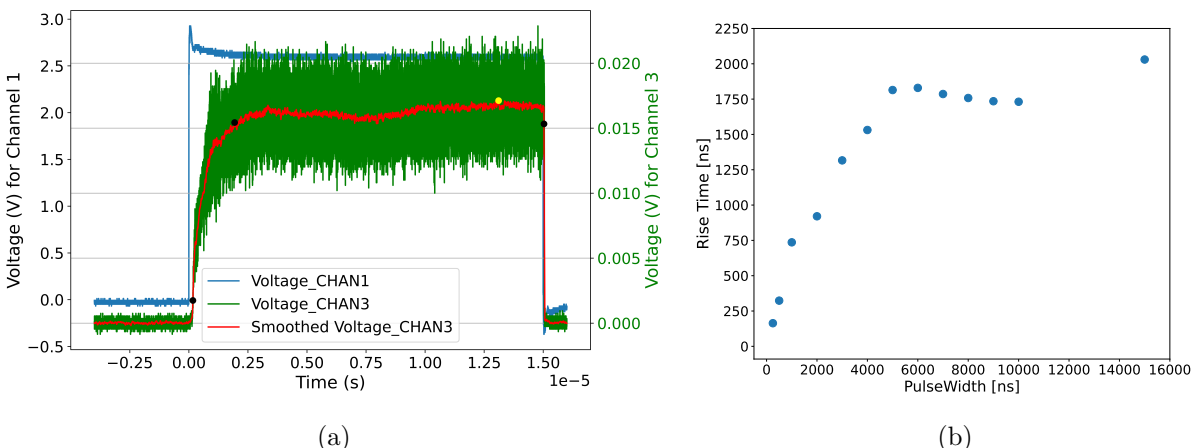


Figure 4.1: Left image (a): Illustration of the utilization of the moving average smoothing function for the measured response of the diode being illuminated by the red laser. The two black dots on the left represent the 10 % and 90 % points of the measurements, so the difference in amplitude is the rise time here. Right image (b): Showing the rise time measurement of 1000/2000 averaged measurement points per data point of the 683 nm QFLD-670-2S laser as a function of the pulse width. The plot captures the laser’s performance, illustrating the prolonged rise time that reaches its maximum at an input pulse width of approximately 5  $\mu$ s and a voltage of 2.6 V.

The stability and rise time characteristics of the waveform emitted by this near-infrared laser were superior to that of the other slow *SPA* laser, inciting an investigation of its suitability for the precise measurements required in the RD50-MPW series investigations. Optimal performance was anticipated at higher pumping voltages, which are known to yield shorter rise times and a signal less prone to jitter influences, thereby enhancing time resolution. However, increasing the applied voltage to 3 V induced undesirable effects within the waveform, including an additional step in the rise time and the emergence of oscillations atop the pulse width, as can be seen in Figure 4.2a. These artifacts would be devastating for a precise time resolution measurement; the response signal was more stable at a high voltage of 2.7 V.

Further scrutiny appeared when the response signal at 2.7 V was investigated. Notably, the amplitude measurements and the RMS of the pulse width amplitude manifested an oscillation artifact (Figure 4.2b and Figure 4.4), and the pulse width demonstrated a tendency towards two distinct equilibrium states Figure 4.3). These aberrations pointed out the inadequacy of this slow *SPA* laser for the precise demands of time resolution assessment within the RD50-MPW-series detectors. Consequently, a transition towards the fast *SPA* laser is needed, capable of delivering the required rise time performance for high-precision time resolution measurements.



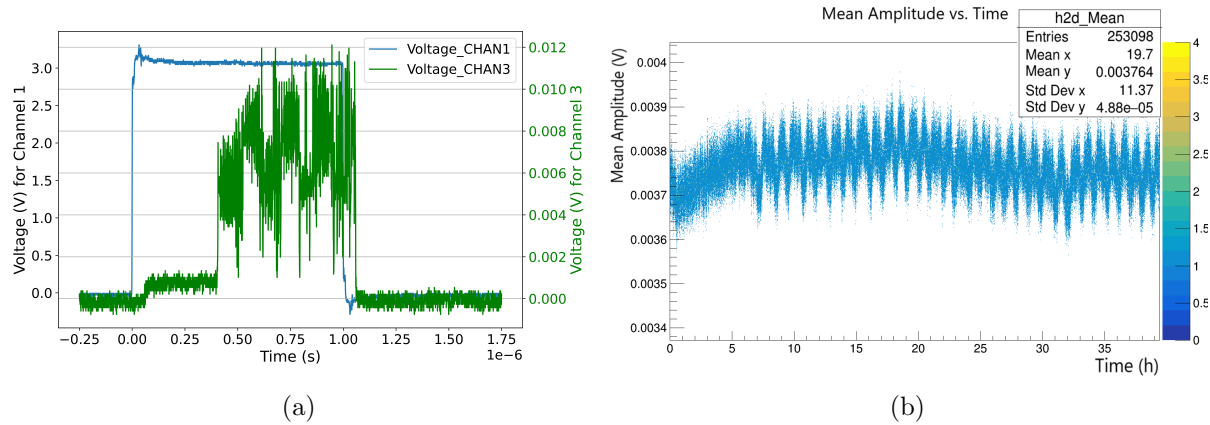


Figure 4.2: Both results are of the 976 nm slowSPA at  $1 \mu\text{s}$  applied pulse width. Here, (a) is the waveform of the laser when the high voltage was put to 3 V, and (b) is the amplitude measurement over a longer period of time, where the manifested oscillation artifact is visible.

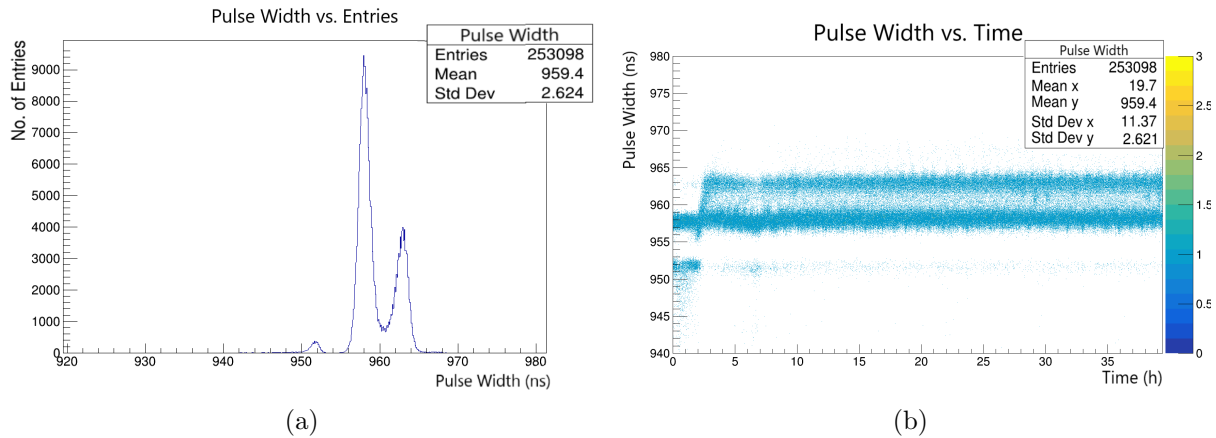


Figure 4.3: Both pulse width results are of the 976 nm slowSPA at  $1 \mu\text{s}$  applied pulse width and 2.7 V high voltage over a longer period of time, where the manifested oscillation artifact is visible.

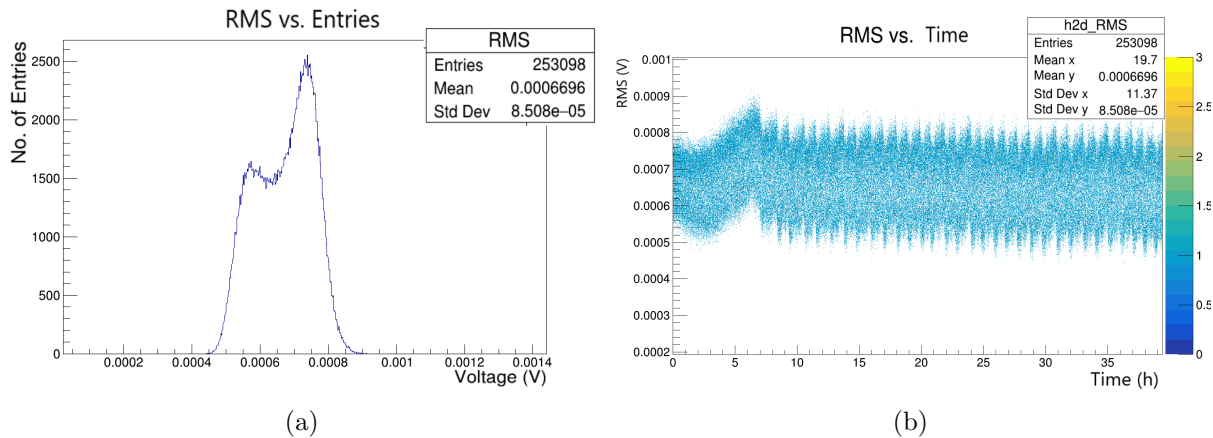


Figure 4.4: Both RMS of the amplitude heights are of the 976 nm slowSPA at  $1 \mu\text{s}$  applied pulse width and 2.7 V high voltage over a longer period of time, where the manifested oscillation artifact is visible.

### 4.1.3 933 nm, PIL1-094-40FC

The 933 nm PIL1-094-40FC is a very rapid and concise near-infrared laser; its fast rise times and short pulse widths are visible in a measurement waveform where the PILAS was measured with the DET08CFC/M detector in Figure 4.5a. For further details about the fastSPA or the detector, look at subsection 3.1 and subsection 3.1.5. The PILAS system was tested to determine whether it was capable of measuring the RD50-MPW series correctly.

The PILAS system showed a satisfactory time resolution, as can be seen in Figure D.12, a mean time resolution of 12.7 ps was measured. A few tens of picoseconds were also the goal to be measured, showing that the PILAS laser system is accurate enough in order to determine time resolution for the measurements of the RD50-MPW series. It became clear that the fastSPA had significant dependence on temperature shifts; the measurements indicated that the fastSPA system requires considerable warm-up time to achieve a stable operational state, as can be seen in Figure 4.5b. Another significant irregularity is visible: the  $ToA$  seemed to be significantly increasing and decreasing over a daytime period. After several discussions, the temperature measurements of the room were compared, and an apparent temperature dependence became visible, as can be seen in Figure 4.6. The origin of these temperature fluctuations is unknown; however, some of the building’s heating or power cycles could be the problem.

The temperature effects led to fluctuations in the time resolution by about 40 ps. While these fluctuations are relatively minor compared to the overall time resolution of the system, they underscore the importance of maintaining a controlled measurement environment. These slow temperature changes have minimal impact on measurements within our typical operational timeframe, primarily because procedures to mitigate warm-up effects were implemented. Should long-duration measurements become necessary, the observed temperature dependency should be addressed, pos-

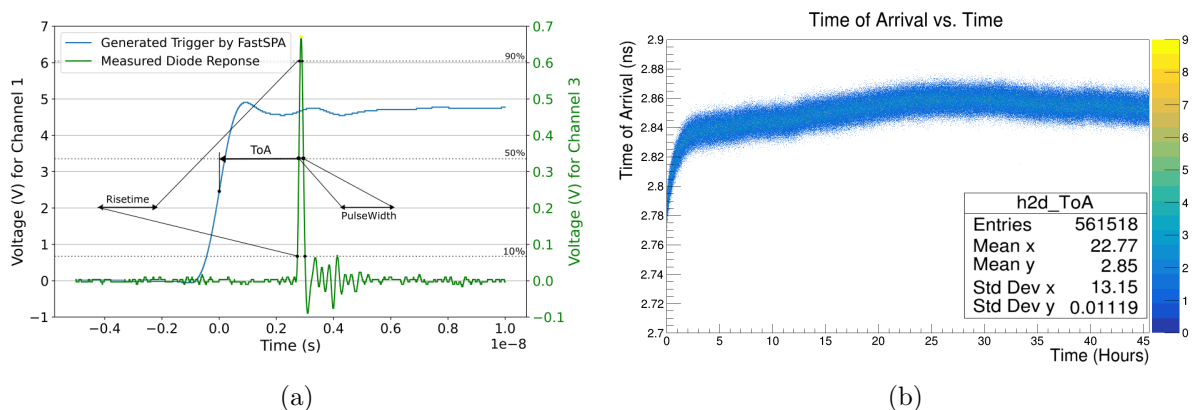


Figure 4.5: Left image (a): A visualization of the Pulse Width, rise time, and  $ToA$  measurements captured via an oscilloscope. This figure showcases the representation of trigger signals and measured responses, enabling the comparison of incoming and outgoing signals for temporal analysis. Data extracted from channels 1 and 3 are used to calculate key temporal parameters (channel 2 was not accessible due to the cabling coming from channels 1 and 3), including pulse amplitude, Pulse Width, rise time, time of arrival, and time resolution. Right image (b): Shows one of the preliminary measurements when the laser was not warmed up before usage, showing the effect of the heating up of the laser in the first hours of the measurement. Further fluctuations are due to fluctuations in the room temperature. In this image, the  $ToA$  is shown as a function of time over roughly two days time.

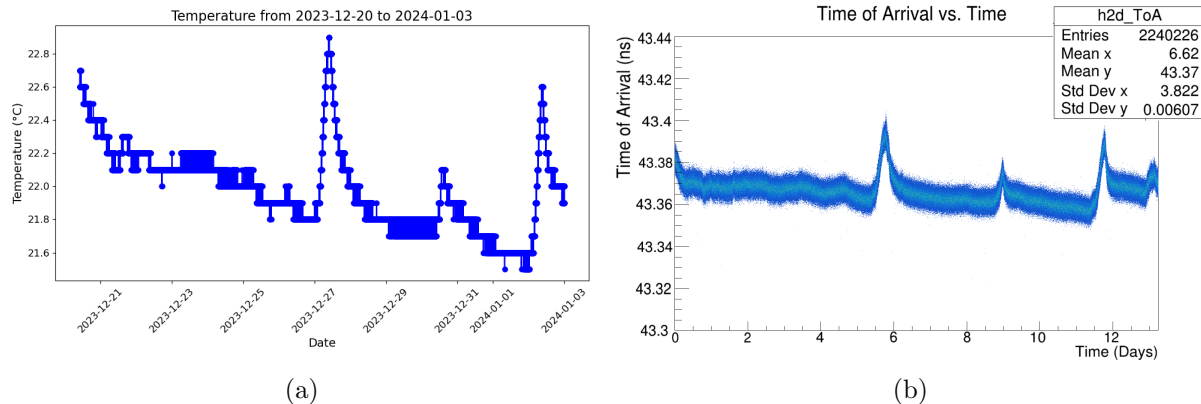


Figure 4.6: Temperature Influence on fastSPA Performance: A comparative analysis of room temperature fluctuations and  $ToA$  fluctuation for the PIL1-094-40FC laser. The left panel (a) illustrates the correlation between ambient temperature changes and the operational stability of the fastSPA laser over the Christmas break, highlighting the laser’s sensitivity to environmental conditions. It can be seen that the temperature graph in the tail is just a bit shorter than the right graph; this originates from the temperature measurement crashing prematurely. The right panel (b) shows the impact on the  $ToA$  measurements, highlighting the need for temperature control in maintaining precise time resolution over long periods of time.

sibly through enhanced climate control measures to ensure consistency and higher accuracy measurements of the time resolution. The other long-time measurements of the PILAS system can be seen in [Appendix D.3](#).

## 4.2 RD50-MPW3

The RD50-MPW3 represents the third iteration of *HV-CMOS* based monolithic chip technology developed by the CERN-RD50 CMOS collaboration. In previous sections, the observations about the RD50-MPW3 have raised concerns about its performance. One of the main concerns was the influence of the external clock within the digital readout periphery on the waveform extracted from the RD50-MPW3. For this reason, this section looks into the clock on and clock off situation and its effects, all affiliated measurements can be found in [Appendix D.4](#). First, however, the charge injection and  $ToT$  calibration are performed in order to put these findings in perspective relative to expected charge depositions at real-life experiments.

Note that the terminology used to describe diode measurements differs from that applied to the RD50-MPW measurements. Specifically, within the RD50-MPW assessments, the width of the measured signal is by convention referred to as Time over Threshold ( $ToT$ ), as illustrated in [Figure 3.2](#).

### 4.2.1 Charge Injection and $ToT$ Calibration

In the characterization of the RD50-MPW3, charge injection techniques are used to calibrate and study the sensors’ response to various charge levels. Injecting charge simulates the effect of a real particle hitting the pixel matrix without the actual particle interaction. This method is particularly useful for systematic testing and calibrating pixel sensors.

The  $ToT$  measurement and electron count correlation were done for the RD50-MPW3. The measurements using injection voltages for the single pixel were done over the range from 450 mV

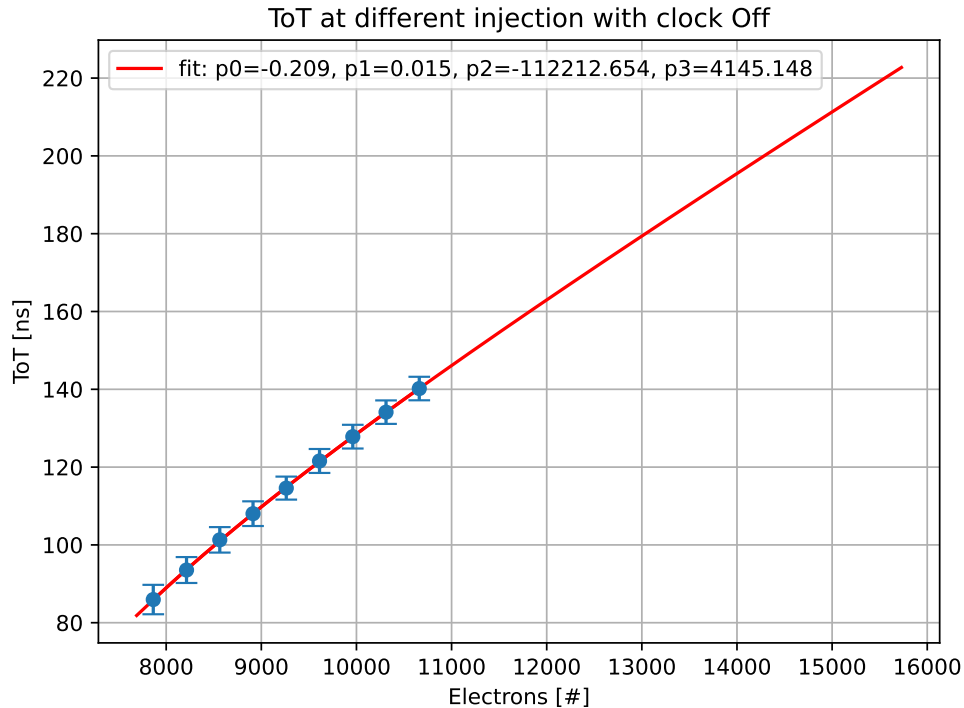


Figure 4.7: Graph depicting the correlation between injected charge (in electrons) and measured  $ToT$  for the MPW3. Where the fit function is:  $f(x, p_0, p_1, p_2, p_3) = p_0 + p_1x - \frac{p_2}{p_3 - x}$ .

to 610 mV in steps of 20 mV.  $ToT$  was calibrated using the equation  $Q = C \cdot V$ , where  $C = 2.8$  fF is the capacitance of the pixel’s frontend electronics, and  $V$  is the injection voltage.

Through this method, the  $ToT$  of 169 ns (Figure D.13a), with the clock activated, corresponds to an electron count of approximately 12200 electrons as can be seen from Figure 4.11. Furthermore, the  $ToT$  of 180 ns (Figure D.13b), with the clock deactivated, corresponds to an electron count of approximately 13000 electrons as can be seen from Figure 4.11. It is assumed that all the measurement results of the MPW3 are made at the same parameters measured and such behave the same and use it for all. This quantification allows for tuning of the sensor’s response to expected charge levels from particle interactions.

In the context of the interaction of particles with sensor materials, a *MIP* typically deposits about 80 electrons per micrometre as it traverses silicon. Considering this rate, for a silicon thickness of 190  $\mu\text{m}$ , a *MIP* would deposit approximately 15,200 electrons. This expectation serves as a point of reference for evaluating the sensor’s calibration. The measured  $ToT$ s, corresponding to 12200/13000 electrons for the injected voltages, indicates that the measurements taken here were below an expected *MIP* deposition. Therefore, these results are slightly below the worst case (a *MIP*); therefore, the final results are expected to be slightly better.

#### 4.2.2 External Clock Effects

The examination of the digital readout periphery’s external clock influence on the output waveform was conducted following the identification of an overlaying noise artifact upon the waveform’s output. An analysis of a singular waveform frame revealed that this induced noise corresponded with a signal frequency of 20 MHz (Figure 4.8), suggesting a direct correlation with the clock.

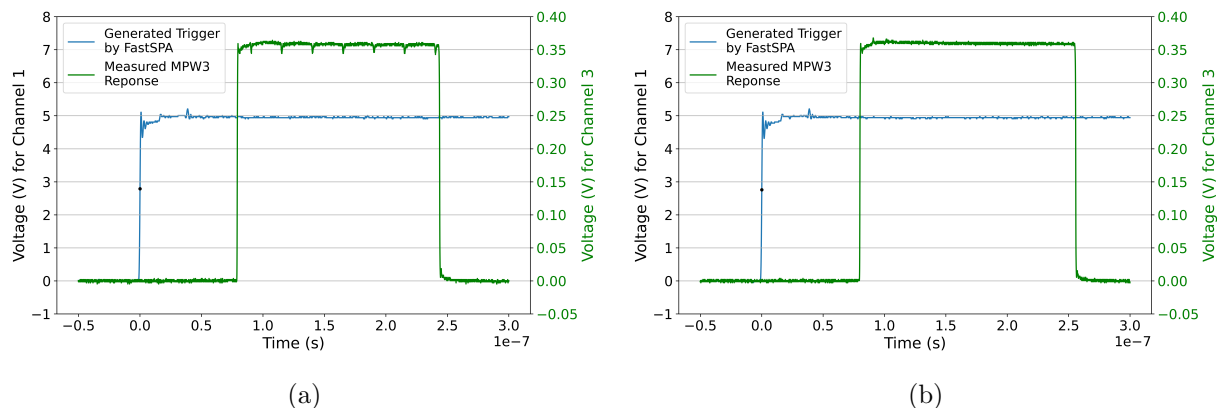


Figure 4.8: Both plots depict a single waveform of the MPW3 long-time measurements where the clock influence is visible, (a) does so for the clock-on situation and (b) for the clock-off situation.

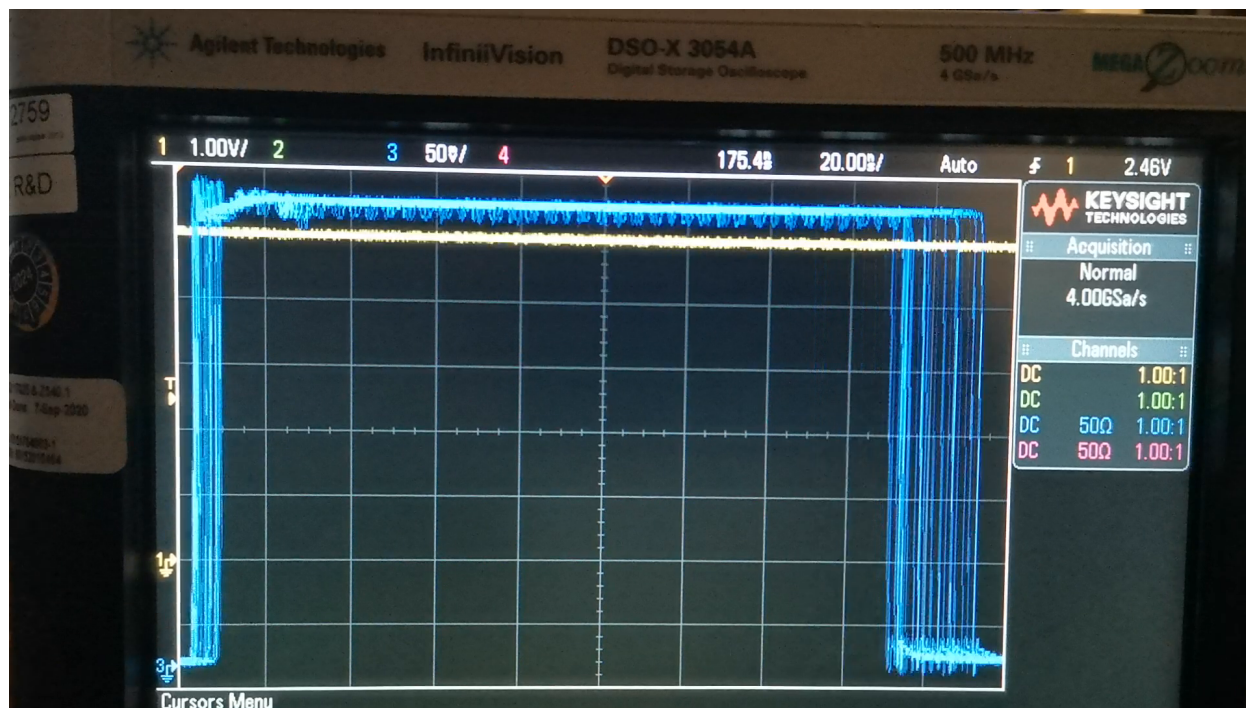


Figure 4.9: This animation depicts the stark waveform noise difference between the clock on and clock off. Note: The animation will only be visible to PDF viewers supporting JavaScript for PDFs, such as Adobe Acrobat Reader. It might not work in all PDF viewers, especially in web browsers or some mobile apps. When you left-click the image, it will freeze for that specific frame.

Further investigation into the noise artifact performed once with an active clock and once with an inactive clock was made, as demonstrated in Figure 4.9. The assessment showed that the time resolution in the absence of the clock noise ( $\sigma_t = 0.293$  ns at a charge of 13000 electrons) surpasses that observed with the clock engaged ( $\sigma_t = 2.01$  ns at a charge of 12200 electrons), showing an order of magnitude improvement (Figure 4.10). This underlines the impact of the external clock on waveform quality and the necessity of optimizing the shielding of analogue from digital signals and vice versa to enhance sensor performance.

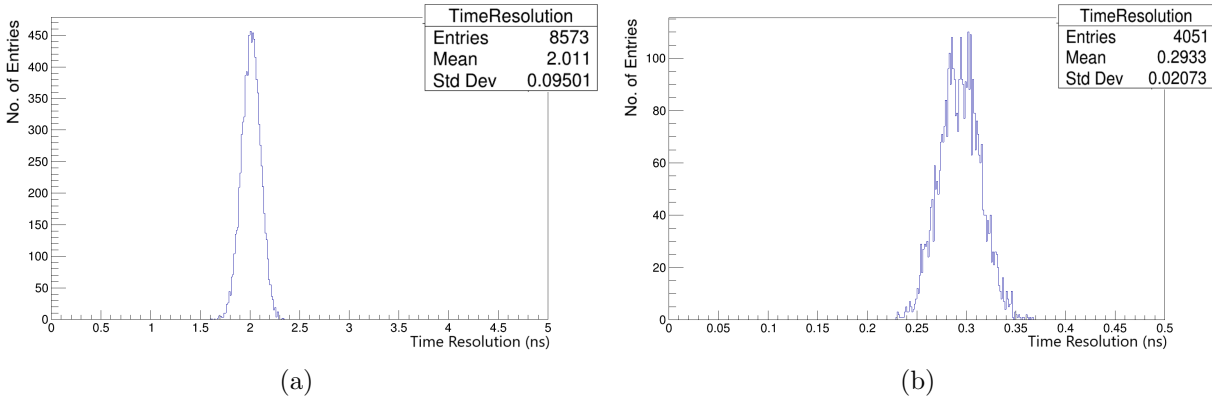


Figure 4.10: Both plots depict the time resolution distribution of the long-time measurements (a) does so for the clock-on situation and (b) for the clock-off situation.

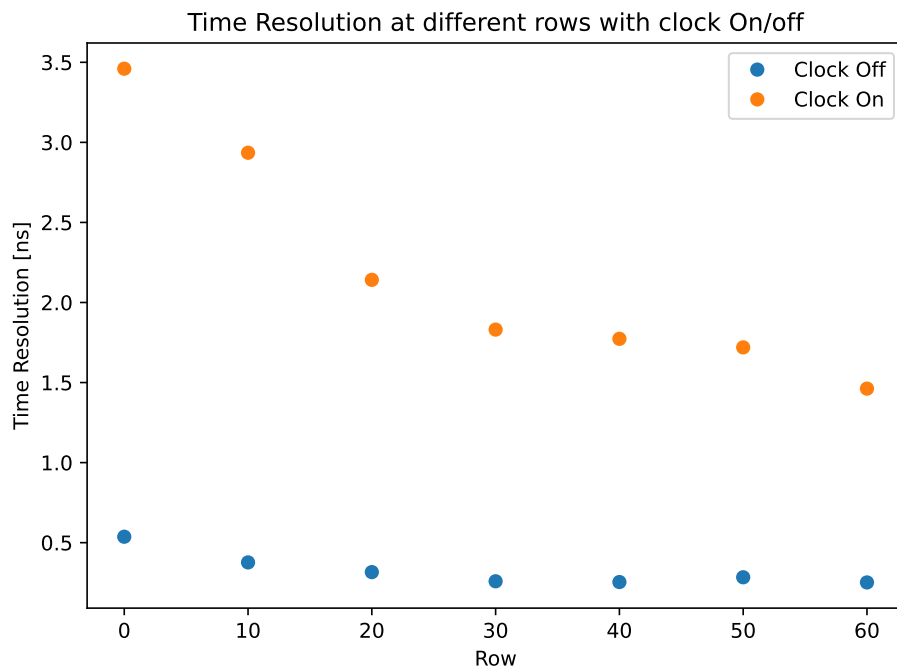


Figure 4.11: This figure illustrates the variation in time resolution across seven rows within a column of the RD50-MPW3 pixel matrix, comparing conditions of clock activation (Clock On) and deactivation (Clock Off). The analysis underscores a degradation in temporal resolution with closer proximity to the digital readout periphery, particularly when the clock signal is active. The visible trend highlights the influence of electromagnetic interference from the clock signal on temporal resolution accuracy.

The earlier findings initiated an investigation into the spatial impact of clock signal proximity on the temporal resolution of active pixels within the RD50-MPW3 pixel matrix. This inquiry focused on an analysis across seven distinct rows within the same column, examining the temporal resolution at varying distances from the digital readout periphery. As shown in [Figure 4.11](#), the analysis spans from row zero, proximate to the digital readout periphery, to row sixty, positioned at

the almost maximal feasible distance. The data unveil a discrepancy in temporal resolution between clock activation and deactivation states across all evaluated rows. Notably, the temporal resolution in the presence of the clock signal is consistently an order of magnitude inferior to that observed in its absence. Beyond the consistent induced offset by the clock’s activation state, an incremental degradation in temporal resolution is observed as pixel proximity to the digital readout periphery increases. This degradation is exacerbated in the clock-on state, manifested by a more negative gradient in temporal resolution approaching row zero, suggesting a scaling negative influence of clock signal proximity on temporal accuracy.

The presence of clock-induced noise is a critical operational issue; while disabling the clock mitigates noise, it renders the chip non-functional for standard operations such as reconfiguration, communication, or digital data output. Essentially, the detector cannot operate in its low-noise state during normal functioning modes. This limitation necessitates a solution that addresses the noise without compromising the detector’s functionality. The ongoing challenge is to design a clock system that minimizes noise while maintaining the chip’s operational capabilities.

### 4.2.3 Pixel Response Through S-Curve Characterization

S-curves are used to analyse the performance characteristics of pixel detectors by quantifying their response to varying signal intensities. The transition from no hits to all hits typically exhibits an S-shaped curve. The width of this curve corresponds to the noise present within the system. Hence, these tests are termed as *S-Curves*. An S-shaped response curve is generated by adjusting either the injection value or the threshold level of a pixel while monitoring the hit registration rate. The 50% point on this curve indicates where the pixel detects the signal half of the time, thus defining the pixel’s effective sensitivity threshold. It’s a balance point indicating where the pixel starts to transition from primarily non-responsive to mostly responsive, providing a quantitative measure of the pixel’s operational characteristics under the tested conditions. Therefore, this midpoint can be used to optimise the detector’s sensitivity and noise characteristics, permitting precise calibration of threshold settings to achieve optimal performance.

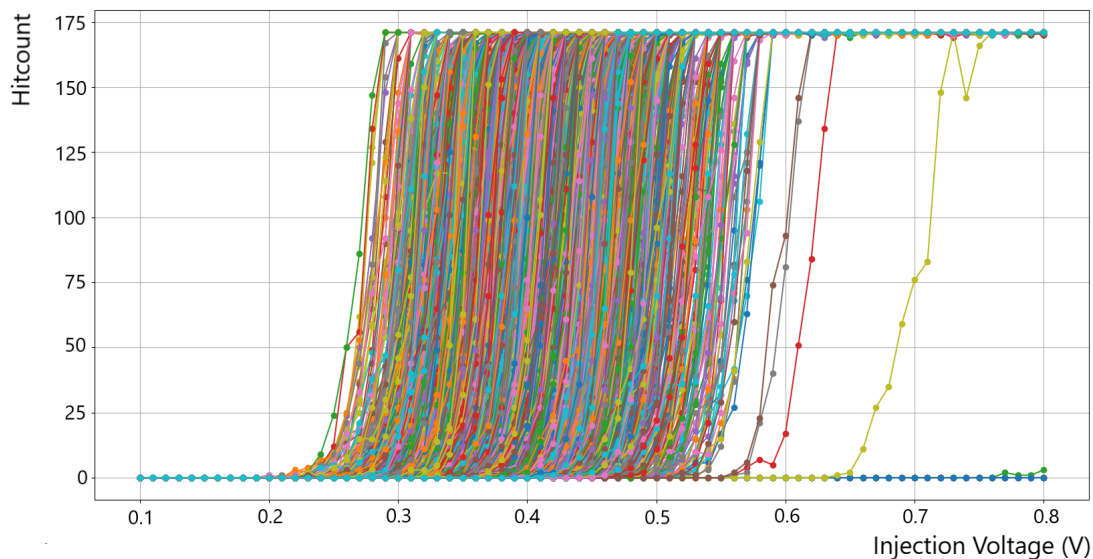


Figure 4.12: S-curve scan of the full RD50-MPW3 pixel matrix. Each line represents one pixel’s hitcount as a function of the injection voltage.

In order to evaluate the in-pixel electronics of the RD50-MPW3, an integrated injection mechanism has been used on the chip. This feature enables injecting a voltage pulse directly into the comparator, facilitating the simulation of hits without actual particle interactions. Such injections were primarily utilised to assess the threshold behaviour of the pixels. As indicated by the modified condition in Equation 3.2, where  $V_{\text{preamp}} \rightarrow V_{\text{inj}}$ , no hits are expected for low injection voltages  $V_{\text{inj}}$ , and all hits should be registered for sufficiently high values of  $V_{\text{inj}}$ . With the parameters set for the *S-Curve* in Figure 4.12, a transition from 0  $\rightarrow$  175 hits is anticipated. The *S-Curves* illustrates the differences between the different pixels, which requires fine-tuning the threshold via the trimdac.

Manufacturing variances and potential crosstalk from various chip components may cause slight variations in threshold levels across individual pixels, even under identical configurations. These discrepancies were explored through an *S-Curve* scan across the entire matrix, with results depicted in Figure 4.12. This measurement indicated that despite uniform settings, the injection voltage  $V_{\text{inj}}$  at which 50% of hits are detected varies significantly, ranging from approximately 260 mV to 710 mV. Consequently, the actual threshold setting for the matrix exhibited variations up to 450 mV. This variation would have to be compensated via the trim-dac of each pixel, which was not performed in this thesis. The measurements were added as the principal investigation, as the RD50-MPW4 is this thesis's main point of interest.



### 4.3 RD50-MPW4

The RD50-MPW4 represents the fourth iteration of *HV-CMOS* technology developed by the CERN-RD50 CMOS collaboration. In previous sections, the observations about the RD50-MPW3 have raised concerns about its performance. The hope for the RD50-MPW4 was that most, if not all, problems would be solved or significantly improved; all remaining affiliated measurements can be found in [Appendix D.5](#).

#### 4.3.1 IV Curve of the RD50-MPW4 Pixel Matrix

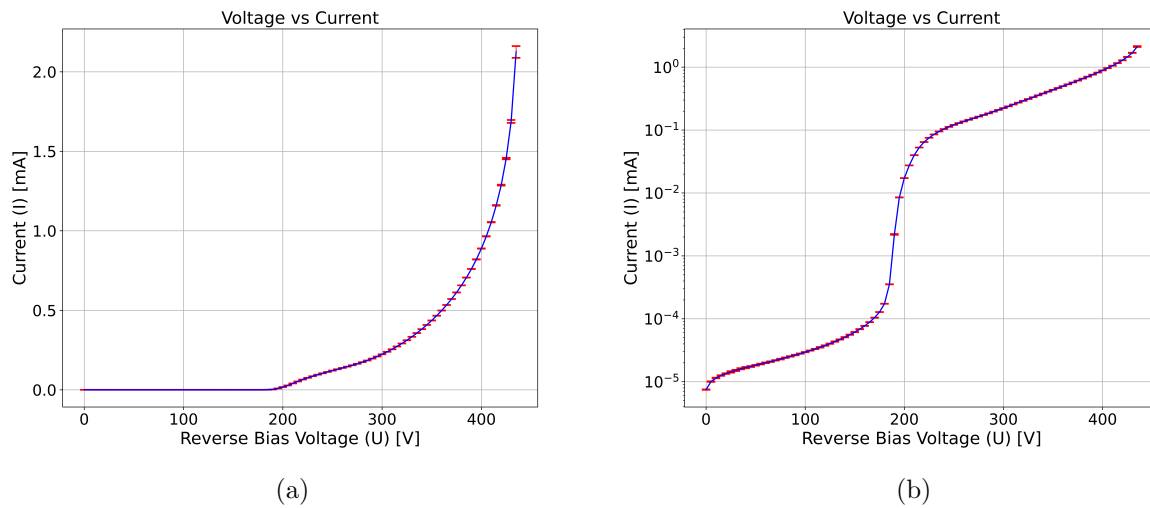


Figure 4.13: IV curve analysis of the RD50-MPW4 pixel matrix in both linear (a) and logarithmic (b) scales, demonstrating the leakage current characteristics over a voltage range from 0 to 450 V. These plots verify the detector’s operational integrity and suitability for high-voltage measurements.

An IV measurement was conducted in order to characterize the electrical properties and ensure the operational stability of the RD50-MPW4 pixel matrix. The measurements were performed with a reverse bias voltage ranging from 0 to 435 V and varied in steps of 5.0 V. The IV curve can be used to assess the pixel matrix’s breakdown characteristics and leakage current behaviours. A waiting period of 30 seconds was imposed after each step to allow for stabilization of the leakage current and thereby ensure an accurate measurement by mitigating transient effects that could skew the results. The measurements mean and standard deviation were calculated from 40 samples per data point on the IV curve and graphically represented in the curve. This is shown in [Figure 4.13](#).

The leakage current (or dark current), which should ideally be minimal in a perfectly blocking diode under reverse bias, was continuously measured. In the RD50-MPW scenarios, however, any current that does flow under these conditions is termed "leakage current". From the IV curves illustrated in [Figure 4.13](#), the leakage current can be assessed for the RD50-MPW4 pixel matrix. If leakage current flows through the active pixel area, it can introduce noise that degrades the signal quality or, in severe cases, can lead to pixel failure due to excessive current. Conversely, when leakage current passes through the guard ring, it results in thermal effects rather than immediate damage, as exemplified by a leakage current of 2 mA at a reverse bias of 450 V, producing about 1 W of heat. This heat can increase the sensor’s temperature, potentially affecting its overall performance and durability. Managing the leakage current is necessary for maintaining the operational

integrity and efficiency of the detectors.

This current indicates the sensor's health and ability to withstand operational conditions without degradation. A sudden increase in leakage current around 200 V probably suggests that the sensor is reaching full depletion to the backside, a condition observed when the reverse bias voltage is sufficient to fully deplete the sensor material from back to front, maximizing its active volume and sensitivity. Beyond 435 V, the current levels approached the potentially dangerous range of the voltage range, leading to the interruption of measurements to avoid risking damage to the sensor. This point, however, does not necessarily represent a breakdown.

### 4.3.2 Charge Injection and $ToT$ Calibration

For the RD50-MPW4, the same calibration was performed as for the RD50-MPW3. The measurements using injection voltages for the single pixel were done over the range of 200 mV to 1600 mV, with a step size of 100 mV.  $ToT$  was calibrated using the equation  $Q = C \cdot V$ , where  $C = 2.8$  fF is the capacitance of the pixel's frontend electronics, and  $V$  is the injection voltage.

Through this method, the  $ToT$  of 813 ns (Figure D.22) corresponds to an electron count of approximately 44000 electrons as can be seen from Figure 4.14. It is assumed that all the measurement results of the MPW4 are made at the same parameters measured as those for the injection voltage. However, this is an assumption that will need to be verified in the future.

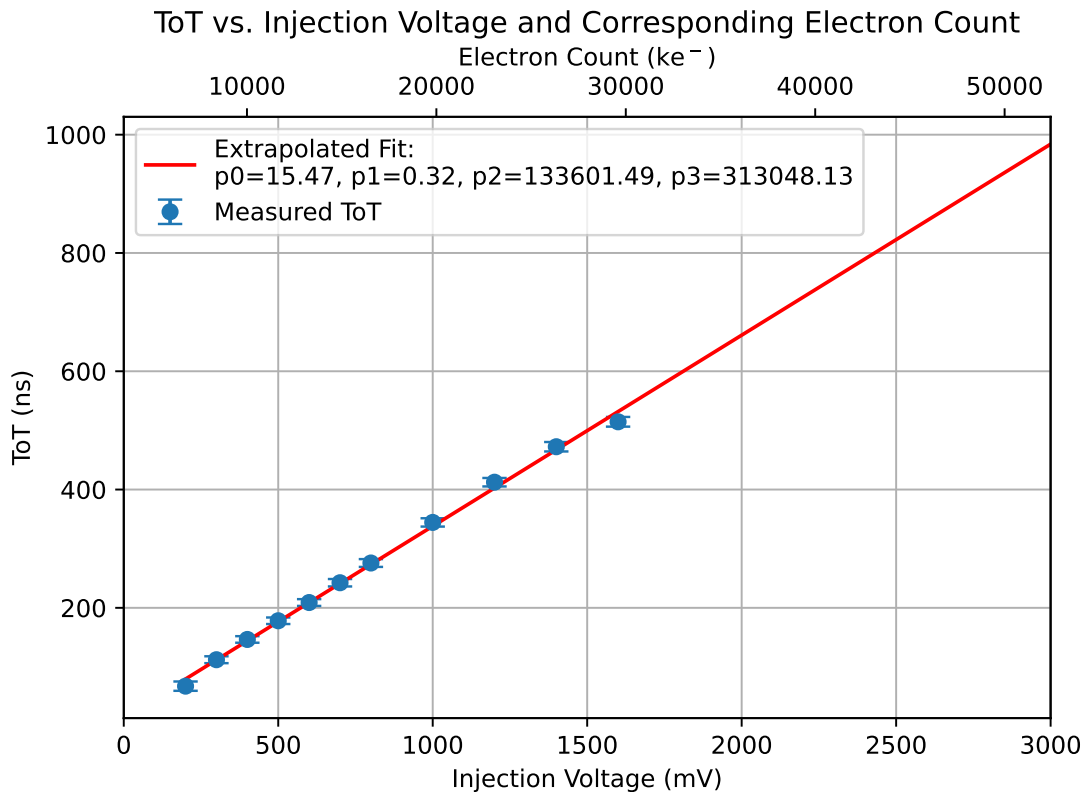


Figure 4.14: Graph depicting the correlation between injected charge (in mV and in electrons) and measured  $ToT$  of the MPW4. Where the fit function is:  $f(x, p_0, p_1, p_2, p_3) = p_0 + p_1x - \frac{p_2}{p_3 - x}$ .

In the context of the interaction of particles with sensor materials, a *MIP* typically deposits

about 80 electrons per micrometre as it traverses silicon. Considering this rate, for a silicon thickness of 300  $\mu\text{m}$ , a *MIP* would deposit approximately 24000 electrons. So, the system measures a lower injection voltage than it would be measured by *MIPs*. Hence, therefore, the results depicted here and further down below will have worse performances than when actually measuring *MIPs*.

### 4.3.3 External Clock Effects

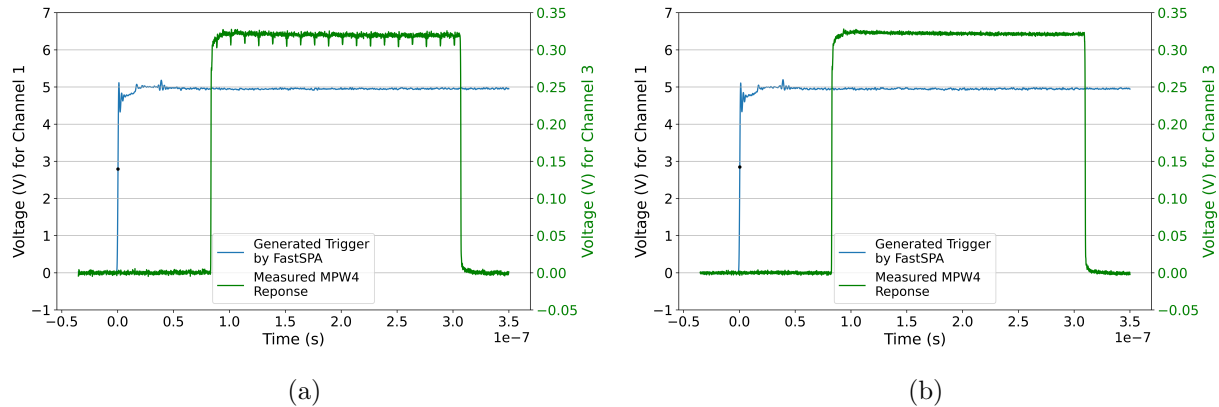


Figure 4.15: Both plots depict a single waveform of the preliminary MPW4 measurements where the clock influence is visible, (a) does so for the clock-on situation and (b) for the clock-off situation.

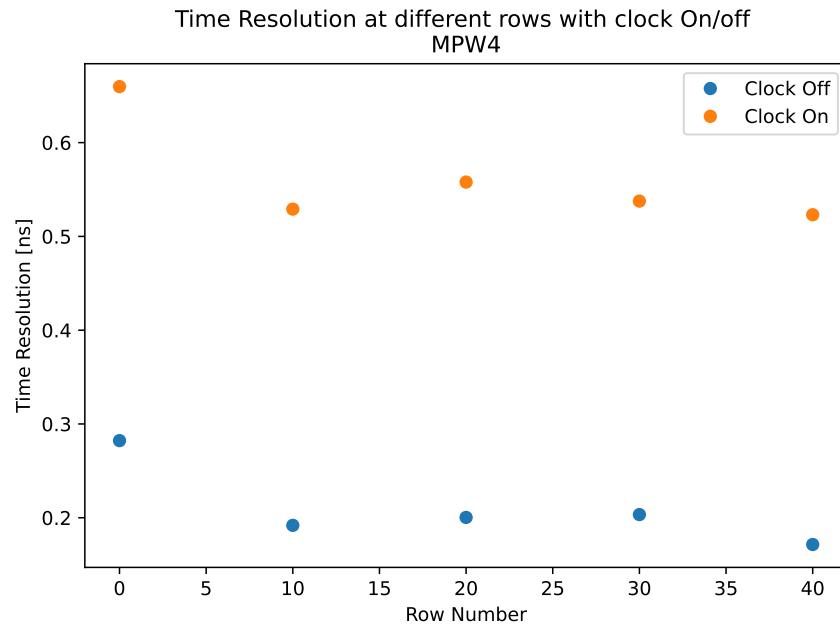


Figure 4.16: Preliminary measurement of time resolution in the RD50-MPW4 under the influence of external clock noise. The plot compares the time resolution at a reverse bias of 100 V and a charge level of approximately 12500 electrons, with and without the external clock activated. Data for rows 50 and 60 were not stored properly and, therefore, considered lost.

Similar to the RD50-MPW3, an analysis of a singular waveform frame revealed that the induced clock noise of 40 MHz (Figure 4.15) was still present for the RD50-MPW4. However, the clock's effect had a less pronounced impact on the time resolution than it was for the RD50-MPW3. The results showed that at a 100 V applied reverse bias voltage the time resolution in the absence of the clock noise ( $\sigma_t = 171$  ps at a charge of approximately 12500 electrons) surpasses that observed with the clock engaged ( $\sigma_t = 523$  ps at a charge of approximately 12500 electrons), still showing a significant improvement (Figure 4.16). This emphasizes the impact the external clock still has on waveform quality, and the optimisation of the clock integration within the digital readout system could be further improved.

#### 4.3.4 Reverse Bias Voltage Effects on the RD50-MPW4

A single-pixel analysis was conducted for the RD50-MPW4, focusing on a pixel located centrally within the matrix in terms of columns and rows. For this purpose and by convenience, the pixel at column 35 and row 41 was measured. This investigation explored the device's capability to operate and function under a reverse bias voltage of up to 500 V and hopefully observe a time resolution in the tens of picoseconds. The impacts of varying reverse bias voltages on the pixel's performance parameters, such as  $ToT$  and time resolution, are documented. As illustrated in Figure 4.17a, there is an increase in  $ToT$ , in response to an increased reverse bias voltage, with the full depletion depth observed at approximately 200 V.

Figure 4.17b shows the implications of increased depletion depth for time resolution and Figure 4.17c shows the same graph but then for measured  $ToT$ , as above this comes at a charge of 44000 electrons. In scenarios where the clock remains activated, time resolution improves from 2293 ps at lower voltages to 347 ps at higher voltages. Conversely, with the clock deactivated, an even more pronounced enhancement in time resolution is observed, decreasing from 1228 ps at low voltages to 66 ps at higher voltages. This time resolution of 66 ps is in the same order of magnitude as the desired goal.

As discussed earlier in this thesis, a detector's time resolution improves with the steepness or slope of the signal's rising edge, which is enhanced by applying a higher reverse bias voltage to the detector. Resulting in a larger electric field across the detector's depletion zone, enabling faster charge collection and sharper rise times in the output signal.

However, during measurements (Figure 4.17), the expected persisting improvement in time resolution unexpectedly flattened at 200 V and higher reverse bias voltages. This deviation can be linked to the bandwidth limitations of the Preamp within the Charge Sensitive Amplifier (CSA) used in the setup, as can be seen in Figure 3.4. As the reverse bias voltage increases, so does the electric field across the sensor, increasing the signal slope further. However, the effective bandwidth of the amplifier likely imposes a limit on the frequencies it can accurately amplify.

The amplifier's frequency response influences the measured rise time of the signal. For instance, if the amplifier has a limited bandwidth, it cannot optimally amplify higher frequency components of the signal, which are crucial for achieving faster rise times. As a result, these higher-frequency components are attenuated relative to the lower-frequency components. Consequently, the signal's observed rise time is longer than expected, leading to a less steep slope and, therefore, poorer time resolution than could be achieved at those high electric fields.

This limitation was already evident during the laser measurements conducted with the diode, where the observed rise time was significantly longer than the manufacturer's specifications for the diode's performance. It highlights the discrepancy of the amplifier bandwidth in the overall performance of timing measurements in high-speed, high-precision experimental setups. Therefore, for accurate time resolution measurements in future experiments, it is necessary to consider the

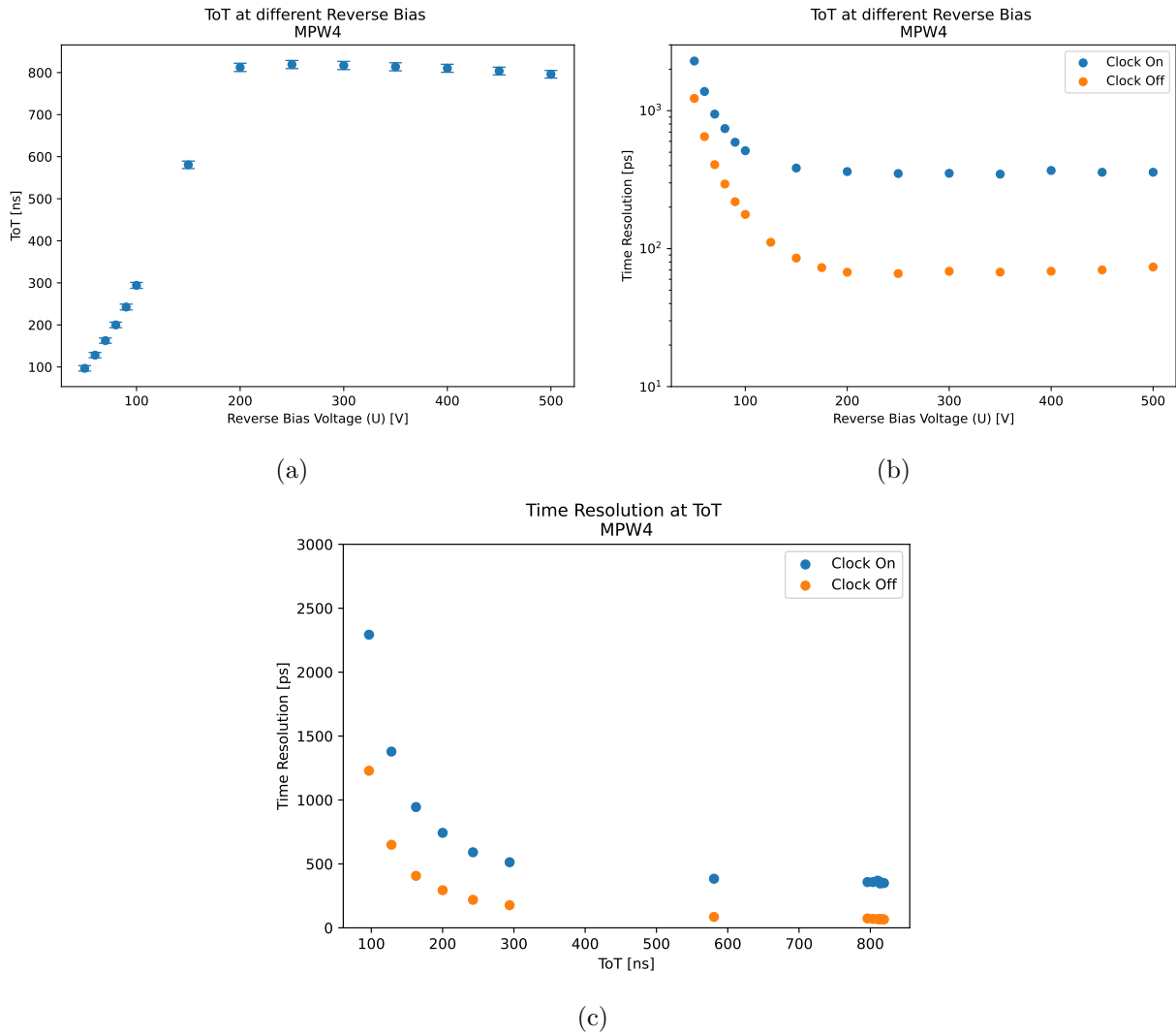


Figure 4.17: Analysis of the RD50-MPW4's response to different reverse bias voltages, illustrating the effects on both  $ToT$  and time resolution. In (a), the variation of  $ToT$  as a function of applied reverse bias voltage indicates enhanced charge collection capabilities at higher voltages. In (b), the improvement in time resolution with increasing reverse bias voltage highlights the device's improved performance at full depletion depth. In (c), the  $ToT$  with increasing reverse bias voltage is depicted, showing the reach of the full depletion depth.

bandwidth constraints of the amplification system. Selecting an amplifier with a bandwidth that matches or exceeds the highest frequency components expected in the signal can mitigate this effect. Additional measurements must be performed in the future to confirm this hypothesis about the amplifier; however, due to limited time, it was not further investigated here.

## 5 Discussion

This thesis examined the time resolution of HV-CMOS-based silicon detectors using picosecond pulsed infrared lasers. The goal of this thesis was to better understand and observe the improvements made for the RD50-MPW series. The desired time resolution would have been in the range of tens of picoseconds. The minimum time resolution was found to be 66 ps. This finding and the others highlight several interactions between the detector properties and the setup that influence performance outcomes. The discussion surrounding the impact of external clock signals and the importance of amplifier bandwidth on time resolution has opened new avenues for optimizing detector systems in high-energy physics applications.

### 5.1 Implications of External Clock Effects

The role of clocking mechanisms, particularly the difference between the external clock-on and clock-off configurations, showed large influences on the output performance. These influences of the external clock on the  $ToT$  and time resolution illustrated the sensitivity of RD50-MPW series digital readout systems to external timing factors. Highlighting design considerations of additional shielding for future improvements.

### 5.2 Implications of PreAmplifier

One notable observation was made that probably points towards the role of amplifier limitations on the achievable time resolution, particularly at higher reverse bias voltages. As discussed, the amplifier's bandwidth could restrict the signal's effective rise time, thus capping the slope and, consequently, the time resolution. This phenomenon was observed during the diode testing with lasers, where the actual device performance deviated from manufacturer specifications due to bandwidth constraints of the measurement system. Due to the constraints on available time, this hypothesis was not yet tested; however, it is presumed to be very likely the cause of the limitation in time resolution.

### 5.3 Time Resolution Improvements and Anticipated *MIP* Performance

The improvement in time resolution with increased reverse bias voltage, particularly in the clock-off scenario, highlights the potential of RD50-MPW4 in applications requiring high time accuracy. Once the issues with the Preamp are dealt with, it is anticipated that the time resolution could further improve, potentially going under the tens of picoseconds.

Despite these findings, it is important to note that the current measurements were conducted using a laser, representing an ideal scenario for assessing the detector's performance characteristics. Real-world applications involving Minimum Ionizing Particles (*MIPs*) are likely to yield poorer outcomes. Future studies must include test beam experiments to assess the RD50-MPW4's effectiveness accurately under typical operational conditions. Providing insights into the impact of *MIPs* on the detector's performance, offering a realistic evaluation of the RD50-MPW4 capabilities in high-energy physics applications.

### 5.4 Constraints on Time

Given the constraints imposed by the limited time available for this project, a full charge calibration across all pixels in the matrix could not be completed. Consequently, this thesis mainly provides a comparative analysis of the performance characteristics of the RD50-MPW3 and RD50-MPW4.

Full calibration and full pixel optimization are recommended for the future to gain more definitive conclusions about the capabilities of the RD50-MPW4 independently.

Despite the limited time, the findings from the data demonstrate improvements in time resolution and reduced external clock interference compared to the previous iteration. These improvements are promising, indicating that the RD50-MPW4 may offer the desired time resolution range that would allow for integrating time as the fourth tracking parameter.

## 6 Outlook

Future work should continue to explore the optimization of detector and readout electronics to enhance the time resolution further. More digital processing tools that can compensate for system imperfections, such as amplifier bandwidth limitations or clock-induced noise, are desired. Additional shielding and incorporation of a high-end amplifier could potentially correct for these effects, improving the overall accuracy and reliability of the detectors when measuring time resolution at high applied reverse bias voltages.

Lastly, as the field of high-energy physics progresses towards experiments requiring ever more precise measurements, such as at the HL-LHC, the need for detectors that can provide both high spatial resolution and excellent time resolution will continue to grow in order to incorporate time as the fourth parameter. The research presented in this thesis contributes to this ongoing effort and sets the framework for the next generation of particle detection technology.

## 7 Conclusion

This thesis has provided an exploration of the advancements in HV-CMOS-based silicon detectors, particularly focusing on the RD50-MPW series and their application in high-energy physics experiments. The investigation into the RD50-MPW3 and RD50-MPW4 have yielded insights into the challenges and capabilities of these devices under various experimental conditions.

This research project identified enhancements in time resolution and signal integrity in the RD50-MPW4 compared to its predecessor. Where the measured time resolution went from  $\sigma_t = 2.01$  ns to  $\sigma_t = 347$  ps with clock enabled. For clock disabled, the measured time resolution went from  $\sigma_t = 293$  ps to  $\sigma_t = 66$  ps. This improvement is mainly attributable to improvements in pixel architecture and digital readout systems, which have contributed to better control of noise and external clock influences. The improvements made in the design of the RD50-MPW4 allow the chip to receive bias voltages of 600 V, and superior time resolution is expected to be measured at these voltages. Despite these advancements, challenges remain, particularly in achieving time resolution below the tens of picoseconds due to system and component limitations such as the Preamplifier bandwidth constraints.

Furthermore, the results have highlighted the importance of environmental control, demonstrating that even minor variations in temperature can have measurable effects on detector performance. This sensitivity demonstrates the necessity for environmental control measures, especially in future high-luminosity environments, where the integration of time as the fourth parameter is dependent on the precision of the time resolution.

In conclusion, while progress may have been made in the development of silicon-based particle detectors, the progress towards perfecting these devices continues. The insights gained from the RD50-MPW series provide valuable directions for future research and development, pointing towards the need for integrated solutions that address both the technological and environmental factors that affect detector performances.

## Acknowledgements

Everything that has a beginning has an end. As this chapter of my academic journey concludes, I reflect on the profound experiences and invaluable support that shaped this research project on the time resolution of an HV-CMOS-based silicon detector.

First and foremost, I extend my deepest gratitude to my mentors at SRON. Dr. Ir. Pieter Dieleman has supported and guided me through this project, and I am thankful for that. I must thank Dr. Gert de Lange, who has always encouraged and supported me in pursuing a career in the sciences; it is a field of truth and beauty, worthy of devotion and admiration.

I am extremely grateful to have Dr. Uwe Kraemer as my daily research supervisor. His keen insights and readiness to invest time have greatly enhanced my understanding and appreciation of our work. In conversations and meetings, he always took my ideas seriously and helped me develop my vision for the project. I couldn't have had a better supervisor at the Detector R&D department of Nikhef, and I considered him more than just a colleague.

Much of the research literature presented in this thesis continues the earlier efforts of the CERN-RD50 collaboration, and I want to thank all my colleagues for their help and support. I have directly worked and collaborated with my colleagues and friends of the detector R&D department of Nikhef: Daan Oppenhuis, Tjip Bischoff, Petja Skomina, Evridiki Chatzianagnostou, Titus Veit, Andrej Sarnatskiy, Kevin Heijhoff, Uwe Kraemer, Isis Hobus, Jory Sonneveld, Timesh Mistry, Roberto Russo, Martin Fransen, and Martin van Beuzekom. I want to thank them all for their time; they enriched my research experience and made it both fruitful and enjoyable during my time at Nikhef.

Lastly, the unwavering support of my family and friends has been a cornerstone of my journey. As for my parents, your belief in my ambitions and emotional sustenance has strengthened me in hard times. Now, in particular, to my girlfriend, I deeply appreciate your support in all the choices I make, and your unconditional love has been my constant source of strength and inspiration throughout all these years.



## References

- [1] *Framework TDR for the LHCb Upgrade II: Opportunities in flavour physics, and beyond, in the HL-LHC era*, Tech. Rep. (CERN, Geneva, Switzerland, 2021).
- [2] The CMS collaboration *et al.*, *The phase-2 upgrade of the CMS tracker technical design report*, Tech. Rep. (CERN, Geneva, Switzerland, 2017).
- [3] S. Charley, “The LHC does a dry run,” (2015).
- [4] K. Černý, T. Sýkora, M. Taševský, *et al.*, *Journal of Instrumentation* **16**, P01030 (2021).
- [5] J. Sonneveld, “Design and performance of HV-CMOS sensors for future colliders by the RD50 collaboration,” (2023), [arXiv:2307.08600 \[physics.ins-det\]](https://arxiv.org/abs/2307.08600) .
- [6] D. Nobels, *Characterisation of RD-50 HV-CMOS Sensors*, Master’s thesis, University of Amsterdam (2023).
- [7] M. K. Gaillard, P. D. Grannis, and F. J. Sciulli, *Rev. Mod. Phys.* **71**, S96 (1999).
- [8] I. Brivio and M. Trott, *Physics Reports* **793**, 1 (2019), the standard model as an effective field theory.
- [9] J. P. Vega and G. Villadoro, *Journal of High Energy Physics* **2015**, 1 (2015).
- [10] T. Schucker, *arXiv preprint arXiv:0708.3344* (2007).
- [11] M. Dine and A. Kusenko, *Rev. Mod. Phys.* **76**, 1 (2003).
- [12] H. Gisbert and A. Pich, *Reports on Progress in Physics* **81**, 076201 (2018).
- [13] G. Bertone and T. M. P. Tait, *Nature* **562**, 51 (2018).
- [14] S. Weinberg, *Rev. Mod. Phys.* **61**, 1 (1989).
- [15] Y. Farzan and M. Tórtola, *Frontiers in Physics* **6** (2018), 10.3389/f-ph.2018.00010.
- [16] A. Joyce, B. Jain, J. Khoury, and M. Trodden, *Physics Reports* **568**, 1 (2015), beyond the cosmological standard model.
- [17] Y. Nakahama and on behalf of the ATLAS Collaboration, *Journal of Physics: Conference Series* **664**, 082037 (2015).
- [18] The ALICE collaboration *et al.*, *Technical Design Report for the Upgrade of the ALICE Inner Tracking System*, Tech. Rep. (CERN, Geneva, Switzerland, 2013).
- [19] K. Heijhoff, *When and Where: Precision Time Measurements with Hybrid Silicon Pixel Detectors*, *Ph.D. thesis*, Universiteit van Amsterdam (2023).
- [20] R. E. Geertsema, *CHASING TIME: Characterisation and application of precision temporal measurements with silicon pixel detectors*, *Ph.D. thesis*, Maastricht University (2024).
- [21] H. F.-W. Sadrozinski, A. Seiden, and N. Cartiglia, *Reports on Progress in Physics* **81**, 026101 (2017).
- [22] N. Cartiglia, R. Arcidiacono, B. Baldassarri, M. Boscardin, F. Cenna, G. Dellacasa, G.-F. Dalla Betta, M. Ferrero, V. Fadeyev, Z. Galloway, *et al.*, *Nuclear Instruments and Methods in Physics Research Section A: Accelerators, Spectrometers, Detectors and Associated Equipment* **845**, 47 (2017), proceedings of the Vienna Conference on Instrumentation 2016.
- [23] L. D. Landau, *J. Phys.* **8**, 201 (1944).
- [24] D. Wilkinson, *Nuclear Instruments and Methods in Physics Research Section A: Accelerators, Spectrometers, Detectors and Associated Equipment* **383**, 513 (1996).

- [25] The CMS collaboration *et al.*, *CMS Physics Technical Design Report Volume I: Detector Performance and Software*, Tech. Rep. (CERN, Geneva, Switzerland, 2006).
- [26] InspireHEP, “CERN RD50: Development of Radiation Hard Semiconductor Devices for Very High Luminosity Colliders,” <https://inspirehep.net/experiments/1108429>, accessed: 2024-04-13.
- [27] R. Marco-Hernández, *Instruments* **4** (2020), 10.3390/instruments4040036.
- [28] A. Tremisin, J. Vallergera, and O. Siegmund, *Nuclear Instruments and Methods in Physics Research Section A: Accelerators, Spectrometers, Detectors and Associated Equipment* **949**, 162768 (2020).
- [29] A. Volta and G. N. C. Cowper, *Philosophical Transactions of the Royal Society of London* **72**, 237 (1782).
- [30] G. Busch, *European Journal of Physics* **10**, 254 (1989).
- [31] M. Becquerel, *Comptes rendus hebdomadaires des séances de l’Académie des sciences* **9**, 561 (1839).
- [32] R. Williams, *The Journal of Chemical Physics* **32**, 1505 (1960).
- [33] P. J. Van Heerden, *The Crystal Counter: A New Instrument in Nuclear Physics...* (Nv Noordhollandsche uitgevers maatschappij, 1945).
- [34] K. G. McKay, *Phys. Rev.* **76**, 1537 (1949).
- [35] E. Haase, M. Fawzi, D. Saylor, and E. Velten, *Nuclear Instruments and Methods* **97**, 465 (1971).
- [36] W. S. Boyle and G. E. Smith, *The Bell System Technical Journal* **49**, 587 (1970).
- [37] G. F. Amelio, M. F. Tompsett, and G. E. Smith, *Bell System Technical Journal* **49**, 593 (1970).
- [38] H. Shirakawa, E. J. Louis, A. G. MacDiarmid, C. K. Chiang, and A. J. Heeger, *J. Chem. Soc., Chem. Commun.* , 578 (1977).
- [39] C. W. Tang, *Applied Physics Letters* **48**, 183 (1986).
- [40] E. Heijne, L. Hubbeling, B. Hyams, P. Jarron, P. Lazeyras, F. Piuz, J. Vermeulen, and A. Wylie, *Nuclear Instruments and Methods* **178**, 331 (1980).
- [41] J. Kemmer, *Nuclear Instruments and Methods* **169**, 499 (1980).
- [42] B. Hyams, U. Koetz, E. Belau, R. Klanner, G. Lutz, E. Neugebauer, A. Wylie, and J. Kemmer, *Nuclear Instruments and Methods in Physics Research* **205**, 99 (1983).
- [43] S. Gaalema, *IEEE Transactions on Nuclear Science* **32**, 417 (1985).
- [44] M. Catanesi, H. Beker, W. Beusch, M. Campbell, E. Chesi, J. Clemens, P. Delpierre, D. DiBari, E. Heijne, P. Jarron, V. Lenti, V. Manzari, M. Morando, F. Navach, C. Neyer, F. Pengg, R. Perego, M. Pindo, E. Quercigh, N. Redaelli, D. Sauvage, G. Segato, and S. Simone, *Nuclear Physics B - Proceedings Supplements* **32**, 260 (1993).
- [45] F. Anghinolfi, P. Aspell, K. Bass, W. Beusch, L. Bosisio, C. Boutonnet, P. Burger, M. Campbell, E. Chesi, C. Claeys, *et al.*, *IEEE Transactions on Nuclear Science* **39**, 654 (1992).
- [46] The ALICE Collaboration, K. Aamodt, *et al.*, *Journal of Instrumentation* **3**, S08002 (2008).
- [47] The ATLAS Collaboration, G. Aad, *et al.*, *Journal of Instrumentation* **3**, S08003 (2008).
- [48] The LHCb Collaboration *et al.*, *Journal of Instrumentation* **3**, S08005 (2008).

- [49] The CMS Collaboration, S. Chatrchyan, *et al.*, *Journal of Instrumentation* **3**, S08004 (2008).
- [50] S. M. Sze, *Semiconductor devices: physics and technology* (John Wiley & sons, 2008).
- [51] A. Kitai, *Principles of Solar Cells, LEDs and Related Devices: The Role of the PN Junction* (John Wiley & Sons, 2018).
- [52] K. Olive, *Chinese Physics C* **38**, 090001 (2014).
- [53] M. Veale, S. Bell, D. Duarte, M. French, A. Schneider, P. Seller, M. Wilson, A. Lozinskaya, V. Novikov, O. Tolbanov, A. Tyazhev, and A. Zarubin, *Nuclear Instruments and Methods in Physics Research Section A: Accelerators, Spectrometers, Detectors and Associated Equipment* **752**, 6 (2014).
- [54] S. Watanabe, T. Takahashi, Y. Okada, C. Sato, M. Kouda, T. Mitani, Y. Kobavashi, K. Nakazawa, Y. Kuroda, and M. Onishi, in *2001 IEEE Nuclear Science Symposium Conference Record (Cat. No.01CH37310)*, Vol. 4 (2001) pp. 2434–2438 vol.4.
- [55] C. Kenney, S. Parker, J. Segal, and C. Storment, *IEEE Transactions on Nuclear Science* **46**, 1224 (1999).
- [56] G. Pellegrini, P. Fernández-Martínez, M. Baselga, C. Fleta, D. Flores, V. Greco, S. Hidalgo, I. Mandić, G. Kramberger, D. Quirion, and M. Ullan, *Nuclear Instruments and Methods in Physics Research Section A: Accelerators, Spectrometers, Detectors and Associated Equipment* **765**, 12 (2014).
- [57] S. Girvin and K. Yang, *Modern Condensed Matter Physics* (Cambridge University Press, 2019).
- [58] A. Poruba, J. Springer, L. Mullerova, A. Beitlerova, M. Vaněček, N. Wyrshch, and A. Shah, *Journal of Non-Crystalline Solids* **338-340**, 222 (2004), proceedings of the 20th International Conference on Amorphous and Microcrystalline Semiconductors.
- [59] M. J. Berger, M. Inokuti, H. H. Andersen, H. Bichsel, D. Powers, S. M. Seltzer, D. Thwaites, and D. E. Watt, *Reports of the International Commission on Radiation Units and Measurements* **os-25**, 107 (1993).
- [60] M. J. Berger, M. Inokuti, H. H. Andersen, H. Bichsel, J. A. Dennis, D. Powers, S. M. Seltzer, and J. E. Turner, *Reports of the International Commission on Radiation Units and Measurements* **os-19**, 55 (1984).
- [61] M. J. Berger, M. Inokuti, H. H. Andersen, H. Bichsel, D. Powers, S. M. Seltzer, D. Thwaites, and D. E. Watt, *Reports of the International Commission on Radiation Units and Measurements* **os-25**, 183 (1993).
- [62] D. E. GROOM, N. V. MOKHOV, and S. I. STRIGANOV, *Atomic Data and Nuclear Data Tables* **78**, 183 (2001).
- [63] C. Grupen and B. Shwartz, *Particle detectors* (Cambridge university press, 2008).
- [64] W.-M. Yao *et al.*, *Progress of Theoretical and Experimental Physics* **2020**, 083C01 (2020).
- [65] D. E. Groom and S. R. Klein, *The European Physical Journal C - Particles and Fields* **15**, 163 (2000).
- [66] M. J. Berger, M. Inokuti, H. H. Andersen, H. Bichsel, J. A. Dennis, D. Powers, S. M. Seltzer, and J. E. Turner, *Reports of the International Commission on Radiation Units and Measurements* **os-19**, 15 (1984).
- [67] F. Berghmans, B. Brichard, A. F. Fernandez, A. Gusarov, M. V. Uffelen, and S. Girard, *Optical Waveguide Sensing and*

- Imaging*, edited by W. J. Bock, I. Gannot, and S. Tanev (Springer Netherlands, Dordrecht, 2008) pp. 127–165.
- [68] H. Bichsel, *Rev. Mod. Phys.* **60**, 663 (1988).
- [69] P. Drude, *Annalen der Physik* **306**, 566 (1900).
- [70] P. Drude, *Annalen der Physik* **308**, 369 (1900).
- [71] B. Pilsl, “Data acquisition systems for depleted monolithic active pixel sensors,” (2022).
- [72] J. Xanthakis, *Electronic Conduction: Classical and Quantum Theory to Nanoelectronic Devices*, Textbook Series in Physical Sciences (CRC Press, 2020).
- [73] C. Jacoboni, C. Canali, G. Ottaviani, and A. Alberigi Quaranta, *Solid-State Electronics* **20**, 77 (1977).
- [74] S. S. Li and W. R. Thurber, *Solid-State Electronics* **20**, 609 (1977).
- [75] A. Sharma and on behalf of the ATLAS ITk Collaboration, *Journal of Physics: Conference Series* **2374**, 012068 (2022).
- [76] M. Demarteau, Y. Arai, H.-G. Moser, and V. Re, in *2009 IEEE International Conference on 3D System Integration* (2009) pp. 1–7.
- [77] B. Hiti, *Radiation Hardness of CMOS detector prototypes for ATLAS Phase-II ITk upgrade*, Ph.D. thesis, Ljubljana U. (2020).
- [78] R. Turchetta, J. Berst, B. Casadei, G. Claus, C. Colledani, W. Dulinski, Y. Hu, D. Husson, J. Le Normand, J. Riester, G. Deptuch, U. Goerlach, S. Higuieret, and M. Winter, *Nuclear Instruments and Methods in Physics Research Section A: Accelerators, Spectrometers, Detectors and Associated Equipment* **458**, 677 (2001).
- [79] P. Yang, G. Aglieri Rinella, C. Cavicchioli, P. Chalmet, N. Chanlek, A. Collu, C. Gao, H. Hillemanns, A. Junique, M. Kofarago, M. Keil, T. Kugathanan, D. Y. Kim, J. Kim, A. Lattuca, C. Marin Tobon, D. Marras, M. Mager, P. Martinengo, and J. Yi, *Journal of Instrumentation* **10**, C03030 (2015).
- [80] C. Zhang, in *RD50 40st workshop* (2022).
- [81] S. Xie, Z. Zhu, X. Zhang, Q. Xie, H. Yu, Y. Zhang, J. Xu, and Q. Peng, *Sensors* **21** (2021), 10.3390/s21144681.
- [82] QPhotonics, “Wavelength stabilized single mode fiber coupled laser diode 5mw @ 980nm, qfbgld-980-5,” (2024), accessed: 2024-03-12.
- [83] GOPhotonics, “Laser diode QFBGLD-980-5,” (2024), accessed: 2024-03-12.
- [84] NKTPhotonics, “PILAS – picosecond pulsed diode lasers,” (2024), accessed: 2024-03-12.
- [85] Tektronix, “6 series mso mixed signal oscilloscope,” <https://www.tek.com/en/products/oscilloscopes/6-series-mso> (2023), accessed: 2023-03-10.
- [86] Keysight Technologies, “InfiniiVision CSO-X 3054A, 4+16 Channel, 500 MHz, 5 GSps, 4 Mpts,” <https://nl.farnell.com/keysight-technologies/msox3054t/oscilloscope-20-ch-500mhz-5gsps/dp/2449649> (), accessed: 2023-03-10.
- [87] Keysight Technologies, “Infiniium mxr-series oscilloscope: 6 ghz, 4 channels,” (2021), accessed: 2023-03-10.
- [88] Keysight Technologies, “Keysight 33600A Series Waveform Generators Data Sheet,” <https://www.keysight.com/us/en/assets/7018-04123/data-sheets-archived/5991-3272.pdf> (), accessed: 2024-04-02.

- [89] thorlabs, “DET08CFC(/M) Fiber Input InGaAs Biased Detector User Guide,” (2024), accessed: 2024-03-12.
- [90] thorlabs, “High-speed fiber-coupled detectors specs,” (2024), accessed: 2024-03-12.
- [91] E. Vilella, *Nuclear Instruments and Methods in Physics Research Section A: Accelerators, Spectrometers, Detectors and Associated Equipment* **1034**, 166826 (2022).
- [92] I. Perić *et al.*, *Nuclear Instruments and Methods in Physics Research Section A: Accelerators, Spectrometers, Detectors and Associated Equipment* **565**, 178 (2006), proceedings of the International Workshop on Semiconductor Pixel Detectors for Particles and Imaging.
- [93] C. Zhang, G. Casse, N. Massari, E. Vilella, and J. Vossebeld, *PoS TWEPP2019*, 045 (2020).
- [94] M. Franks *et al.*, in *14th Trento Workshop on Advanced Silicon Radiation Detectors, Trento, Italy* (2019).
- [95] R. M. Hernández, “Latest Depleted CMOS Sensor Developments in the CERN RD50 Collaboration,” in *Proceedings of the 29th International Workshop on Vertex Detectors (VERTEX2020)*.
- [96] E. Vilella Figueras, in *Proceedings of The 28th International Workshop on Vertex Detectors—PoS (Vertex2019)*, Vol. 373 (Sissa Medialab, 2020).
- [97] C. Zhang, G. Casse, N. Massari, E. Vilella, and J. Vossebeld, *PoS TWEPP2019*, 045 (2020).
- [98] P. Sieberer, *Monolithic active pixel sensors for high rate tracking detectors*, Ph.D. thesis, Technische Universität Wien (2023).
- [99] CERN-RD50 Collaboration, *RD50-MPW4 Chip Documentation*, CERN (2023), documentation on the design and specifications of the RD50-MPW4 sensor chip.
- [100] J. Debevc, M. Franks, B. Hiti, U. Kraemer, G. Kramberger, I. Mandić, R. Marco-Hernández, D. J. L. Nobels, S. Powell, J. Sonneveld, H. Steininger, C. Tsolanta, E. Vilella, and C. Zhang, “Measurements of time resolution of the RD50-MPW2 DMAPS prototype using TCT and  $^{90}\text{Sr}$ ,” (2024), [arXiv:2312.01793](https://arxiv.org/abs/2312.01793) [physics.ins-det].
- [101] L. van Rootselaar, “Keeping up the pace: Characterising the laser setup used to evaluate timing-performances of silicon pixel sensors for the HL-LHC upgrade,” (2022), bachelor thesis, Amsterdam University College.
- [102] R. M. Sternheimer, *Phys. Rev.* **88**, 851 (1952).
- [103] R. M. Sternheimer, *Phys. Rev.* **145**, 247 (1966).
- [104] R. Talman, *Nuclear Instruments and Methods* **159**, 189 (1979).
- [105] W. W. M. Allison and J. H. Cobb, *Annual Review of Nuclear and Particle Science* **30**, 253 (1980)

# Appendices

## Appendix A Supplementary Information

### A.1 Detailed Analysis of Particle Interaction and Energy Loss Mechanisms

Here, a detailed exploration of particle interactions with matter, energy loss mechanisms, and the specifics of the Bethe-Bloch equation can be found following the discussion made in [Subsection 2.2.1](#).

In the regime where  $\beta\gamma \approx 0.001$ , non-ionizing nuclear recoil is the main mechanism of energy dissipation for alpha particles. Similarly, at reduced momenta, protons also predominantly experience energy loss through this process. As  $\beta\gamma$  increases to 0.01, ionization losses become proportional to the particle's velocity until reaching a peak when the velocity approaches that of the atomic electrons in the absorber. Beyond  $\beta\gamma \geq 0.1$ , the electronic motion is less significant, with the mass stopping power being influenced by the particle's mass and charge sign slightly below this threshold.

When considering heavy charged particles (mass much greater than the electron mass) in general, the mass stopping power, beyond  $\beta\gamma \approx 0.1$ , typically decreases as  $\beta^{-k}$  ( $k$  ranges from 1.4 to 1.7) until reaching a minimum (1-2 MeV cm<sup>2</sup> g<sup>-1</sup>) in the range of  $3 \leq \beta\gamma \leq 3.5$ . Following this minimum, the relativistic rise occurs due to the relativistically extended transverse electric field of the incident particle. At even higher energies, radiative losses become considerable and eventually predominate, with the crossover point between ionization- and radiative-dominated energy loss varying based on the particle's mass [64]. The Bethe-Bloch equation adequately describes the energy loss due to atomic ionization or excitation by moderately relativistic heavy charged particles ( $\beta \geq 0.1$  and mass much greater than the electron mass).

Furthermore, the Bethe equation includes a density correction ( $\delta$ ) as can be seen in [Equation A.1](#), especially significant at highly relativistic velocities ( $\beta \geq 1000$ ), to account for the reduction in energy loss due to the screening of the incident particle's transverse electric field by the absorber material's polarization. This effect is more pronounced in dense materials and is typically expressed using the Sternheimer parameterization with  $x = \log_{10} \beta\gamma$  [63, 102]:

$$\delta(x) = \begin{cases} \delta(x_0)10^{2(x-x_0)} & \text{for } x_0 > x \\ 2x \log 10 + p_0 + p_1(x_1 - x)^{p_2} & \text{for } x_0 \leq x \leq x_1, \\ 2x \log 10 + p_0 & \text{for } x_1 \leq x \end{cases} \quad (\text{A.1})$$

where the parameters for silicon can be found in the literature:  $p_0 = -4.4351$ ,  $p_1 = 0.14921$ ,  $p_2 = 3.2546$ ,  $x_0 = 0.2014$ , and  $x_1 = 2.8715$  [103].

### A.2 Energy Loss Fluctuation

The concept of mass stopping power, as defined by Bethe Bloch ([Equation 2.4](#)), relates to the mean energy loss of a charged particle traversing a specific absorber material. Particularly for *MIPs*, this mean energy loss does not reliably represent the energy loss of individual particles due to the skewed nature of the energy loss distribution. This skewness arises from relatively rare but quite hard collisions, where energy is transferred to a single electron, resulting in the generation of a delta ray. Upon losing their energy, such electrons may exit the sensor material, thereby not contributing to the signal formation in the detector. The variability in energy loss is a factor influencing the time resolution of silicon-based tracking detectors.

To illustrate the energy loss distribution process as outlined by [104, 105], take the probability density function of energy loss  $E$  for a particle passing through an infinitesimally thin mass thickness  $\delta x$ , under the assumption that the likelihood of multiple collisions within  $\delta x$  is negligible:

$$F(\delta x, E) = (1 - p_1) \delta(E) + N_A \frac{Z}{A} \delta x \frac{d\sigma}{dE} + O(p_1^2), \quad (\text{A.2})$$

here,  $\delta$  represents Dirac's delta function, and  $p_1$ , represents a single collision likelihood within  $\delta x$ , is defined as:

$$p_1 = N_A \frac{Z}{A} \delta x \int_0^\infty dE \frac{d\sigma}{dE}, \quad (\text{A.3})$$

moreover, the differential cross-section is denoted by  $\frac{d\sigma}{dE}$ . In Equation A.2, the first parameter signifies the likelihood of zero energy loss, while the second parameter is equivalent to an energy loss greater than zero. At an arbitrary thickness  $x$  of mass, the energy loss distribution is originating from Equation A.2 through a series of convolution into:

$$F(x + \delta x, E) = \int_0^E d\epsilon F(x, \epsilon) F(\delta x, E - \epsilon), \quad (\text{A.4})$$

where the initial condition is set such that the likelihood of zero energy loss in zero mass thickness is 100%:  $F(0, E) = \delta(E)$ . The Laplace transform is performed to each of the ends of Equation A.4, the Laplace-transformed energy loss distribution  $\bar{F}$  is obtained:

$$\tilde{F}(x, s) = \exp \left[ -N_A \frac{Z}{A} x \int_0^\infty dE (1 - e^{-sE}) \frac{d\sigma}{dE} \right]. \quad (\text{A.5})$$

To derive Landau's renowned model [23], it was postulated that the main effect adding to the cross-section stems from Rutherford scattering on free electrons, characterized by  $(\beta E)^{-2}$  behaviour for  $E_{\text{cut}} < E < T_{\text{max}}$ , and is null outside of it. The maximal energy transfer  $T_{\text{max}}$ , previously discussed in subsection 2.2.1, is given in Equation 2.6. The lower cut-off energy  $E_{\text{cut}}$  is selected to align the resultant mean energy loss with Bethe Block's formula (Equation 2.4). Landau's energy loss distribution is then expressed as [24]:

$$F_L(x, E) = \frac{\phi_L(\lambda)}{\xi}, \quad (\text{A.6})$$

here is

$$\lambda = \frac{E}{\xi} - \log \frac{2m_e c^2 \beta^2 \gamma^2 \xi}{I^2} - 1 + \beta^2 + \gamma_E + \delta, \quad (\text{A.7})$$

where,  $\gamma_E = 0.577 \dots$  is Euler's constant, furthermore

$$\xi = \frac{1}{2} K z^2 x \frac{Z}{A} \frac{1}{\beta^2}, \quad (\text{A.8})$$

and the function  $\phi_L(\lambda)$  is known as the inverse Laplace transform with  $s^s$ :

$$\phi_L(\lambda) = \frac{1}{2\pi i} \int_{\alpha - i\infty}^{\alpha + i\infty} ds \exp(s \log s + \lambda s), \quad (\text{A.9})$$

here, the integral is taken such that it is in consideration to the imaginary axis with a real part  $\alpha > 0$  along a parallel line.

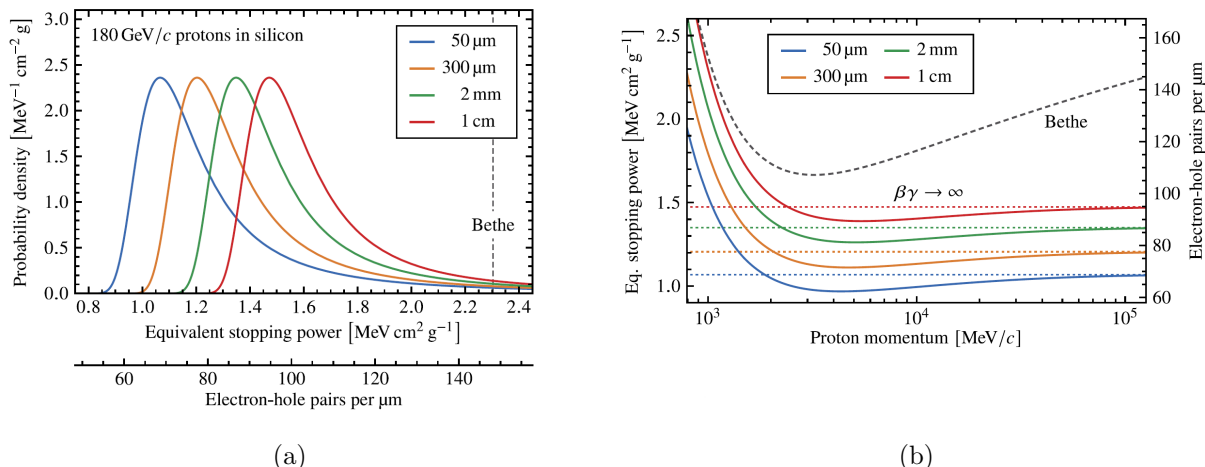


Figure A.1: **(a)** This figure illustrates the Landau energy loss distributions as a function of sensor thickness for protons with a momentum of 180 GeV/c traversing silicon. The distributions showcase the variability in energy loss dependent on the thickness of the silicon sensor. Additionally, the mean stopping power calculated by Bethe’s formula is shown for comparison, further illustrating its position relative to the Landau distribution tails. **(b)** This figure demonstrates the relationship between the most probable energy loss of protons and their momentum for various thicknesses of silicon sensors. It clarifies how the energy loss varies with changes in both the momentum of the protons and the thickness of the silicon sensor. Additionally, the mean stopping power derived from Bethe’s equation is also depicted, highlighting its relationship to the observed energy loss trends under different conditions. Images are taken from [19].

The Landau energy loss distribution plays a crucial role in understanding the interaction of charged particles with the detector material. Figure A.1a illustrates the Landau energy loss distribution for 180 GeV/c protons traversing silicon sensors of varying thicknesses. Notably, the stopping power derived from Bethe’s equation mainly resides in the distribution’s tail, highlighting the distinction between average and most probable energy losses in high-energy interactions.

To quantify the energy deposition in silicon, the secondary horizontal axis of Figure A.1a represents the number of *EHPs* generated per unit path length within the detector. This estimation is predicated on the assumption that the entire energy of the incident particle is absorbed by the material. Given that the average energy required to create a single *EHP* in silicon is approximately 3.62 eV, this axis allows for a direct correlation between energy loss and charge carrier generation [63].

The peak of the Landau energy loss distribution (Equation A.6) is the most probable energy loss, defined as:

$$E_{\text{mp}} = \xi \left( \log \frac{2m_e c^2 \beta^2 \gamma^2 \xi}{I^2} + 0.2000 - \beta^2 - \delta \right), \quad (\text{A.10})$$

which was postulated in [68].

Figure A.1b further explores the energy loss dynamics by depicting the energy loss of protons in silicon to the incident particle’s momentum. A noticeable trend is the increasing divergence from Bethe’s mean energy loss with increasing particle momentum. This deviation underlines the dependency of the most probable energy loss on the sensor’s total path length. In scenarios involving high momentum particles, the anticipated count of *EHPs* per micron in silicon ranges from approximately 70 to 80 for sensor thicknesses of 50 μm and 300 μm, respectively. Such insights



are pivotal in optimizing sensor design and understanding the response of silicon detectors.

While Landau's model is highly reliable for thin absorbers, it underestimates energy fluctuation for certain conditions, leading to the development of more accurate models such as the photoabsorption ionization (PAI) models [105]. These models consider the full photoabsorption spectrum, improving the differential cross-section of energy loss. For theoretical analyses of silicon sensor time resolution, Landau's model is combined with data-driven modifications and convolution with a Gaussian function, resulting in the Langaus model:

$$F_{LG}(E) = N\phi_L \left[ \frac{E - \mu_L}{\sigma_L} \right] \cdot \exp \left( -\frac{1}{2} \left( \frac{E}{\sigma_G} \right)^2 \right), \quad (\text{A.11})$$

here  $\phi_L$  is Landau's function from [Equation A.9](#),  $N$  a normalisation constant,  $\sigma_G$  and  $\sigma_L$  are the scale parameters of the Gaussian and Landau functions, respectively, and  $\mu_L$  the location parameter of the Landau function.

## Appendix B Laser Specifics

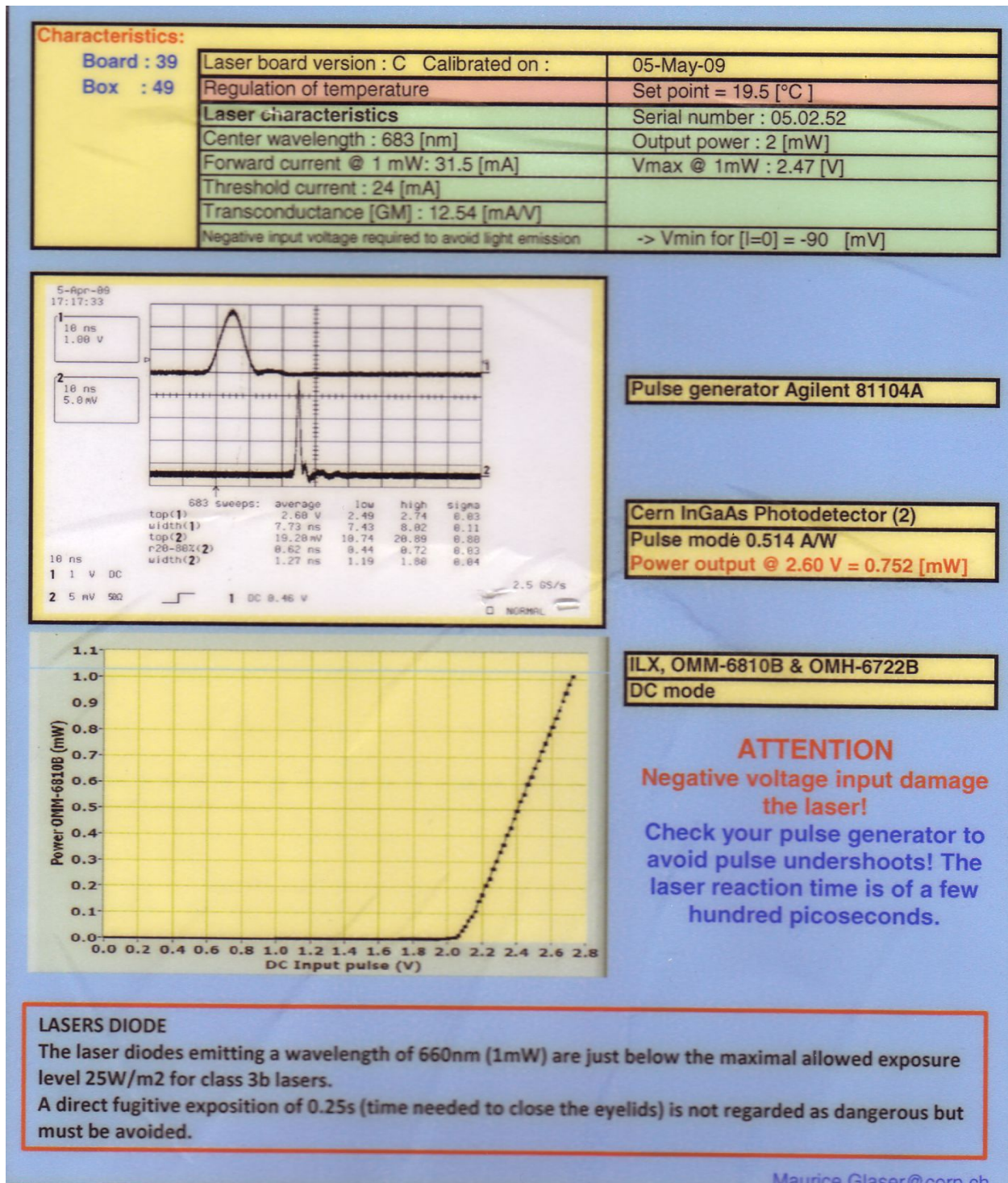


Figure B.1: Laser specifics of the 683 nm slow SPA.

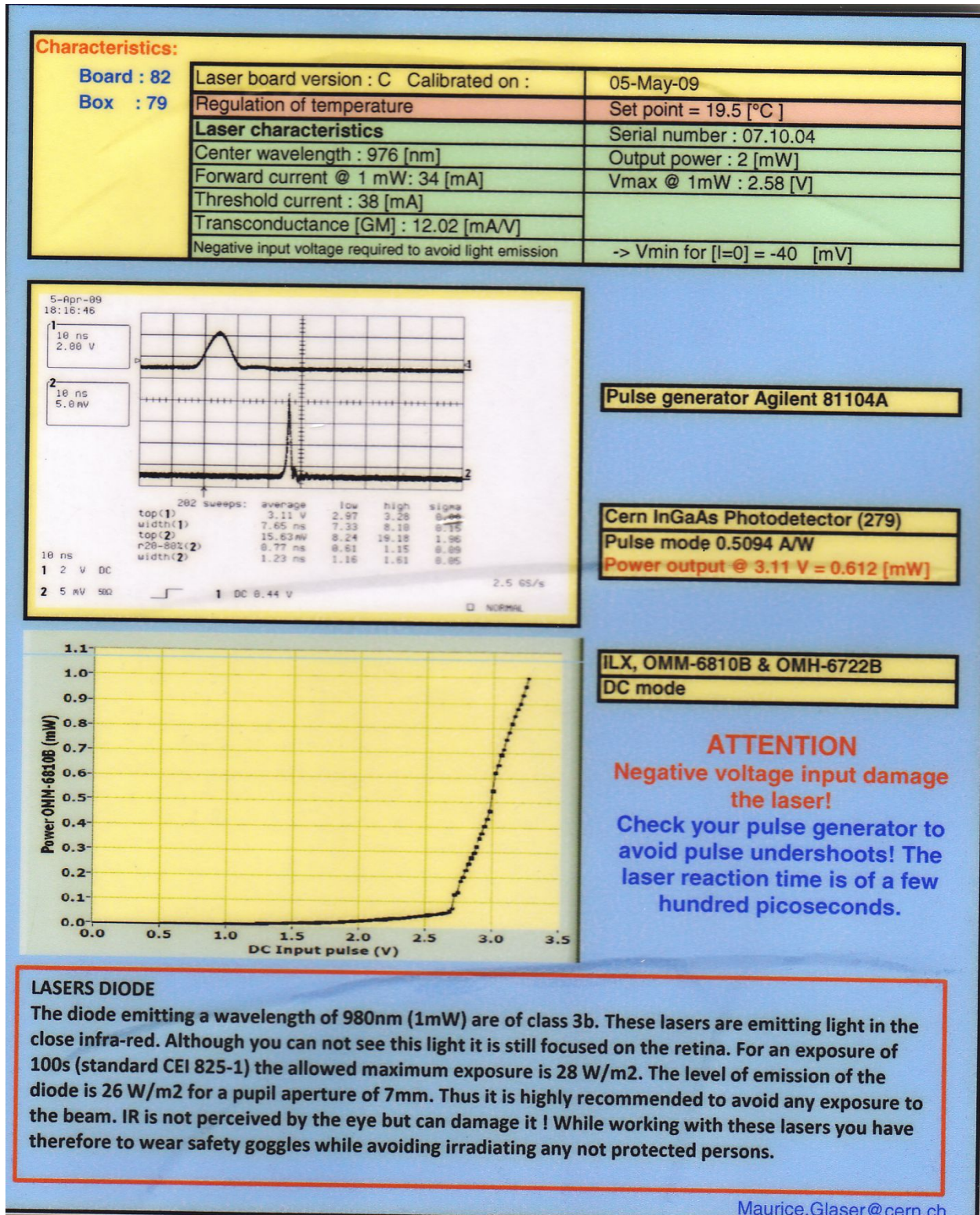



Figure B.2: Laser specifics of the 976 nm slowSPA.

# Appendix C Test and Calibration Report of the PILAS System

## PILAS DX Test Report



Date: November 30, 2022  
by: epsc  
checked: bokh

<b>Item</b>	<b>Characteristics</b>
<b>Head (PN):</b>	PIL1-094-40FC
Serial number:	1113
<b>Controller (PN):</b>	EGI-D2-40                      max. PRF 40MHz, FW:V1.1AEe
Serial number:	1113
<b>Laserdiode:</b>	WT1959
Wavelength:	932.7nm                      (measured at 40MHz)
Spectral width (FWHM):	6.1nm                          (measured at 40MHz)
Laser diode temperature:	23°C
Thermistor:	NTC 10 kΩ at 25°C
<b>Optics</b>	
Laserdiode Collimator:	50CL-A4.5-07
Focal length:	4.5mm (asphere)
Numerical aperture:	0.55
Beam diameter (1/e <sup>2</sup> ):	3.3mm x 1.1mm @ 0.5m
Beam divergence* (1/e <sup>2</sup> ):	0.18mrad x 0.56mrad
<i>* half angle</i>	
Fiber Coupler:	60SMF-1.4-A11-02 (FC/APC)
Focal length:	11 mm
Numerical aperture:	0.25
Fiber:	P3-830A-FC-1
type:	SM800-5.6-125, 1m length, 3mm jacket
core / MFD:	unknown / 4.7 - 6.9 μm @ 830 nm
NA (5% drop):	0.11-0.13
Connectors:	2x FC/APC

Laser Class: **3B**  
IEC 60825-1:2014  
see manual for laser  
warning label  
reproduction

A.L.S. GmbH - part of NKT Photonics - www.nktphotonics.com
Page 1 / 3
Photon PIL1-094-40FC\_1113

Figure C.1

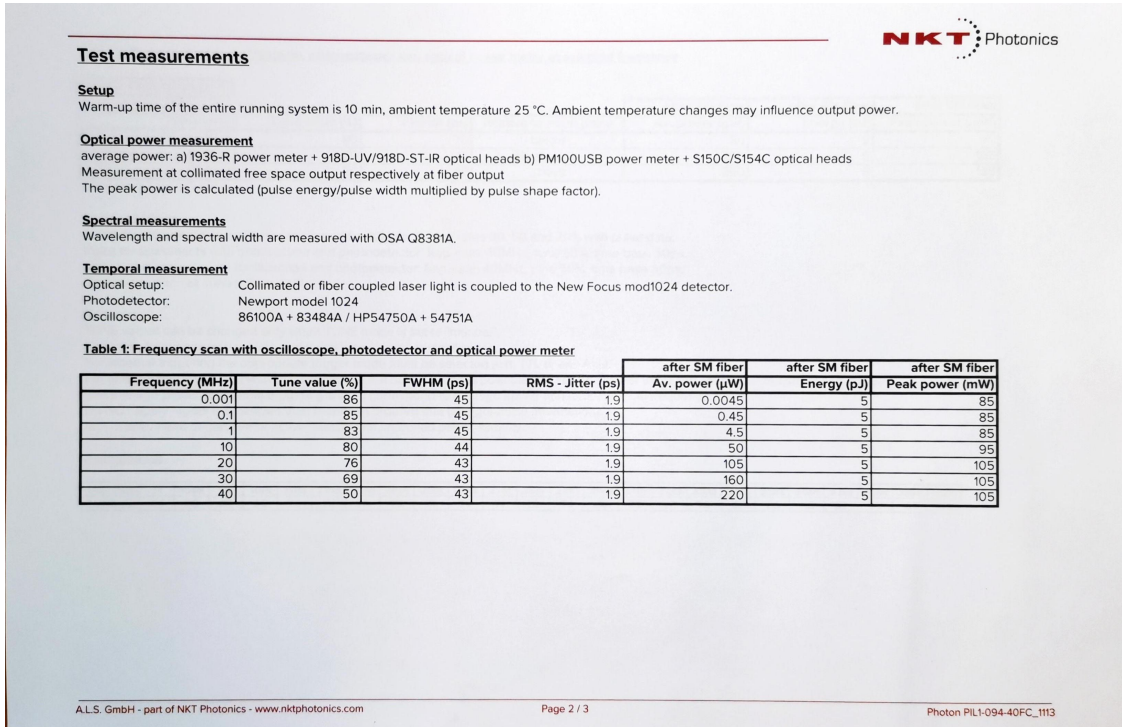


Figure C.2

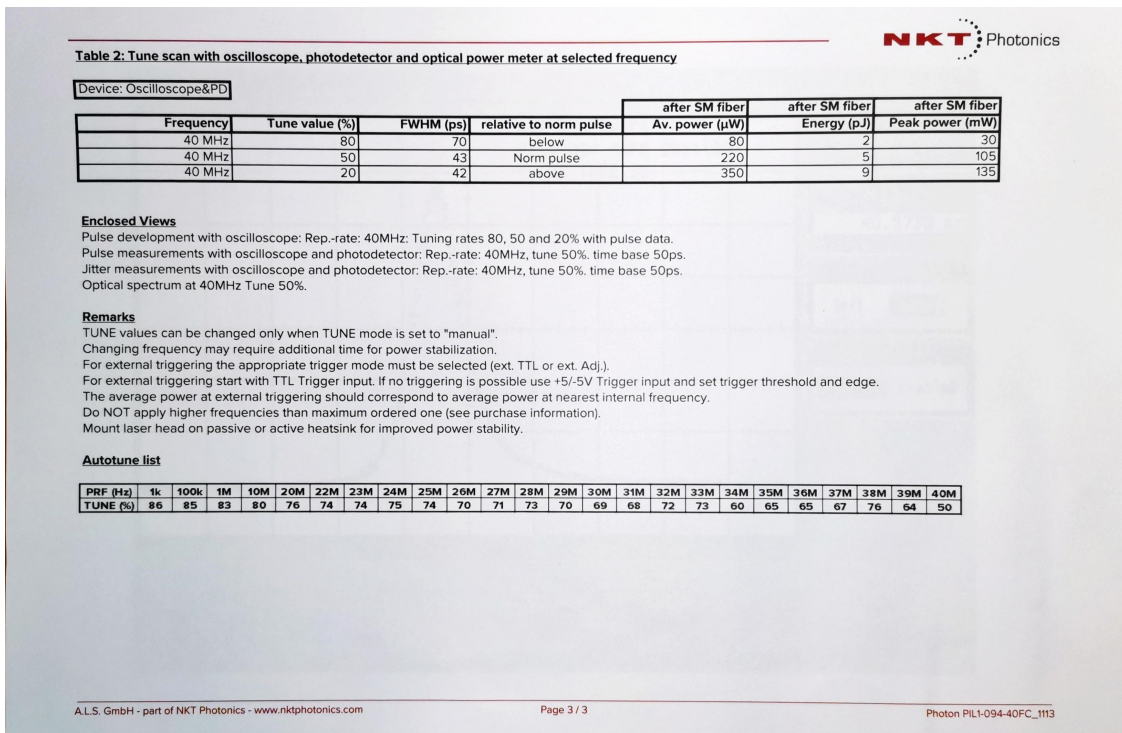


Figure C.3

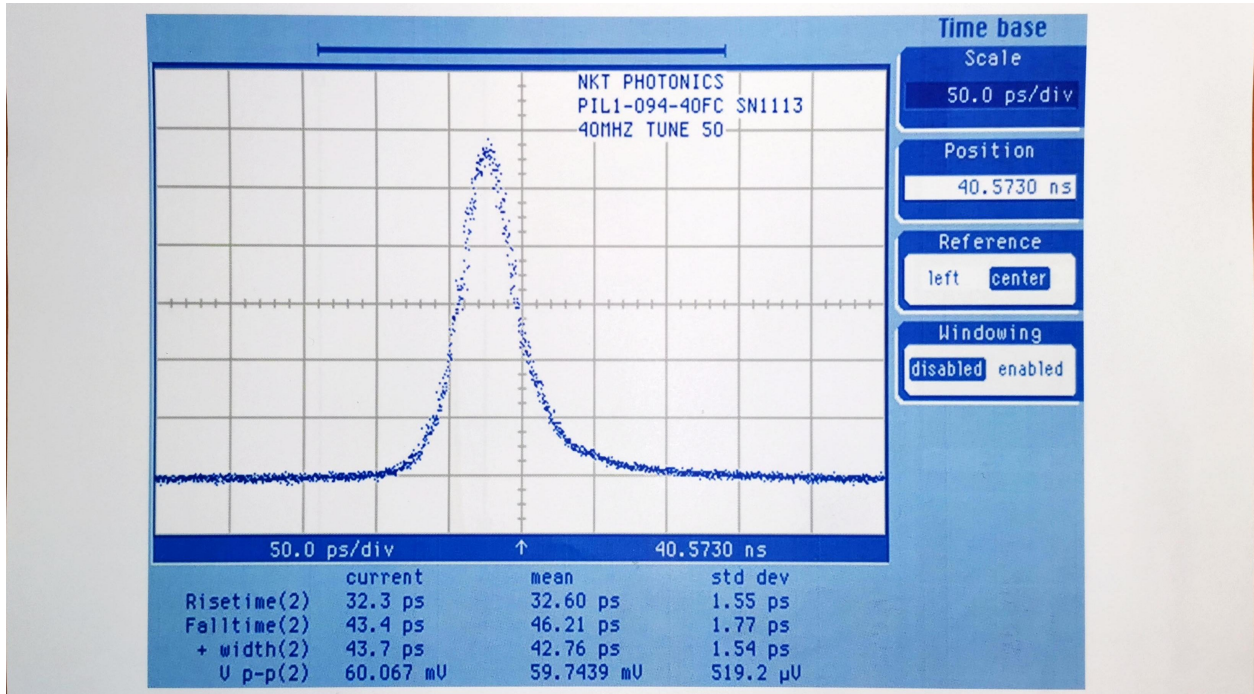


Figure C.4

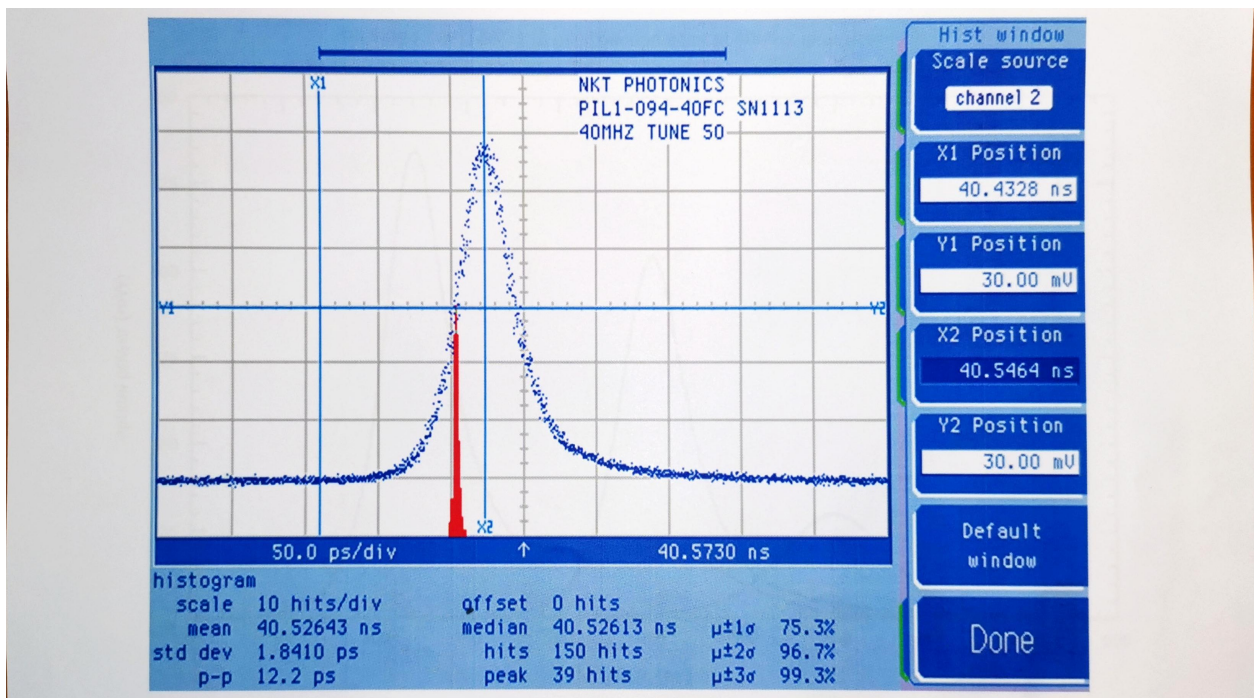


Figure C.5

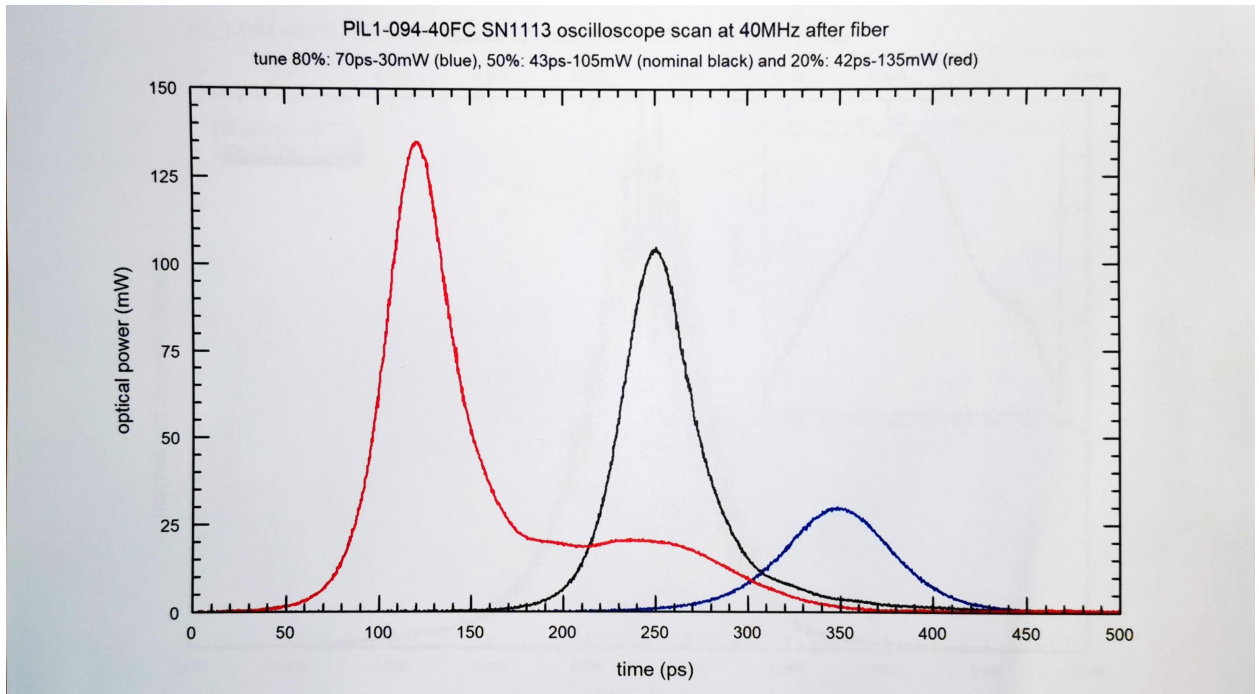


Figure C.6

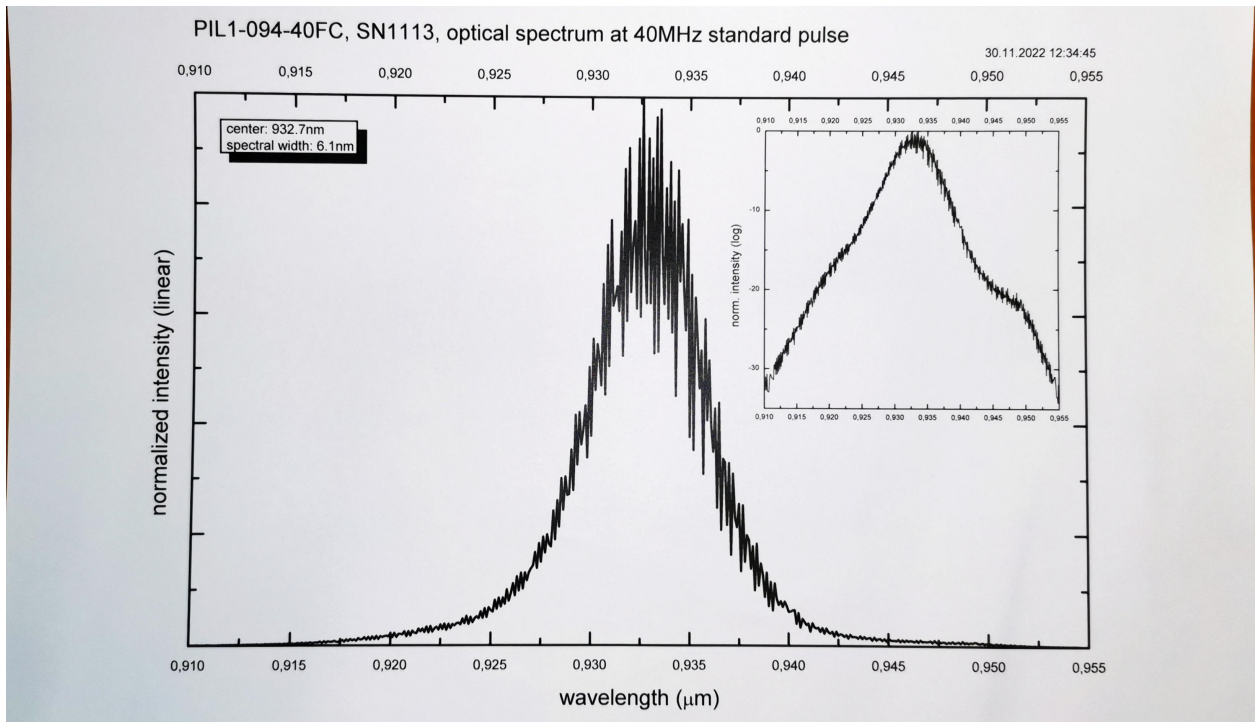
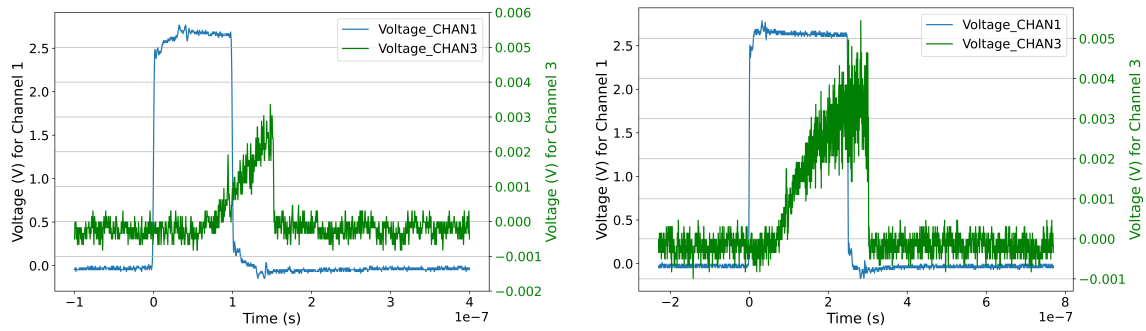


Figure C.7

## Appendix D Measurement Graphs

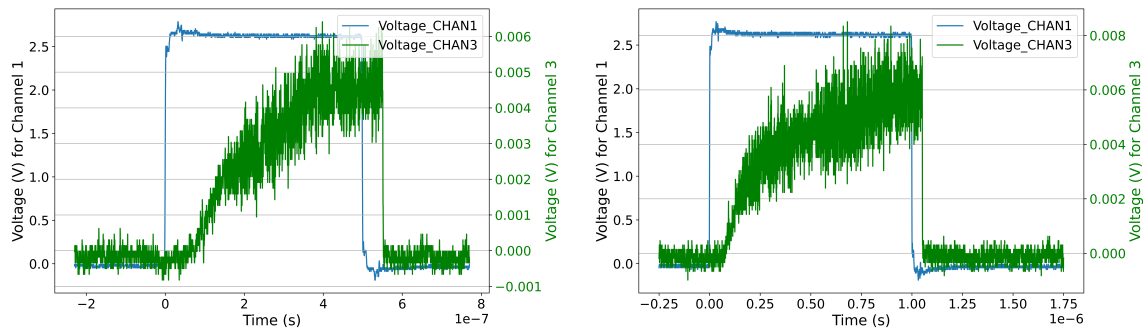
### D.1 683 nm

Measurement results of the 683 nm slow *SPA* and related to the arguments made in [subsection 4.1.1](#).



(a) The waveform at 100 ns applied pulse width. (b) The waveform at 250 ns applied pulse width.

Figure D.1: Both waveforms of the 683 nm slow *SPA* are at SI2.6 applied bias.



(a) The waveform at 500 ns applied pulse width. (b) The waveform at 1 μs applied pulse width.

Figure D.2: Both waveforms of the 683 nm slow *SPA* are at SI2.6 applied bias.



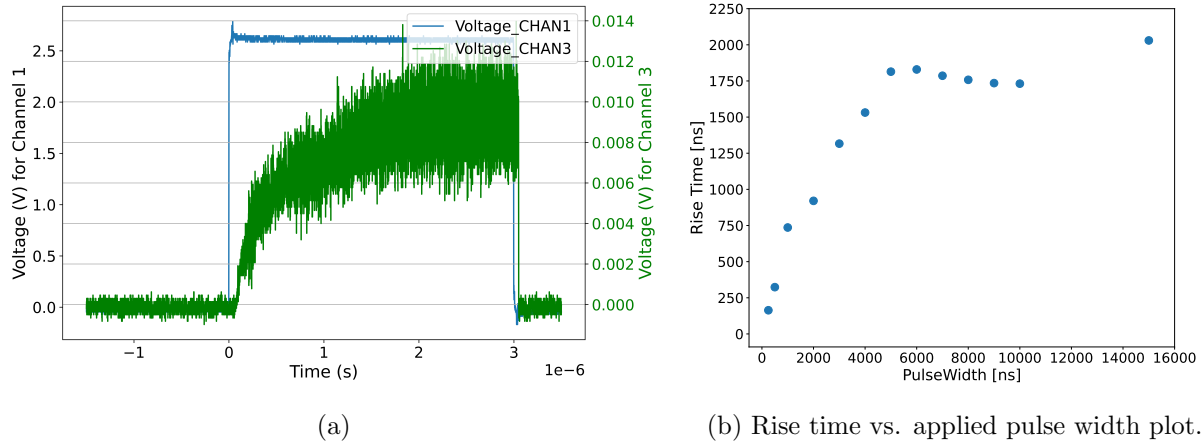
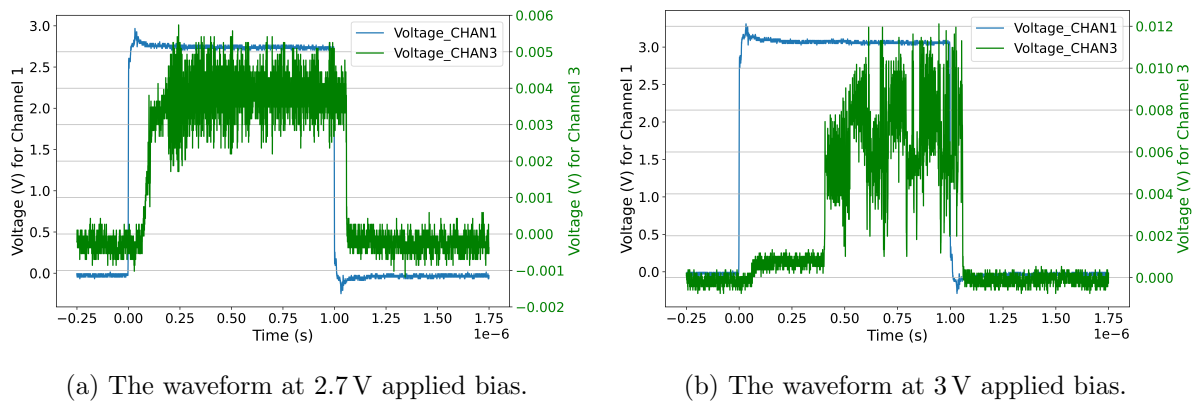


Figure D.3: Both waveforms are taken at 2.6 V applied bias and 3 μs applied pulse width.

D.2 976 nm

Measurement results of the 976 nm slow SPA and related to the arguments made in subsection 4.1.2.



(a) The waveform at 2.7 V applied bias.

(b) The waveform at 3 V applied bias.

Figure D.4: Both waveforms of the 976 nm slow SPA are at 1 μs applied pulse width.

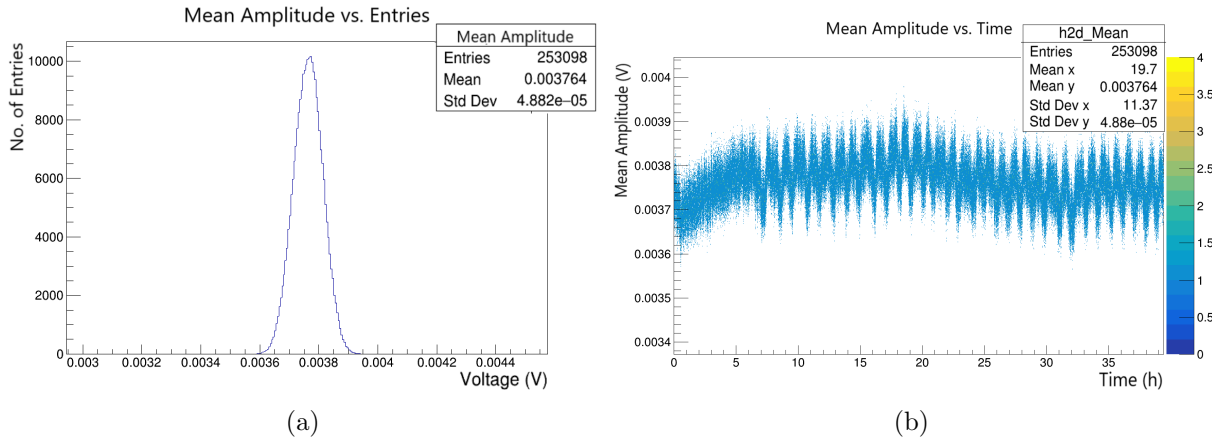


Figure D.5: Both amplitude results are of the 976 nm slowSPA at 1  $\mu$ s applied pulse width and 2.7 V applied bias.

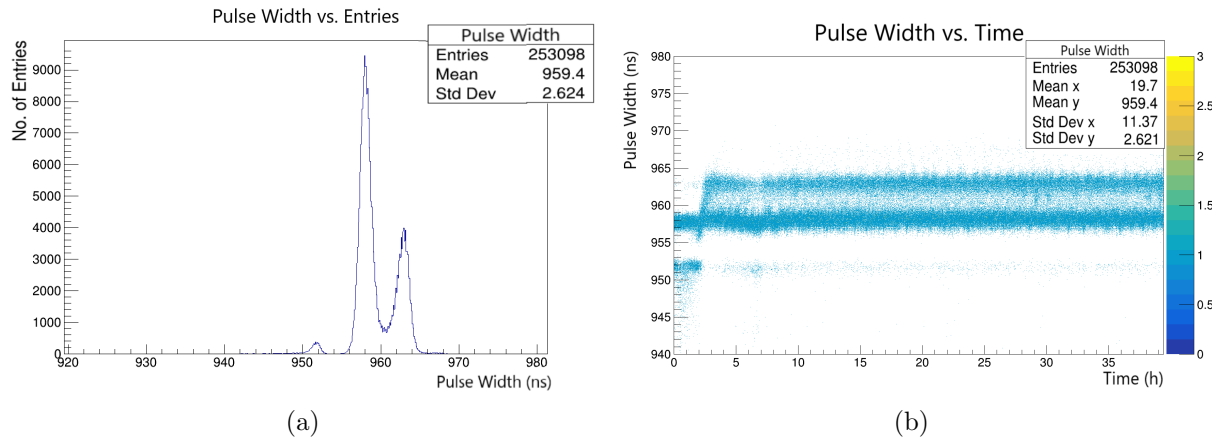


Figure D.6: Both pulse width results are of the 976 nm slowSPA at 1  $\mu$ s applied pulse width and 2.7 V applied bias.

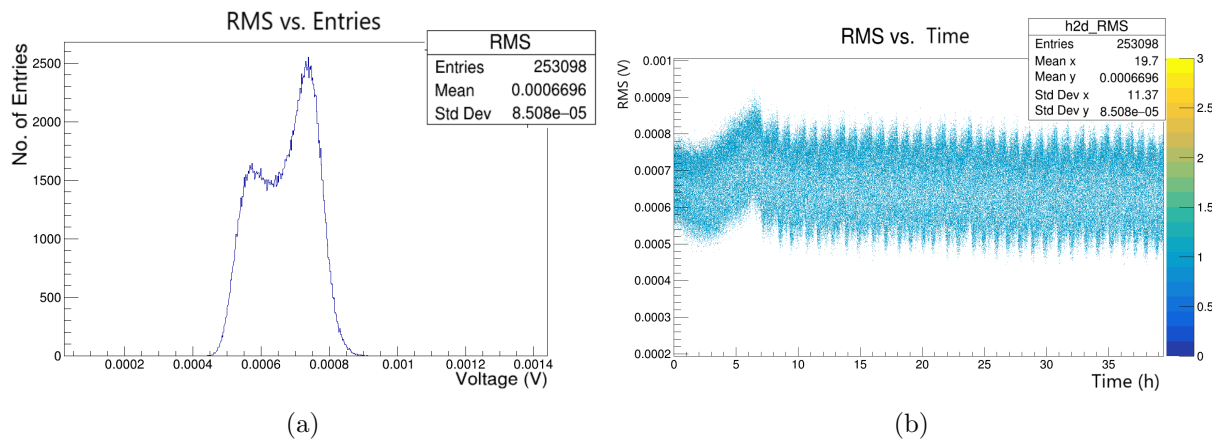
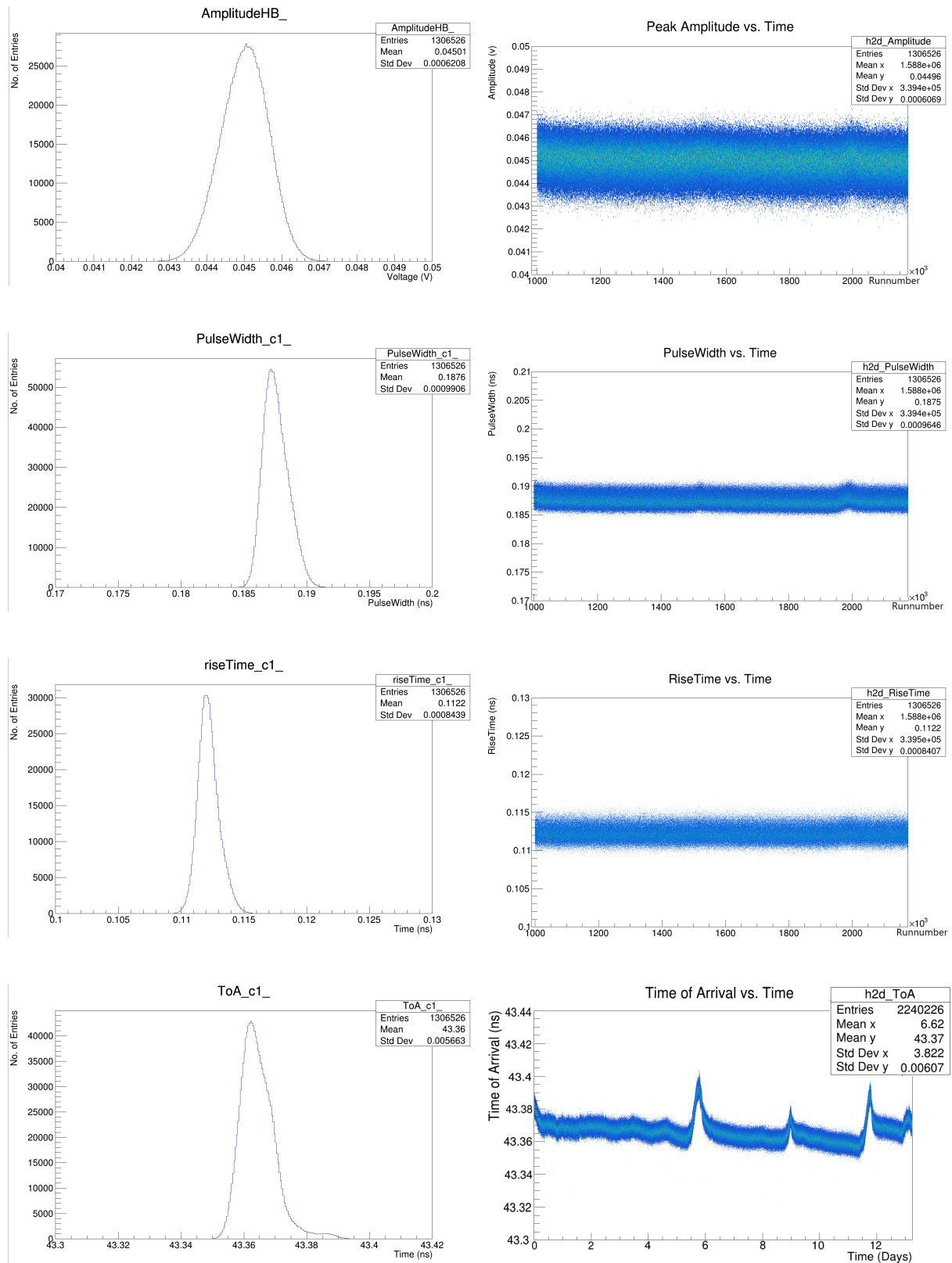


Figure D.7: Both RMS of the amplitude height are of the 976 nm slowSPA at 1  $\mu$ s applied pulse width and 2.7 V applied bias.

### D.3 933 nm

Measurement results of the 933 nm fastSPA and related to the arguments made in subsection 4.1.3.



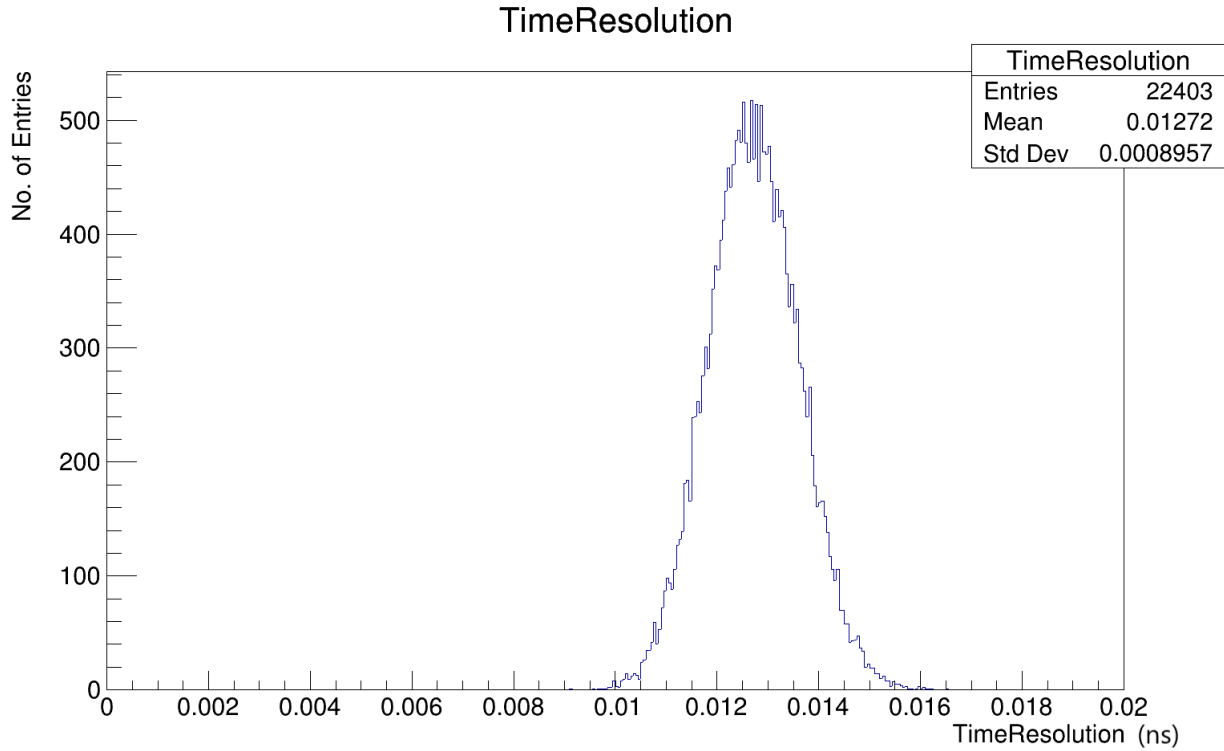


Figure D.12: Measured time resolution of the 933 nm fastSPA using the DET08CFC/M Detector.

#### D.4 RD50-MPW3

Measurement results of the RD50-MPW3 using the 933 nm fastSPA and related to the arguments made in subsection 4.2. All measurements were made from the same pixel with all the same applied parameters, and only the difference between clock on and clock off is depicted.

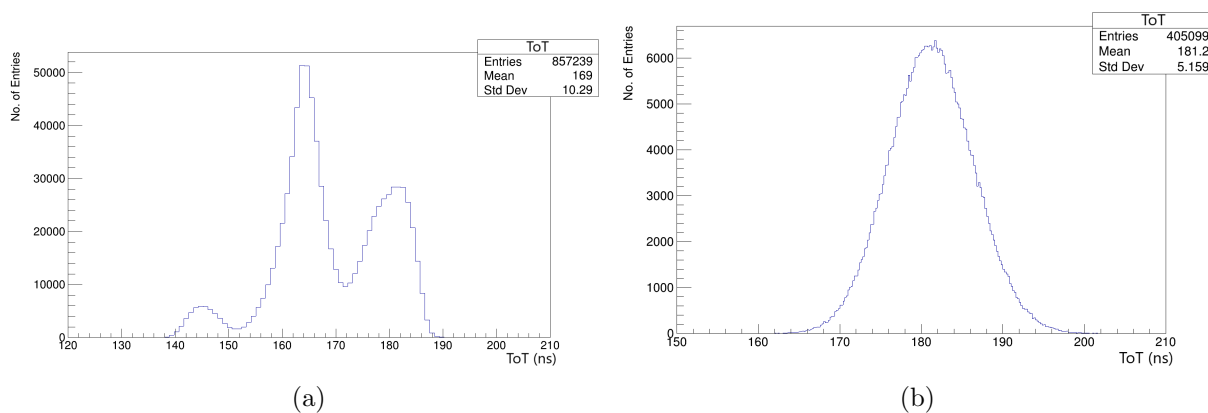


Figure D.13: Both entries plots depict the *ToT*. (a) does so for the clock-on situation and (b) for the clock-off situation.

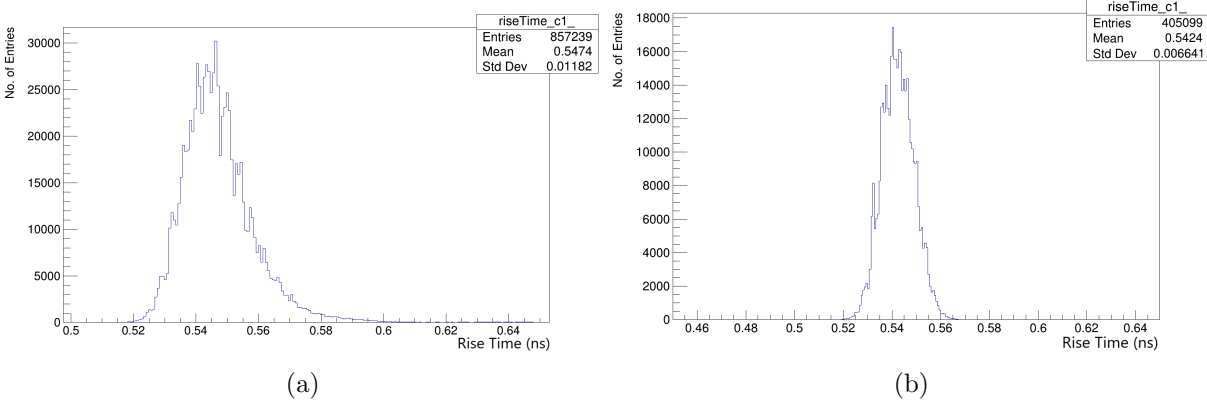


Figure D.14: Both entries plots depict the rise time. (a) does so for the clock-on situation and (b) for the clock-off situation.

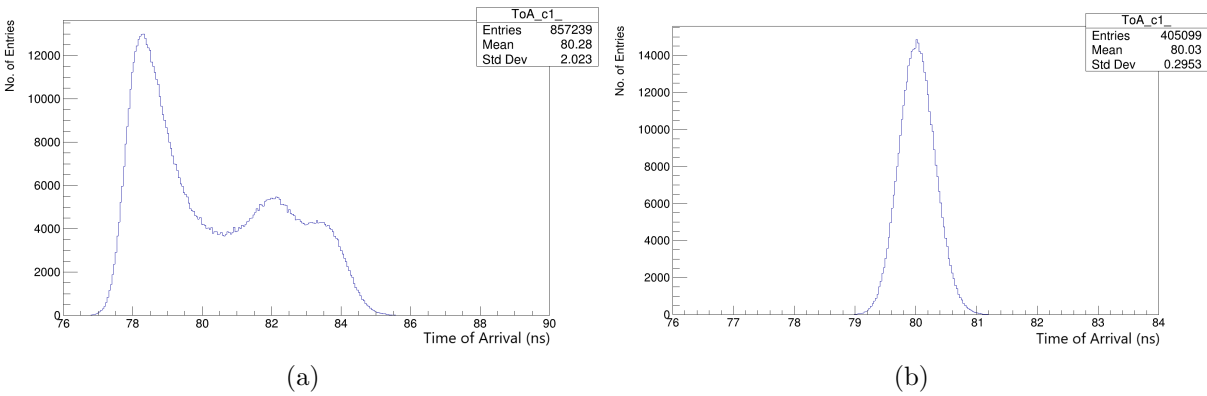


Figure D.15: Both entries plots depict the  $ToA$ . (a) does so for the clock-on situation and (b) for the clock-off situation.

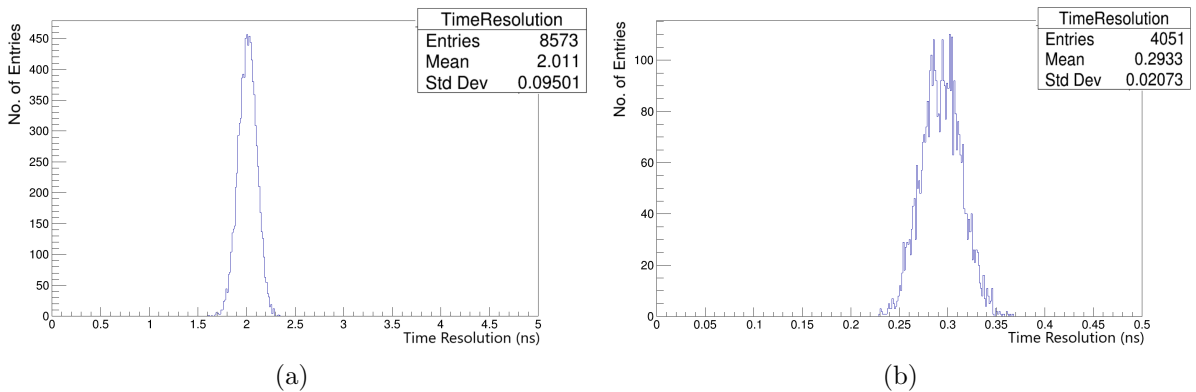


Figure D.16: Both entries plots depict the time resolution. (a) does so for the clock-on situation and (b) for the clock-off situation.

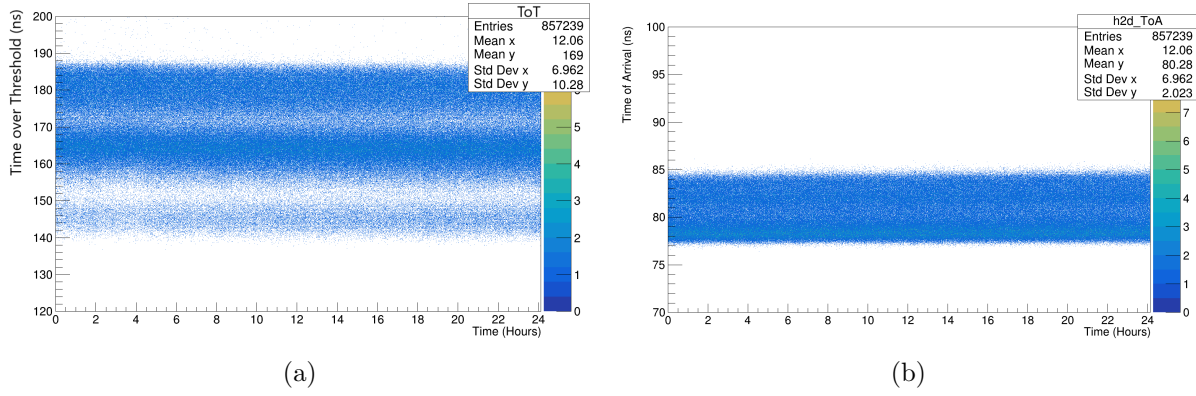


Figure D.17: Both plots depict the clock-on situation for a long period of time. (a) does so for the  $ToT$  and (b) for the  $ToA$ .

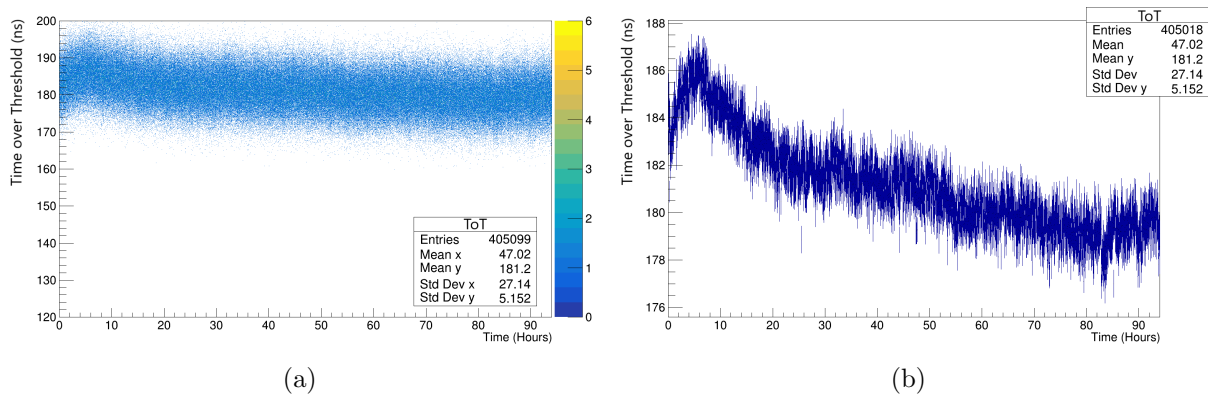


Figure D.18: Both plots depict the  $ToT$  over a long period of time for the clock-off situation.

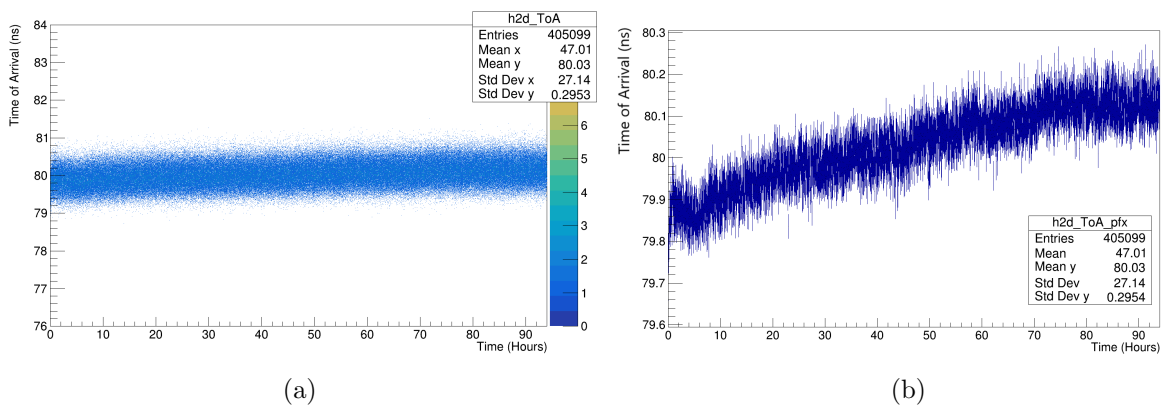


Figure D.19: Both plots depict the  $ToA$  over a long period of time for the clock-off situation.

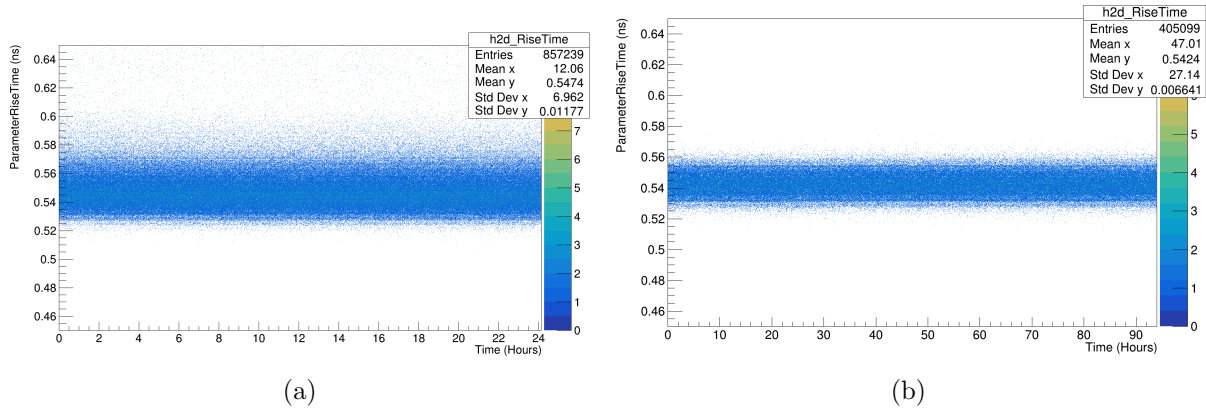


Figure D.20: Both plots depict the rise time over a long period of time. (a) does so for the clock-on situation and (b) for the clock-off situation.

## D.5 RD50-MPW4

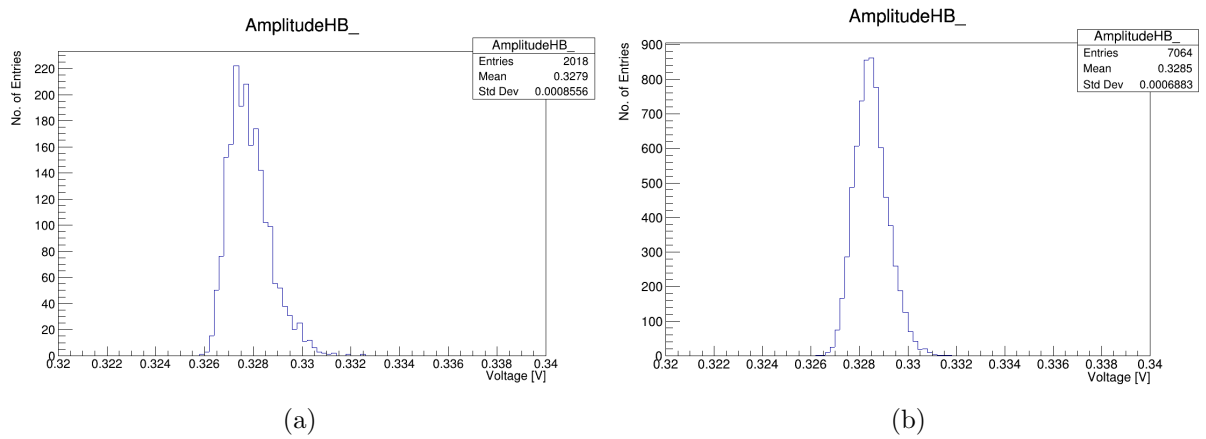


Figure D.21: Both entries plots depict the amplitude magnitude of pixel column 35 row 41 at 350 V reserve bias voltage. (a) does so for the clock-on situation and (b) for the clock-off situation.

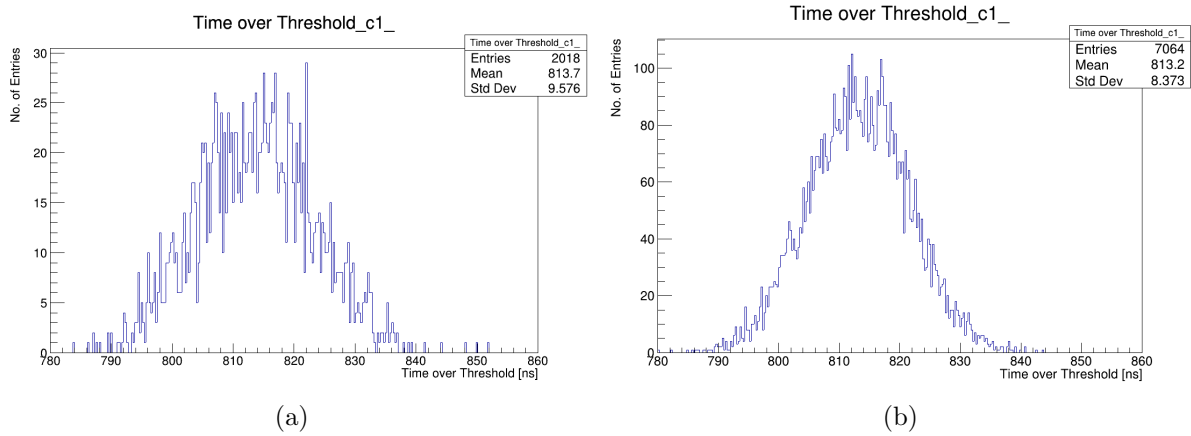


Figure D.22: Both entries plots depict the  $ToT$  of pixel column 35 row 41 at 350 V reserve bias voltage. (a) does so for the clock-on situation and (b) for the clock-off situation.

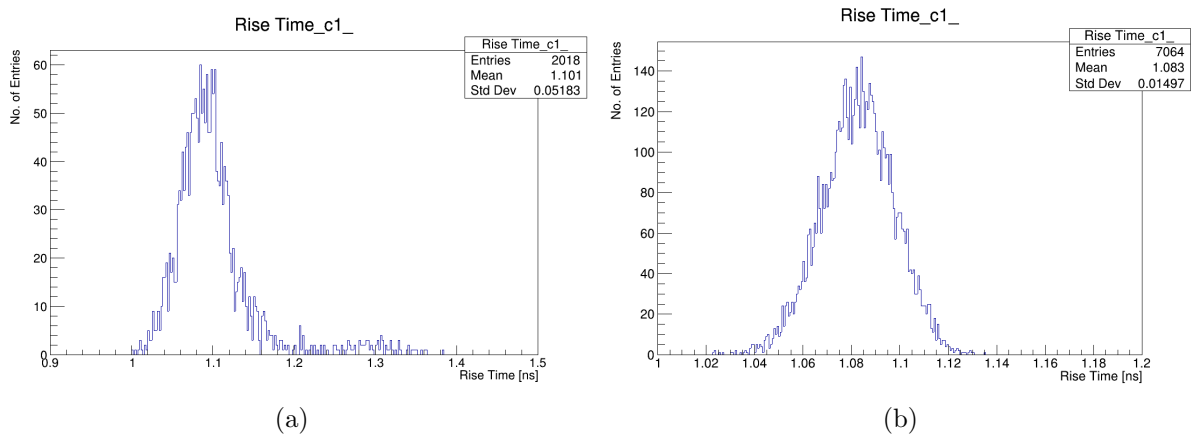


Figure D.23: Both entries plots depict the rise time of pixel column 35 row 41 at 350 V reserve bias voltage. (a) does so for the clock-on situation and (b) for the clock-off situation.



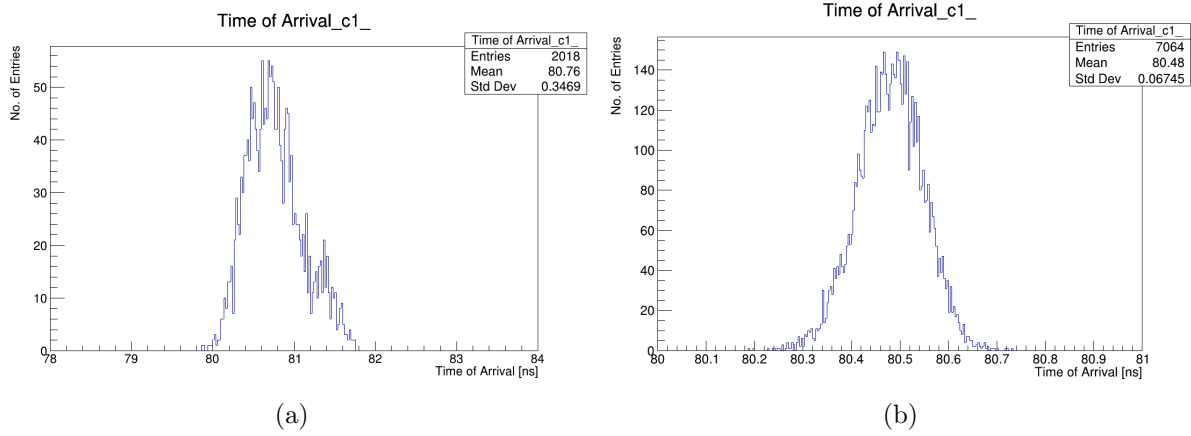


Figure D.24: Both entries plots depict the  $ToA$  and the Std Dev is the measured time resolution of pixel column 35 row 41 at 350 V reserve bias voltage. (a) does so for the clock-on situation and (b) for the clock-off situation.